Synthetic seismic modelling of fluvial channels in the Blackhawk Formation as an analogue to the Triassic Barents Sea

Espen Friestad

Master Thesis in Petroleum Geoscience

Department of Earth Science
University of Bergen
November 2018

Abstract

Seismic modelling studies based on field analogues is a promising tool to close the gap between observations in field and interpretations of seismic data. Fluvial channel deposits can be great reservoirs for hydrocarbons, water and CO_2-storage in the subsurface. However, there are considerable uncertainties on how size, geometries and architecture of such deposits are resolved in subsurface seismic. By seismic modelling outcrops of fluvial channel deposits that have such variation in size, geometry and architecture, the resulting synthetic seismic data can be analysed and used to better understand subsurface fluvial reservoirs. To increase knowledge about seismic imaging of fluvial deposits, I will present different synthetic seismograms from non-marine deposits in the Blackhawk Formation from a seismic-scale (250 m x 5.3 km) outcrop in Book Cliffs (Utah, USA). The study highlights what impact the dominant frequency has on the detail-level for such deposits in seismic data. In comparison with actual seismic data from the Triassic Barents Sea, synthetic seismic data with equivalent frequency show several similarities in detail. Furthermore, the process of analogue seismic modelling is evaluated, where the input from a high-detailed (down to 14 cm) outcrop-mapping shows a difference of up to 36 % in seismic amplitude compared to more conventional and simplified input-modelling. A survey in seismic interpretation of fluvial deposits was conducted using the generated seismograms, where nine participants that are geologists with different levels of experience, were asked to map out fluvial deposits at different resolutions. This gives an objective view of how the different synthetic seismograms would be interpreted by unbiased interpreters, where the results show that high-resolution seismic are interpreted in more detail but still have large uncertainties. By improving the understanding of fluvial deposits at different resolution-levels, it is possible to make seismic interpretations that are closer to the real stratigraphy.

Acknowledgement

I would like to seize the opportunity to thank a number of people who helped both scientifically and personally in order to build this thesis. First and foremost, I want to express my sincere gratitude to my main supervisor Christian Haug Eide for all the feedback and great guidance during the last two years. A special thanks to my co-supervisor Isabell Lecomte for the guidance in seismic modelling and use of SeisRoX.

Thanks to co-supervisor Simon Buckley and the VOG Group for the academic license to use the software LIME and for providing the LiDAR-model of the Beckwith Plateau and Wasatch Plateau. NORSAR is also thanked for the academic licence of the program SeisRoX. Special thanks to the Trias North-project and their sponsors, who have funded this thesis and for providing 3D seismic data of the Barents Sea.

To my family and fellow students over the past years, thank you for the support during the work of this thesis. Especially, Aasmund Olav Løvestad for the field assistance in Utah, Thomas Jarle Grimstad and Martin Kyrkjebø Johansen for geophysics guidance, the participants of the conducted survey and the boys of Svelget for both academic and non-academic discussions.

Table of Contents

1 INTRODUCTION

1.1 Aim of study

Significant volumes of oil and gas are trapped in fluvial deposits worldwide (Ford & Pyles, 2014; Miall, 2006a), as well as much of world's drinking water aquifers are of fluvial origin (Bridge & Tye, 2000). Some major fluvial petroleum reservoirs are the Statfjord Formation and the Ness Formation of the Brent Group in the North Sea, the Sarir field in Libya and the Sheerwood Sandstone Group in England (Miall, 2006a). Subsurface fluvial reservoirs also have potential for CO_2 storage in the future (Shi et al., 2013). There are however several challenges for geologists and engineers that work with such reservoirs in terms of predicting dimensions, sand connectivity, and spatial and temporal changes in the system (Ford & Pyles, 2014). These challenges require detailed knowledge and information of the subsurface distribution and facies (Miall, 2006a).

Computer modelling and comparison with outcrop analogues is a way to assist the characterization of the fluvial reservoirs for geologist and engineers (e.g. Ashton, 1993; Buller, 1990; Flint & Bryant, 1993; Martin, 1993; Miall & Tyler, 1991). The models can take many forms, including modern analogues of the depositional system to the interpreted reservoir, outcrop units as analogues that was formed under similar conditions, physical scale models and numerical simulations of the reservoir (Miall, 2006b). The input data can be values from available outcrops or subsurface wells (Miall, 2006b).

One useful way to model when working with subsurface reservoirs, is seismic modelling of outcrops. This is valuable in order to link subsurface seismic facies interpretations with observed geometrical relations in outcrops (Falivene et al., 2010; Helland-Hansen et al., 1994; Hodgetts & Howell, 2000). This way of modelling can improve the understanding of subsurface deposits imaged in seismic datasets, as well as inform how the seismic reflection pattern are able to capture actual stratal geometries at different seismic resolutions (Helland-Hansen et al., 1994). In addition to be necessary to understand seismic imaging of subsurface architectures in the

subsurface, seismic modelling is both insightful and cost-efficient when the right methods are used (Lecomte et al., 2016).

It is important that analogues that are chosen as input for seismic models are appropriate for the investigated subsurface fluvial system (Bridge & Tye, 2000). However, the level of details in analogue outcrops and modern data has increased during the recent two decades due to development in technology and digital outcrop mapping, which allows far more realistic geological models and further applications in seismic interpretation (Lecomte et al., 2016). In recent studies, modern digital outcrop mapping has been used as input to create synthetic seismic. Anell et al. (2016) has used this technique to create synthetic seismic of faults, paralic deltaic deposits and intrusions in the NW Barents shelf. Eide et al. (2017b) also published an article where outcrops of mafic sill complexes in a sedimentary basin in east Greenland was seismic modelled and compared with actual seismic. Rabbel et al. (2018) recently published a paper that focuses on seismic modelling of igneous sill complexes, more specifically, oil-producing andesitic sills in Argentina. Carbonate outcrops are also being used as input to generate synthetic seismic by Johansen (2018), which has studied the seismic response to paleokarst reservoirs.

However, little work has been done on seismic modelling of reservoir-scale fluvial deposits, such as the non-marine part of the Blackhawk Formation in the Book Cliffs, Utah. Therefore, little is known about the limits of imaging of different fluvial geometries. The large, world-class exposures of the Blackhawk Formation in Central Utah is an excellent analogue to many reservoir that consist of deposits from meandering fluvial systems, such as the Ness Formation of the Brent Group (Flood, 2015) and the Snadd and Kobbe Formations in the Barents Sea (Klausen et al., 2014; 2017). Large virtual outcrop models acquired from the Book Cliffs can therefore be used to provide detailed information as input data to seismic modelling of such deposits. By comparing the resulting synthetic seismograms to actual stratal seismic, it is possible to identify similarities and limitations in seismic images.

The goals in this study are threefold: (1) to investigate the architecture of the ancient fluvial deposits in the non-marine Blackhawk Fm.; (2) to investigate how these fluvial deposits will be imaged in seismic data; and (3) to compare the synthetic seismic images to subsurface fluvial deposits in the Barents Sea and discuss how insights from this could improve seismic interpretation of fluvial reservoirs.

1.2 Study area

The studied deposits are exposed in the Book Cliffs located in central Utah, USA. The Book Cliffs are a series of plateaus that begins in east-central Utah, just west of Helper (Figure 1.2.1), and continues all the way to the Colorado border (Van Wagoner, 1995). The total extent of the Book Cliffs are over 200 km long (Van Wagoner, 1995). The exposures are more precisely the western and southern faces of the Beckwith Plateau between Woodside Canyon and Battleship Bute, within Emrey County. Cross-cutting valleys within the plateau gives some three-dimensional perspective of the deposits (Rittersbacher et al., 2014b). The total length of the outcrop is approximately 28 km (Rittersbacher et al., 2014a) and it is roughly shaped as a horseshoe. This entire outcrop has been covered by heli-LiDAR scan and is the main dataset in this study. The maximum height of the scan is up to 500 m, but the studied non-marine deposits are in the upper Blackhawk Formation and lower Castlegate Sandstone, which are situated in the thickness interval of 250 m to 310 m. An additional dataset of sedimentary logs have been acquired in the field, where 43 m has been vertically logged in this study at the Woodside Canyon, the northernmost part of the Beckwith Plateau.

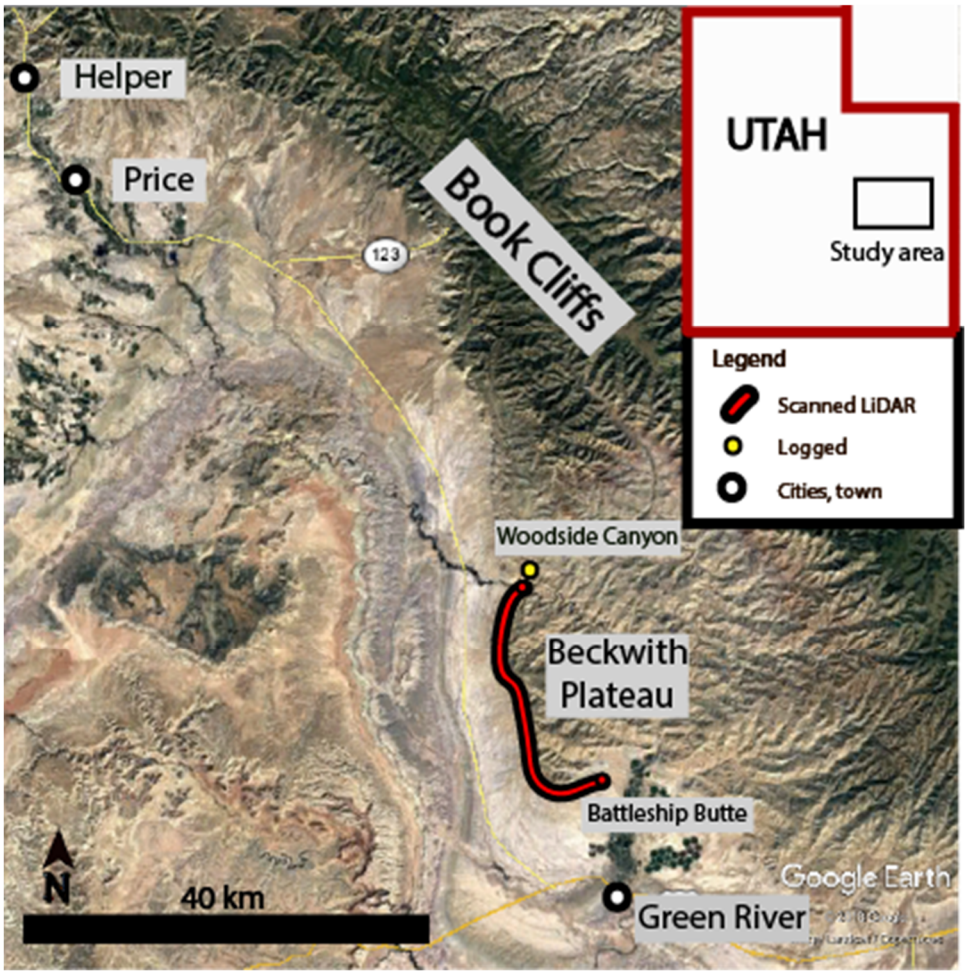

Figure 1.2.1 Map of study area in Utah, USA. LiDAR-scan of the Beckwith Plateau is the main input in this study. A sedimentary log has been acquired in the Woodside Canyon as additional detailed data. Satellite photo © Google Earth 2018.

2 GEOLOGICAL BACKGROUND

2.1 Tectonic history and basin development

The studied deposits of upper Blackhawk Formation and lower Castlegate Sandstone, are part of a Campanian (Late Cretaceous) (Figure 2.1.1) (Young, 1955) siliciclastic wedge that prograded into the foreland basin of the Sevier Orogen (Kauffman & Caldwell, 1993; Van Wagoner, 1995). The Sevier Orogeny is a part of the Cordilleran retroarc thrust belt and foreland basin system, which was a result of closure of oceanic basins and accretion of arcs along the western edge of the North American Plate (DeCelles, 2004). The thrusting of western United States began in Late Jurassic (Burchfiel & Davis, 1975), but the first evidence of thrusting in Utah is from Barremian (Early Cretaceous) (Sprinkel et al., 1999). The hinterland compression occurred in a series of events, where the deposition of the Blackhawk Fm. and Lower Castlegate Sandtone foreland basin-fill is associated with one of the latest compression events (Schwans, 1995).

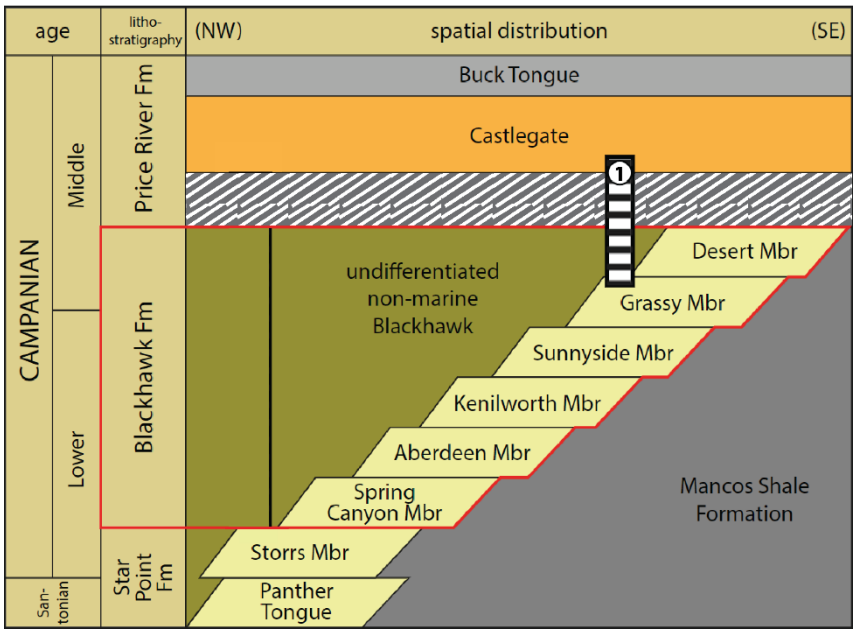

Figure 2.1.1 Illustration of Late Cretaceous stratigraphy (formations and members) in the Book Cliffs. The Blackhawk Fm. is outlined in red. Shallow-marine members are marked as yellow boxes. The focus in this study is the non-marine Blackhawk (marked as green). (1) shows where in the stratigraphy acquired log is from. Stratigraphy below Castlegate is eroded and marks a hiatus. Modified from Howell and Flint (2003b); based on Young (1955).

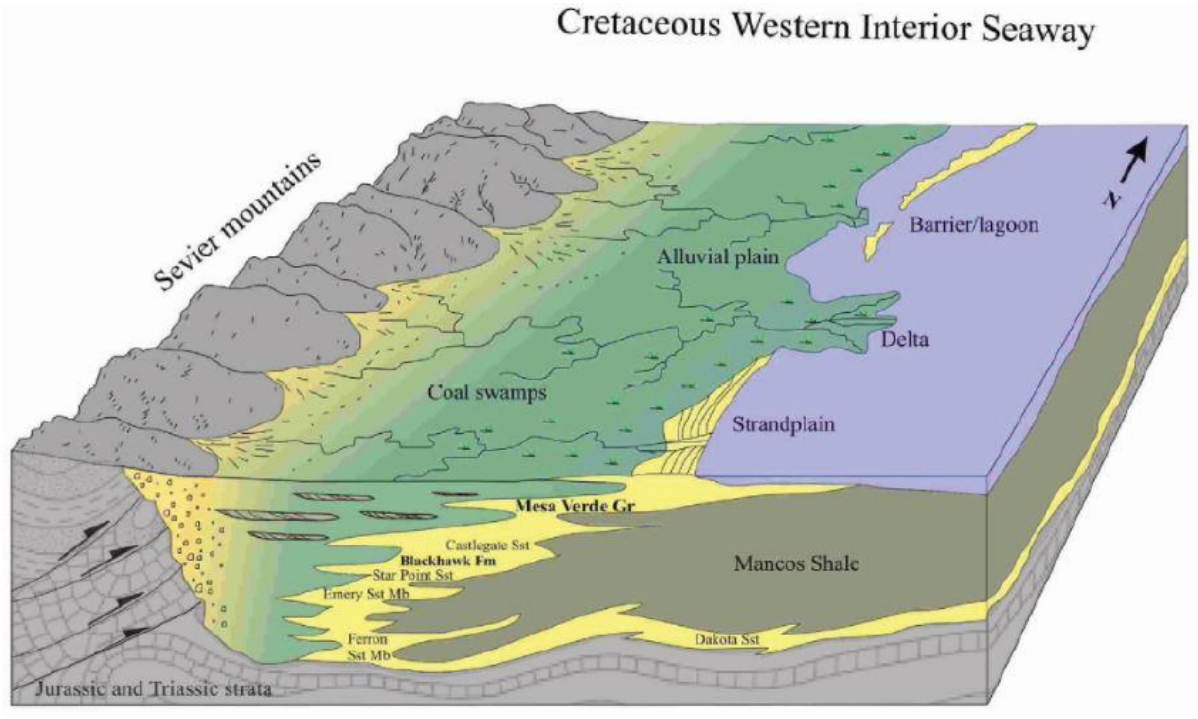

Figure 2.1.2 This block diagram shows the Late Cretaceous depositional environments in Utah. The shallow- marine members and formations are listed in stratigraphic order within this figure. The green area shows the non-marine environment of coal swamps and alluvial plain that is further studied in this thesis. This figure is modified from Hintze (2005) by Knudsen (2008).

The foreland basin-fill of the Sevier Orogen was deposited along the western shoreline of the Western Interior Seaway, which was a large north-south trending epicontinental sea that developed in North America during a period in Cretaceous with very high sea level (Haq et al., 1988; Rittersbacher et al., 2014b). The basin of the Western Interior Seaway is one of the largest, best preserved and most studied sedimentary basins in the world (Miall et al., 2008). The basin was formed due to a combination of short-term loading and depression of the Sevier Orogen in the west (Miall et al., 2008) and more long-wavelength dynamic subsidence from pulling of the oceanic Farallon slab below (Liu et al., 2011). The subsidence and the rising sea level, lead to a flooding from both the north and the south of the North American continent (Kauffman & Caldwell, 1993).

During Late Cretaceous, the transition from marine to non-marine deposits was accelerated by shifting of the tectonic style along the subduction zone in the west (Howell & Flint, 2003a). The

angle of subduction was reduced, which lead to a slower, broader and more extensive subsidence (Kauffman & Caldwell, 1993). Even though the deposits of today's Book Cliffs has been uplifted by at least 6000 m, the area has undergone no significant tectonic deformation (Howell & Flint, 2003a; Rittersbacher et al., 2014a). This allows the stratigraphy and stratal relationships to be studied and traced for several kilometres, which is unique for any foreland basin-fill in the world (Howell & Flint, 2003a; Miall et al., 2008).

2.2 Stratigraphy and sedimentology

The Mesa Verde Group is the name used to gather all the different shallow-marine sediments that were deposited along the western side of the Western Interior Seaway (Swift et al., 1987). In the Book Cliffs, the group is further divided into the Star Point and Blackhawk formations. The Blackhawk Fm. is comprised of six members where each member represents a shallow-marine sandstone wedge, separated by interfingering tongues of the offshore Mancos Shale (Young, 1955). Each member is further divided into parasequences, which is smaller-scale progradational sandstone tongues separated by flooding surfaces during minor transgressions (Hampson & Howell, 2005; Van Wagoner et al., 1990). Overlying the shallow-marine sediments, is a thick package of non-marine coastal plain- and fluvial deposits connected to each shallow-marine wedge, which pinches out basinward (Swift et al., 1987). This is referred to as the undifferentiated non-marine Blackhawk and is unconformably overlain by the Castlegate Sandstone of braided fluvial origin (Van Wagoner, 1991). The overall architecture of the Blackhawk Fm. shows a large-scale progradation of a delta during a long-term relative sea level rise (Young, 1955).

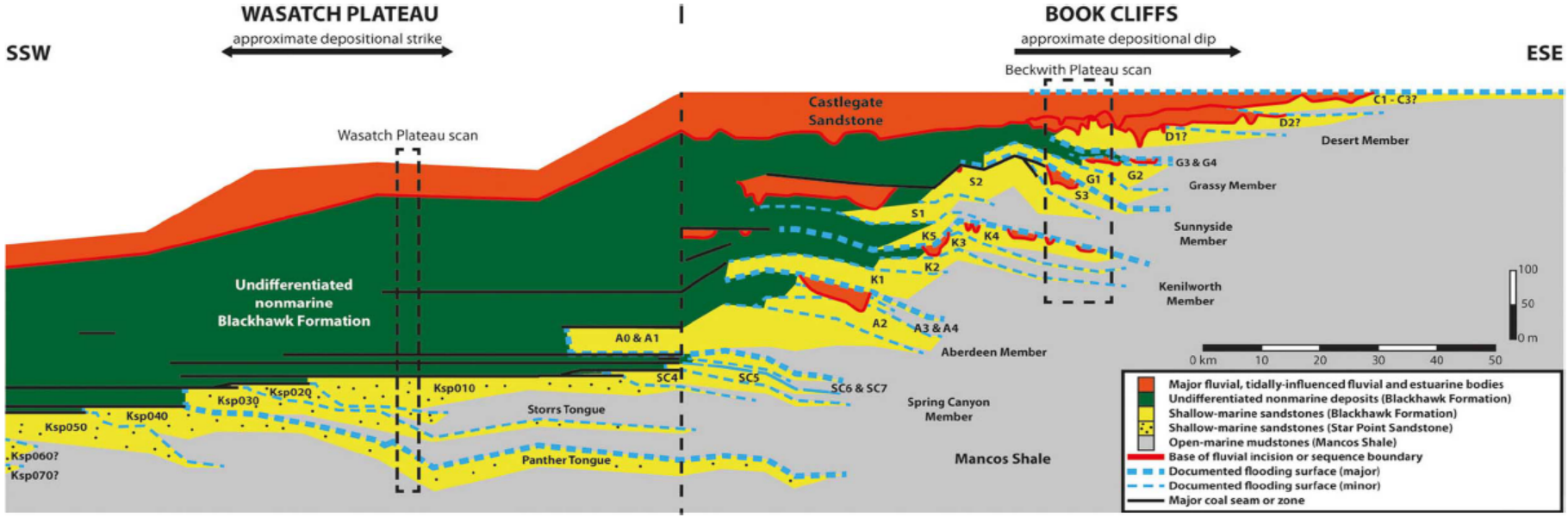

Figure 2.2.2.1 Stratigraphic summary in cross section of the Wasatch Plateau and Book Cliffs. The shallow-marine members of the Blackhawk Formation are coloured yellow, the non-marine is in green and the Castlegate Sandstone is orange. This show how much thinner the studied non-marine deposits are in the Beckwith Plateau scan compared to the Wasatch Plateau scan. Modified by Eide et al. (2015) after Hampson et al. (2012).

The sediment source of the Book Cliffs was from the uplifting of the Sevier Orogenic Belt (DeCelles & Coogan, 2006; Horton et al., 2004). The depositional system that fed sediments to the wave-dominated shoreface in the Blackhawk Fm. consist of alluvial plains with distributive fluvial channels (Rittersbacher et al., 2014b). The erosion and transport of the sediments was increased by the climate at that time, as the paleolatitude was approximately 42°N (Kauffman & Caldwell, 1993). Flora from the non-marine Blackhawk Fm. suggest that the climate during the deposition was warm temperate to subtropical (Kauffman & Caldwell, 1993).

The non-marine Blackhawk Formation comprises a succession of interbedded coals, mudstones and sandstones (Hampson et al., 2012; Young, 1955). The coal seams can be observed in metre-scales throughout the non-marine part of the formation and indicate that the climate was seasonal and warm during deposition, typical for temperate to subtropical climates (Hampson et al., 2012; Parker, 1976). The mudstones are often rooted and the sandstones are either thinly (< 1 m) sheeted or in lenticular shapes (typically <10 m thick and 1 km wide) (Hampson et al., 2012). The environment has been interpreted to a coastal plain with deposits of floodplain, crevasse-splay and fluvial or distributary channel-fill (Adams & Bhattacharya, 2005; Hampson et al., 2005). The size and abundance of the fluvial sandbodies increase from the base to the top of the formation, where several of the channels have multilateral and multistorey architecture (see section 4.4 for further description) (Hampson et al., 2012).

3 DATA AND METHODS

The main dataset of this thesis consists of 31.7 km of virtual outcrop data from two outcrops named the Beckwith Plateau and the Wasatch Plateau. The geological interpretations from the virtual outcrop data is constrained and verified by a set of four lithological logs acquired in the field, in total 153 m.

This data is used to generate synthetic seismic images using ray-based 2(3)D convolution, and subsequently compared to real seismic data from The Barents Sea. The datasets and methods mentioned above are described in this section, and important papers are referred to. In the end of the chapter, the full workflow used in this thesis is described.

3.1 Lidar data

The main dataset of this study is a high-resolution virtual outcrop model, which is from an oblique helicopter-mounted laser scanning of the Beckwith Plateau. The method of collecting this kind of data is known as light detection and ranging scanning, or "LiDAR"-scanning. LiDAR-scanning makes it possible to collect large quantities of accurate geometric data from depositional elements located in inaccessible cliffs, like in the Book Cliffs. LiDAR can be acquired either through scanning from the ground or from the air. Terrestrial LiDAR is used in geosciences for small-scale outcrop studies, where 3D visualisation of vertical cliff sections and extraction of accurate geobody dimensions is necessary (Rittersbacher et al., 2014a). But the terrestrial LiDAR has a limited range of the scanner and are not very efficient for outcrops that have a larger horizontal extent than 5 km, while airborne LiDAR can acquire data for several kilometres efficiently (Rittersbacher et al., 2014a). The angle from the scanner to the outcrop can also be a problem for terrestrial scans, whereas a side-looking scan from a helicopter much easier can provide an optimal view of the cliff (Buckley et al., 2008b).

The LiDAR system has several components that work simultaneously to collect data of the same area. A laser scanner sends out a laser pulse that bounces off the target and returns to the detector, which records distances and angles to a target (e.g. an outcrop) and determines

the XYZ coordinates of these data points at the same time (Bellian et al., 2005; Rittersbacher et al., 2014a). The system records hundreds of thousands of points per second, which result in a point cloud (Bellian et al., 2005; Rittersbacher et al., 2014a). The point cloud can be used to describe the topography, but in order to interpret geological details, is a digital camera built in to give a further photorealistic description (Bellian et al., 2005; Buckley et al., 2008b; Rittersbacher et al., 2014a). The camera is used simultaneously with the laser scanner at matching field view, so the point clouds and images are merged together to a "virtual outcrop" (Bellian et al., 2005; Buckley et al., 2008b; Rittersbacher et al., 2014a). The laser scanner used in this virtual model is a Riegl LMS Q240i-60 airborne laser scanner, encapsulated in the Helimap System (as shown in Figure 3.1.1) (Buckley et al., 2008b; Eide et al., 2014; Rittersbacher et al., 2014a), which is a LiDAR system described in detail by Vallet and Skaloud (2004). As the input data in this project is a complete virtual outcrop model, the detailed methodology of the acquisition and post-processing of LiDAR data will not be further described. This has been documented well in earlier papers (e.g. Bellian et al., 2005; Buckley et al., 2008a; Enge et al., 2007; Verwer et al., 2007; Verwer et al., 2009; Wilson et al., 2009). Further description of workflow in terms of collecting and processing LiDAR data captured obliquely from a helicopter is documented by Buckley et al. (2008b) and Rittersbacher et al. (2014a).

Figure 3.1.1 Photo of equipment used in acquisition of the airborne LiDAR data used in this study. This is a Riegl LMS Q240i-60 airborne LiDAR scanner including Hasselblad H1 22-megapixel camera, GNSS antenna and inertial measurement unit. The equipment is mounted on a commercial helicopter. From Rittersbacher et al. (2014a).

The resolution of the model depends on the setup used during the LiDAR scan. The setup used for collection of data of the Beckwith Plateau, is almost identical to what is used in the LiDAR scanning of the Wasatch Plateau in the studies by Buckley et al. (2008b), Rittersbacher et al. (2014a) and Eide et al. (2014). In the Wasatch Plateau scan, the distance between the outcrop face and the helicopter while scanning was 300 – 400 m. Between each point in the point cloud is a distance at around 30 cm, where the image resolution has a pixel of around 7 cm. Such high resolution makes it possible to see geological features at a high level of detail.

The 5.3 km of the northernmost part of the Beckwith Plateau (Figure 3.1.2) is main focus area in this study, while the rest of the available virtual outcrops are used as supplements to increase the understanding. The restricted area is due to limited available computer resources, which has trouble simulating when the seismic models are too large. The reason for why this specific part is chosen, is that the non-marine Blackhawk Fm. in this interval contains the channelized fluvial sandbodies this study aims to model. The non-marine Blackhawk Fm. pinches out further south, which makes the modelling area thinner, while the more sheet-shaped sand deposits in the formation in the Wasatch Plateau do not contain the same architectural elements.

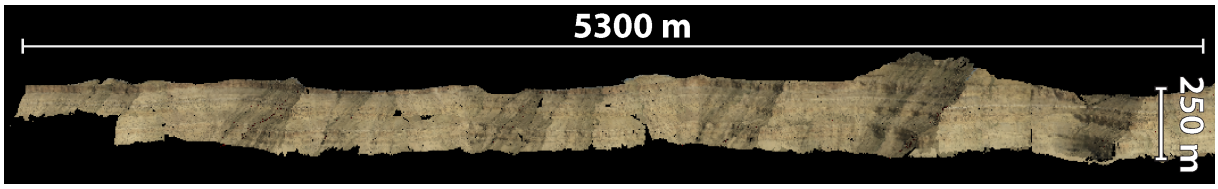

Figure 3.1.2 Virtual outcrop model of the northern Beckwith Plateau, used as the main input data in this study.

Interpretation of the virtual outcrop model is completed through these following steps: (1) Map the key stratigraphic boundaries (flooding surfaces) to identify the stratigraphic framework and the main members and parasequences in the formations. (2) Map the extent of the depositional elements and interpret their respective depositional environment within each parasequence. (3) Interpret and map the architectural features within the deposits, focusing on the fluvial architecture in this study.

3.2 Geological model and elastic properties

After outlining the depositional elements and surfaces in the virtual outcrop model, a more complete geological model needs to be established. Since this study aims to generate 2D synthetic seismic, the 3D outcrop model must be converted into a 2D panel of the outcrop. The next step is to use photo editing software (in this study, Adobe Illustrator) to assign different colour blocks to the outcrop-panel, based on the different interpreted lithologies (Figure 3.2.1). The reason for dividing the model into blocks, is so the elastic properties associated with the lithology can be assigned to a specified colour block. To simplify, the coloured geological model is turned into greyscale, so each block can have an own black/white ratio code.

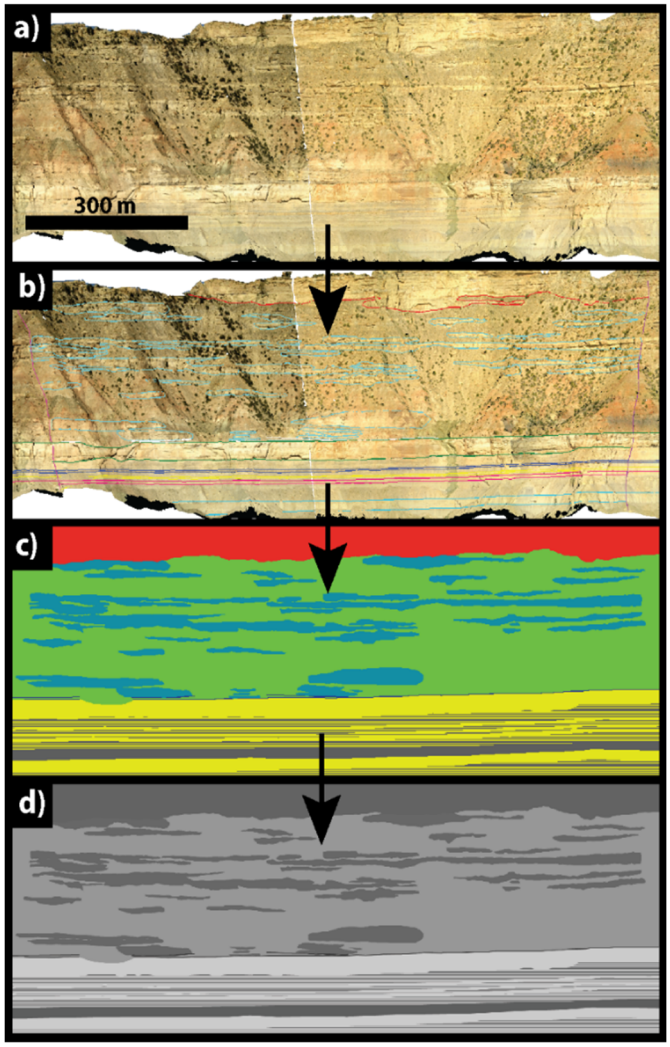

Figure 3.2.1 Workflow of making a geological model from an outcrop, using the Wasatch Plateau as an example. (a) Clean and uninterpreted virtual outcrop model. (b) Mapped surfaces and geometries of depositional elements on top of LiDAR-data. (c) Colour-filled depositional elements based on interpreted geometries and lithology. (d) Greyscale version of colour-filled geological model.

The response of seismic waves is dependent on the elastic moduli of the material, where the variable properties are velocity (P- and S-wave) and density (Haskell, 1953). As this study aims to compare the generated synthetic seismic with real seismic, the input of elastic properties are collected from offshore well data on the Norwegian continental shelf (mainly from the Barents Sea) (Table 1). If well log data from mapped formations in the outcrop would have been available, the synthetic seismic would have reflected how the outcrop with the actual properties could have looked in seismic. Instead, the model shows how a reservoir with the geometries of the outcrop could have looked if it was located in the subsurface offshore Norway. The analogue formations used as input data, are chosen because of similar lithology and similar environments of deposition to what has been interpreted in the outcrop. Information about lithology and interpreted depositional environment of the different formations are gathered from the FactPages of the Norwegian Petroleum Directorate (2018). The density log is used to describe density, while the sonic log is converted and used for P-wave velocity. The S-wave velocity for different facies associations is calculated by using Vp/Vs-ratios from the Troll field (Buland et al., 1996) and the Barents Sea (Golyan, 2012).

Table 1 Input of elastic properties to the seismic modelling. Properties are from offshore wells on the Norwegian continental shelf that penetrates formations with analogue depositional environments.

Facies Association	Analogue Formation	Well	Density (g/cm^3)	Vp (km/s)	Vp/Vs	Vs (km/s)
Fluvial channelized sandbody	Snadd Fm. (Kapp Toscana GP)	7223/5-1	2,56	4,41	1,7	1,42
Heterolithic (siltstone-layer)	Snadd Fm. (Kapp Toscana GP)	7223/5-1	2,33	3,58	1,7	2,11
Heterolithic (generalized)	Snadd Fm. (Kapp Toscana GP)	7223/5-1	2,42	3,80	1,7	2,23
Coal	Soldogg Fm. (Billefjorden GP)	7128/4-1	1,39	2,98	2,1	1,42
Coastal Plain	Snadd Fm. (Kapp Toscana GP)	7223/5-1	2,40	2,88	2,5	1,15
Braidplain	Statfjord Fm.	16/2-15	2,18	3,12	1,7	1,83
Shoreface	Stø Fm. (Kapp Toscana GP)	7119/12-2	2,28	3,45	1,7	2,03
Offshore	Knurr Fm. (Adventdalen GP)	7119/12-2	2,51	3,07	3,0	2,11

The greyscale geological model and corresponding the elastic properties are joined together in the numerical computing software MATLAB. In the software, a programming script made by Schmid (2016), later modified by Lecomte (2016) and the present author to import the greyscale model and connect each black/white ratio code to specific density-, Vp- and Vs-values. The output of the script is then four individual property models showing their values embedded with the geological model; density-model, Vp-model, Vs-model and a block-model. The block model shows how the geological model is divided into a number of faceis associations based on lithology. The output-format of these models is SEG-Y-files, which is a format for storing geophysical data (Society of Exploration Geophysicists, 2002). The same format is used for input of data in the synthetic seismic modelling.

3.3 Synthetic seismic modelling

Synthetic seismic modelling is used to simulate the seismic response of an earth model. Most seismic modelling studies use input models that have similar detail-level as the standard seismic image samplings (only details larger than a few metres). However, when using high-resolution virtual outcrop models of seismic-scale outcrops as an input, it is possible to map a detail-level much finer than expected seismic resolution to better analyse what influence such details have in the seismic response. In forward modelling of seismic, there are two main classes for 2(3)D geological structures: full-wavefield and ray-based (Lecomte et al., 2015). Each approach is widely used and has both advantages and drawbacks. The full-wavefield method is however often considered as the ideal seismic modelling strategy, as it results in complete synthetic seismograms ready to use for processing and imaging tests (Lecomte et al., 2016).

Some of the main reasons for why ray-based modelling is used in addition to full-wavefield, is that full-wavefield is very time-demanding and requires high computer-cost, whereas ray-based approach rapidly and efficiently generates synthetic seismograms for user-selected wave phases (e.g. P-wave, S-wave, reflection, transmission conversion, etc.) (Lecomte et al., 2015). Even though some wave types and phases (e.g. headwaves, surface waves, multiples, etc.) might be missing in this approach, this study will only use the ray-based modelling due to restricted computer resources and time. The method will only be briefly reviewed in this

thesis as more detailed description is available in other studies (Lecomte, 2008; Lecomte et al., 2015; 2016).

Ray-based modelling relies on high-frequency approximation of the wave equation and then solve the latter along ray paths. Once this is done, the obtained information in form of travel times, amplitudes, etc., is used to generate synthetic seismograms by convolution with a wavelet. The simplest form of such approach is 1D convolution, which is a well-known method commonly used in industry (Lecomte et al., 2015). The reason is that 1D convolution efficiently generates post-stack time-migrated seismic sections, which is more suited for interpretation (Lecomte et al., 2015). The seismic traces of the section are generated individually by convolving each vertical reflectivity log with the user-selected wavelet (as shown on the right side in Figure 3.3.1). The traces are then plotted side by side in a time section, which then approximates a post-stack time-migrated section. Some of the advantages of using 1D convolution are that it is very efficient and gives a good estimate of the vertical resolution. A drawback is that the concept originates from a simple geological model, i.e., homogenous horizontal layers, and do not consider lateral velocity variations, lateral resolution effects and lack of illumination for e.g., steep geological dips (Lecomte et al., 2015).

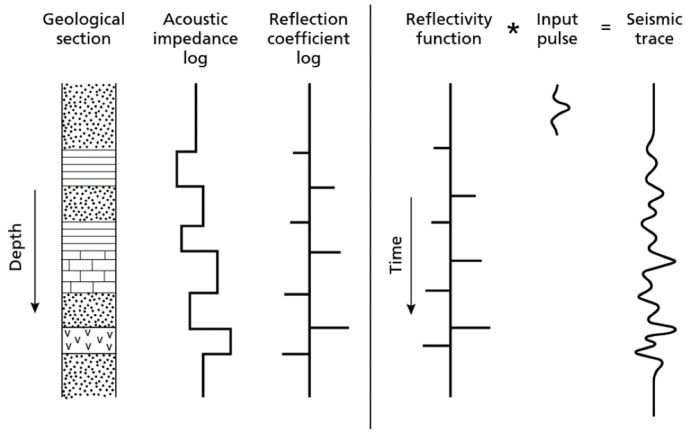

Figure 3.3.1 Illustration of convolution of a reflection function with an input pulse, to get a seismic trace in time domain (right side). The relationship between the reflectivity function and the different physical properties in geological layers in depth domain is also illustrated (left side). Figure from Kearey et al. (2002)

Another ray-based modelling is using Point-Spread Functions (PSF) for 2(3)D convolution and directly generate prestack depth migration (PSDM) images (Lecomte, 2008). PSDM is often the ultimate goal in seismic processing, as it provides directly depth images of the subsurface

reflectivity, hence being closer to the geological structures. The PSF is the 2(3)D response of a diffraction point in PSDM-type seismic imaging; it is convolved with the input 2(3)D reflectivity model to get the simulated PSDM seismic images from that model (Figure 3.3.2).

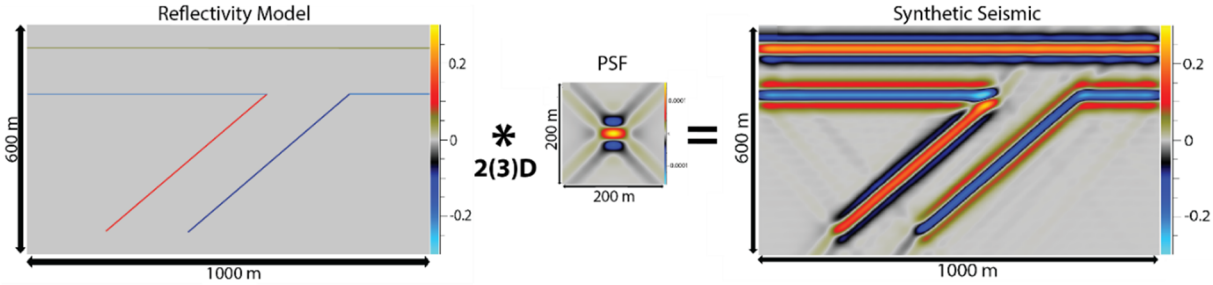

Figure 3.3.2 Basic illustration of how 2(3)D convoluted synthetic seismic is generated. The two main components are the reflectivity model and the PSF. These are convoluted to generate the PSDM simulated synthetic seismic image. Model courtesy of Grimstad (2018).

The PSF-based 2(3)D convolution modelling differs from a 1D convolution as the seismic is not generated trace by trace (each reflectivity log thus being considered independently from its neighbours) but as a whole model at once. Such automatically accounts for lateral resolution

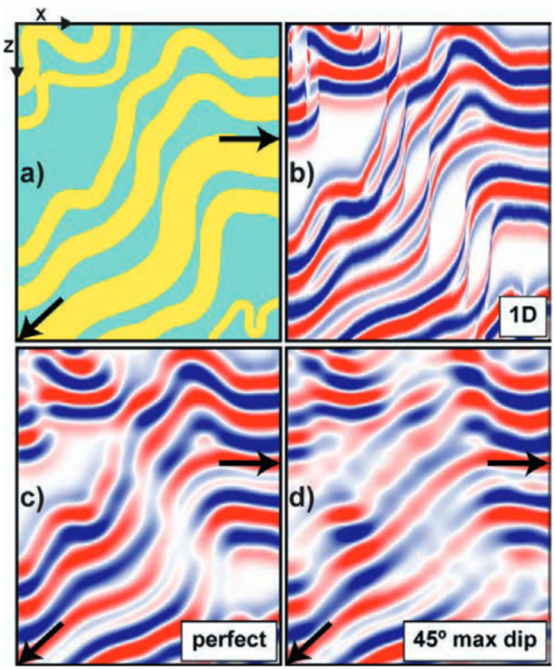

Figure 3.3.3 Example showing the difference between 1D convolution and 2(3)D convolution of the same model. (a) A zoomed acoustic impedance image (blue=high, yellow=low) of folds, used as an input to both convolutions. (b) Seismic image using 1D convolution. A thinning effect is visible at the steepest parts of the folds. (c) and (d) shows the resulting seismic image using 2(3)D convolution, where (c) uses a perfect illumination that can illuminate all reflector dips and (d) corresponds to partial illumination, i.e. with reflectors illuminated up to 45° in dip but not higher. The thinning effect is removed by 2(3)D convolution. Figure from Lecomte et al. (2016).

effects and illumination issues, instead of just vertical resolution as in 1D convolution (Lecomte et al., 2016).

2(3)D convolution uses PSF that is generated from the illumination vector (I_{SR}) at a reference target point (usually taken as the centre of the seismic image to generate). The illumination vector I_{SR} is a result of the difference between two slowness vectors at that reference point; the slowness vector towards the receiver (P_R) and the slowness vector from the source ($-P_S$) (Equation 1).

$$I_{SR} = P_R - P_S \quad (1)$$

The slowness vector is a local vector perpendicular to the wavefront at the reference point (both for isotropic and anisotropic media). It is called "slowness" because its length is defined as $\frac{1}{velocity}$ (i.e., slowness), where the velocity is the one at the reference point. The slowness vectors are calculated in a background velocity model (e.g., the migration-velocity model), which is a smooth version of the actual velocity field. The slowness vector in an isotropic media is always parallel with the raypath of the waves from a source or towards a receiver, but it is not necessary parallel to raypaths in anisotropic media (see Figure 3.3.4 for illustration of slowness vectors and raypaths in isotropic media).

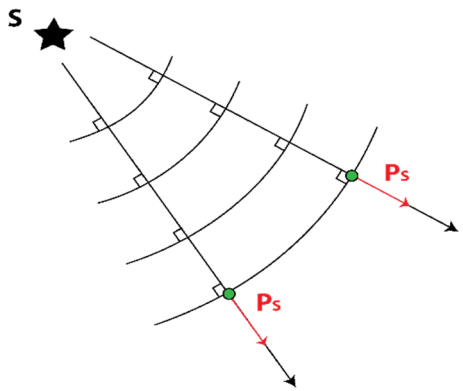

Figure 3.3.4 Illustration of how slowness vectors (red P_S vectors) are locally oriented from the target points (green dots) in an isotropic media. P_s vectors are in that case parallel with the raypaths (black arrows), which are perpendicular to the wavefronts from the source (S).

The length and orientation of the I_{SR} describe the resolution and illumination effects in the seismic imaging (Figure 3.3.5a). Both the velocity, which defines the length of slowness vectors

(P_R and P_s), and the opening angle (θ_{SR}) between P_R and -P_S, control the length of the I_{SR}. θ_{SR} is function of the offset (distance) between source and receiver: if source and receiver coincides (zero-offset case), θ_{SR} is zero and the corresponding I_{SR} is at its longest. A longer I_{SR} reflects a higher resolution, which can be best achieved in the case of low velocity and/or small θ_{SR}. This means that a high background velocity and/or long offsets will lead to low resolution. In addition, the orientation of the I_{SR} tells which reflector dip nearby the reference point will be illuminated. If a reflector is orientated perpendicular to the I_{SR}, it will be imaged and the corresponding incident angle (θ_i) from Snell's law is defined by $\frac{\theta_{SR}}{2}$.

In a given acquisition survey where the raypaths from the source (S) and to the receiver (R) will vary, the I_{SR} will have a span of orientations (See Figure 3.3.5b for illustration of I_{SR} span). The span will then reflect the range of reflector dips that can be illuminated near the target point; in Figure 3.3.5, only reflectors with a dip between 0° and 45° can be illuminated by the calculated PSF. The lateral resolution is controlled by the lateral width of the span, which has lowest resolution for small span-widths and corresponding small maximum illuminated dip. The span is dependent on the background velocity model and the survey geometry. If these factors are not available in the modelling, a generic I_{SR} span is created. The input in the generic span is an average velocity (V) of the target, an incident angle (θ_i), and a maximum reflector dip to illuminate.

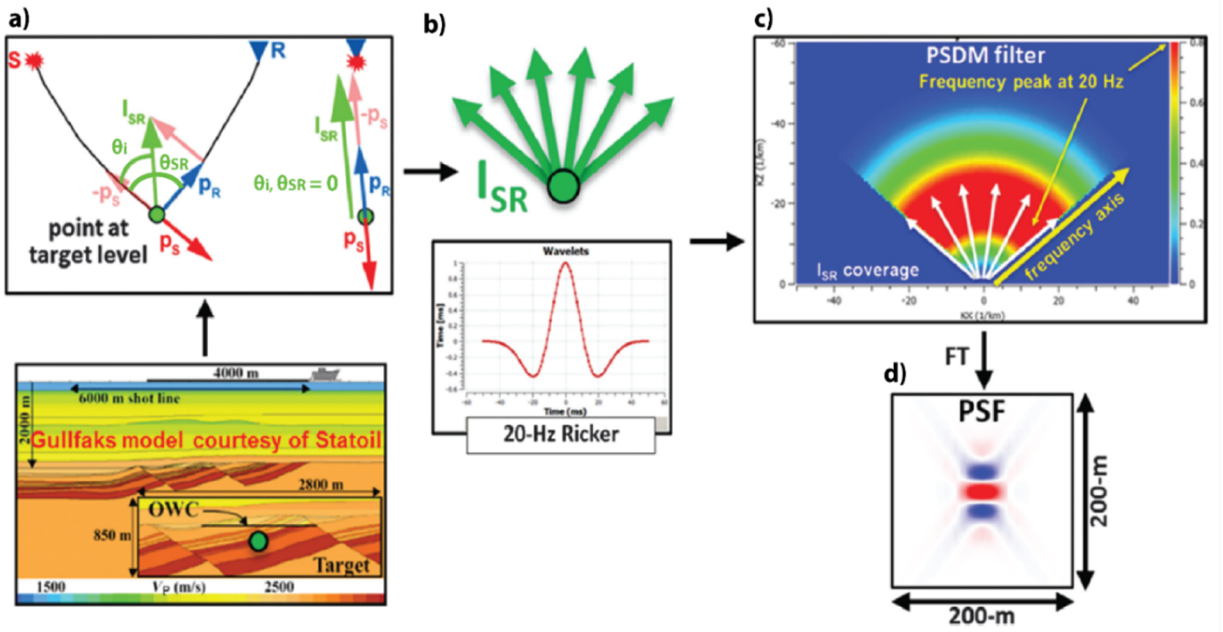

Figure 3.3.5 The basic elements and workflow of 2(3)D spatial prestack convolution. (a) Velocity model based on the geology of the Gullfaks field and illustration of how the I_{SR} is calculated based on p_R and $-p_S$ at a target point (green dot), both with an offset and with a zero-offset. (b) Illustration of how I_{SR} span at a target point would look in a survey and a figure of the selected frequency wavelet. (c) Corresponding PSDM filter for such I_{SR} and wavelet; the maximum illuminated dip is 45° in that case. (d) The resulting PSF after performing a Fourier transformation on the PSDM filter. Modified from Lecomte et al. (2015)

The next step in 2(3)D convolution after calculating illumination vectors (I_{SR}), is to use them along with the wavelet frequency (f) to generate scattering wavenumber vector (K_{SR}) (as shown in Equation 2).

$$K_{SR}(f) = f \times I_{SR} \qquad (2)$$

By calculating K_{SR} for the whole I_{SR} span, a resulting PSDM filter is generated in the wavenumber domain (Figure 3.3.5c). A PSDM filter can be used to describe the resolution, illumination and scattering in the wavenumber domain, but in order to translate this information into space domain as a point spread function (PSF), the PSDM filter needs to be Fourier Transformed (FT) (Figure 3.3.5d).

As this study has limitations in time and resources, a few pre-set parameters have to be made. Firstly, a ray-based modelling approach is chosen over the more complete full-wavefield approach. Furthermore, the focus is to use 2(3)D convolution over 1D convolution as there are expected lateral variations in the target area between coastal plain mudstone and fluvial

sandbodies. In the convolution process, no background velocity model or survey geometries are provided and therefore a generic I_{SR} span needs to be created. In the generic I_{SR}, the incident angle (θ_i) is set to 0° which means that the source (S) and receiver (R) are at the same location (zero-offset acquisition). Even though this is not normal in real seismic acquisition, this is used in this study to get a best possible illumination of the I_{SR} span, but we should keep in mind that larger offsets (i.e., larger incident angles) would correspond to worse resolution. The average velocity in the target area is calculated to be 3.64 km/s.

The selected wavelet type is a zero-phased Ricker wavelet (Ricker, 1940) in a positive standard polarity (Sheriff & Geldart, 1995), where increase in acoustic impedance is visible as red peaks and decrease in acoustic impedance is blue troughs. For the settings of maximum reflector dip to illuminate, this is set to maximum ±45° dip. This setup will give a PSF with a vertical resolution of a quarter wavelength ($\lambda/4$) and a lateral resolution of a half wavelength ($\lambda/2$), as quoted in literature to be the realistic and ideal setup (Simm & Bacon, 2014; Widess, 1973). The vertical resolution of $\lambda/4$ also defines the tuning thickness (Equation 4), which is the bed thickness where two events become indistinguishable (Widess, 1973). The tuning thickness is calculated by Equation 3 and Equation 4.

$$tuning\ thickness = \lambda/4 \qquad (3)$$

$$\lambda = \frac{V_p\ (m/s)}{F_d\ (Hz)} \qquad (4)$$

Where λ = wavelength (m), V_p = average P-wave velocity and F_d = dominant frequency (Simm & Bacon, 2014).

The sampling-resolution of the input-outcrop is set to every 25 cm, both laterally and horizontally, which is very detailed considering the whole outcrop is 5300 m long and 250 m high. All the amplitudes in the seismic images are shown within the scale of 70 % of max amplitude and -max amplitude, as each frequency has a different amplitude spectrum. This is to better visualise where the strongest and weakest amplitudes are located, where 70 % of the max spectrum is the percentage that shows this best. All the figures from the Beckwith Plateau in chapter 5 Results and 6 Discussion, both input-models and synthetic seismic, are vertical exaggerated by a factor of 6.5.

The results of the generated synthetic seismic needs to be interpreted. As the author of this thesis knows the input model that are used to generate the synthetic seismograms, the interpretations made from the synthetic seismograms could be influenced by this *a priori* information. In order to assess how the synthetic data would be interpreted by a geologist who did not know the input models, a group of nine selected people with a background in seismic interpretation participated to do a survey. The participants were asked to interpret fluvial channel deposits within the synthetic seismic images generated in this study. The participants had a general knowledge of seismic interpretation, but with varying experience and had positions such as geology professors at the University of Bergen, geologists at Equinor and Aker BP, PhD- and master students. The aim of the survey was to get an objective overview of how fluvial channel deposits would be interpreted at different resolution.

3.4 Analogue seismic data

The generated synthetic seismic is compared with real seismic data from the Barents Sea. Four 3D-seismic datasets have been available for comparison in this study. Three of the datasets (hereby referred to as A, B and C) are located on the Bjarmeland Platform and one (referred to as D) on the Finnmark Platform (see Figure 3.4.1 for an overview map of the datasets). There are discoveries within three of these datasets, the Caurus-discovery in dataset A, the Obesum-discovery in dataset B and the Arenaria-discovery in dataset C (all of these are unlikely to enter production, as they are currently considered non-commercial) (Norwegian Petroleum Directorate, 2018). The depth level of interest is in the interval of the Triassic deposits, which is covered both by seismic and well data in all datasets. The Snadd Formation within this interval contains seismically visible and well-preserved fluvial channel deposits, and are therefore especially used in this study to compare with the fluvial channel deposits in the Blackhawk Fm. The reason for why these Triassic deposits in the Barents Sea are chosen as analogue data, is that the deposits are both very little affected by tectonic activity and are located at relatively shallow depths. This results in seismic reflections that are rather horizonal, lateral continuous and with higher resolution compared to deeper and tectonic affected areas, like the Brent Delta in the North Sea (Jackson et al., 2010).

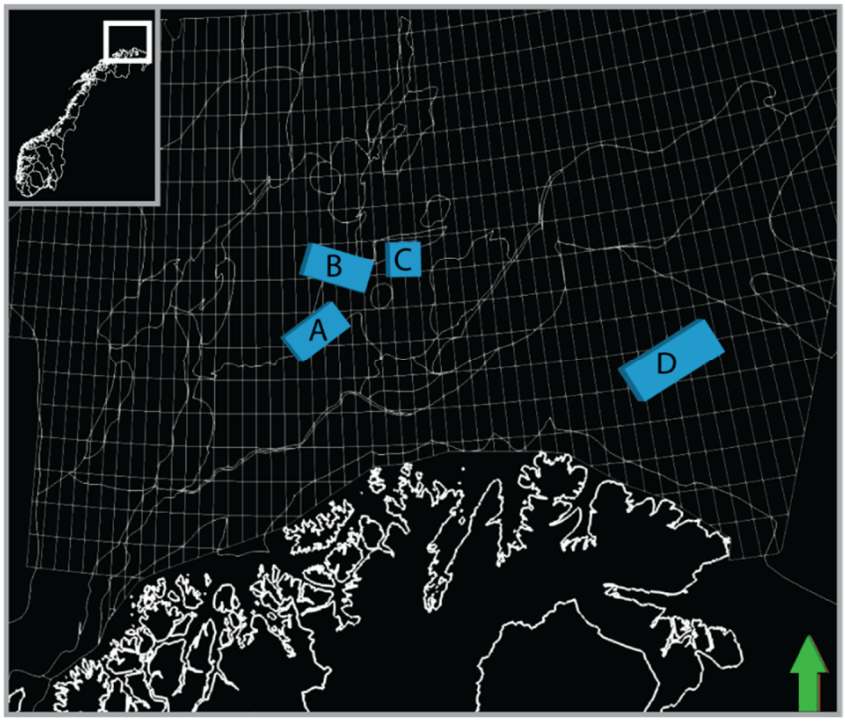

Figure 3.4.1 Overview map of the Norwegian licence area in the Barents Sea. The four available seismic datasets in this study are marked with A, B, C and D.

The seismic is interpreted in the software Petrel. In addition to comparing seismic reflections, different volume- and surface attributes have been applied. The purpose of these attributes is to identify channel complexes in the seismic and illuminate their geometries and properties. Interpreting channel complexes in the Barents Sea is not a main objective of this thesis, rather, the seismic has been used as an analogue and real-world ground-truth of the synthetic seismic models.

3.5 Workflow – From outcrop to seismic

Going from interpretation of sedimentary units and elements of the virtual outcrop to a seismic image are done using these following six steps (Figure 3.5.1):

1. Interpretation of virtual outcrop, where extensive surface boundaries are interpreted first. After the non-marine part of the Blackhawk Formation is identified, a more thorough and detailed interpretation is done within this unit (focusing on outlining elements connected to fluvial channels). After interpretation, the resulting outcrop

model with the overlying interpretation lines are projected as a 2D-panel that is parallel with the outcrop face and exported as a graphic file (PNG-format) (Figure 3.2.1a-b).

2. The image file is then imported to a photo editing software (in this study, Adobe Illustrator). Here are the interpreted stratigraphic elements outlined again and filled with a specific colour according to their lithology (Figure 3.2.1c). The elements with the same colour are now referred to as “blocks”.
3. After the whole image is colour-filled and all the elements are assigned to a block, is the colour image turned into greyscale (Figure 3.2.1d and Figure 3.5.1a). This is so each block is assigned a specific black/white-ratio number to be mathematically identified by.
4. Elastic properties (density, P-velocity and S-velocity) are assigned to each block. Available well log data are investigated to find appropriate properties to the block and their associated facies. The selected log data intervals are also verified by their connected well cores and previous depositional environment interpretations (available from Norwegian Petroleum Directorate (2018)) (Figure 3.5.1b).
5. The greyscale image is imported in MATLAB, where a script is made to connect the elastic properties to the specific block by using the black/white ratio number. The export products of the fusion, are four models; block-, density-, p-velocity- and s-velocity model. These are exported as SEGY-files (Figure 3.5.1c).
6. The SEGY-files are imported to SeisRoX as properties. A 2D target model is built by using these properties. User-settings like average velocity of wanted target, incident angle, max reflector dip illuminated and wavelet frequencies are then set before generating a reflectivity and seismic models (Figure 3.5.1d).

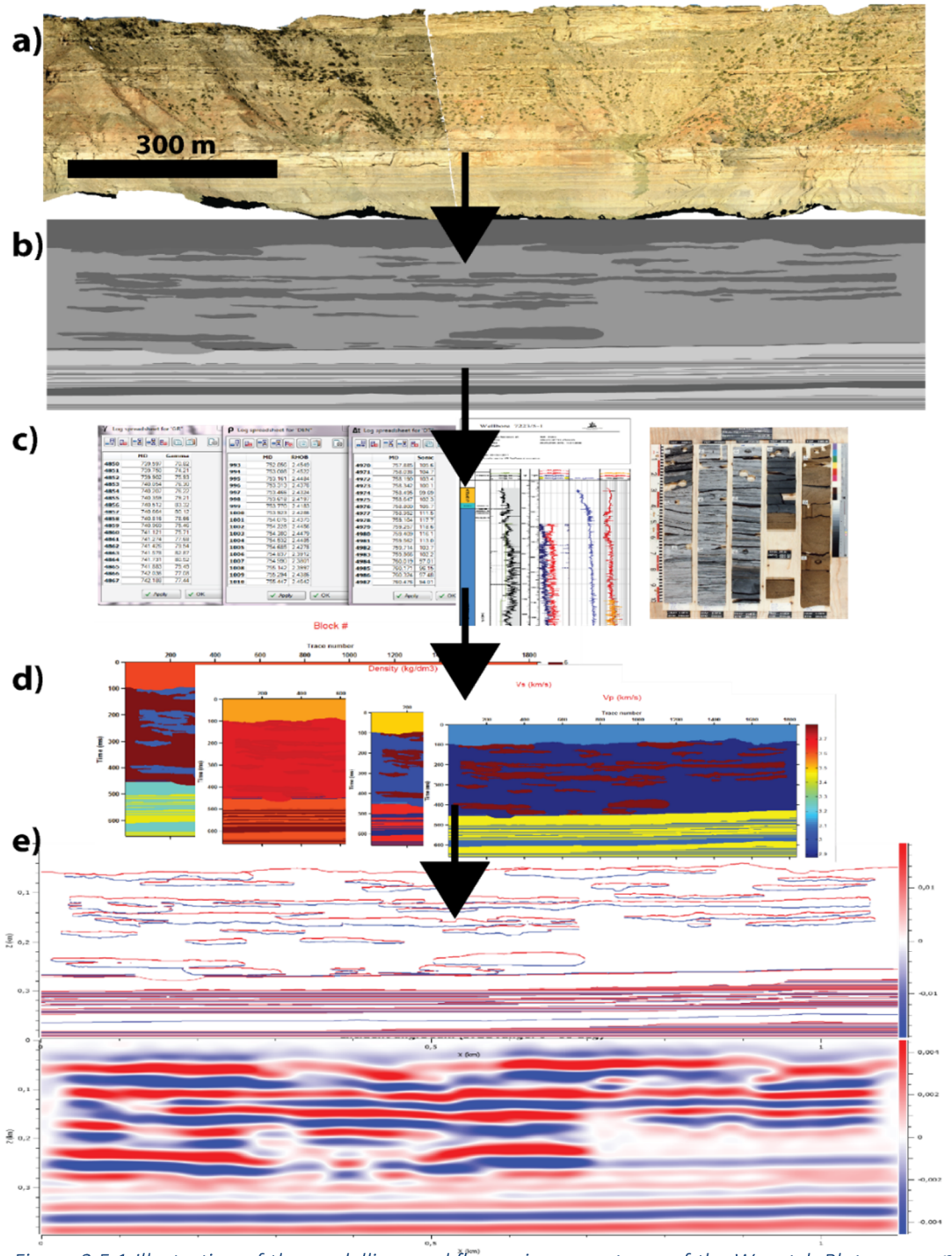

Figure 3.5.1 Illustration of the modelling workflow using an outcrop of the Wasatch Plateau as an example. (a) Virtual outcrop model on a 2D panel. (b) Greyscale image of the outcrop (modelling workflow from outcrop (a) to greyscale (b) is previous illustrated in Figure 3.2.1). (c) Finding properties from real well data that fits with the interpreted elements in the outcrop, using data from logs, interpretations and cores. (d) Connecting the greyscale model with the chosen well data by generating block-, density, S-velocity- and p-velocity models. (e) Using property models along with user-selected variables to generate reflectivity- and seismic images.

4 SEDIMENTOLOGY OF STUDIED DEPOSITS

In this chapter, sedimentological properties of the studied deposits are explained. First, the large-scale architecture will be enlightened, which is mainly based on interpretations from the LiDAR-data in the virtual outcrop. Secondly, the focus is on smaller-scale architecture, which is based on sedimentary logs. The observations from the large- and small-scale architecture are then composed together to a number of facies associations presented in a table. Finally, the sedimentology of fluvial deposits is explained in further detail, as these are the main focus of the studied deposits.

4.1 Virtual outcrop

The interpretation of different facies in the virtual model is mainly based on the appearance in the outcrop, which is strongly influenced by weathering characteristics. Generally, sandstone appears as beige resistant ledges or massive cliff faces (Hampson et al., 2012). Mudstone/siltstone are visible as grey, thin layers between sandstone beds or as thick beds of scree-cover in a slope (Eide et al., 2015). When beds of alternation between thin sandstone and mudstone/siltstone layers occurs, this is categorized as heterolithic deposits. Coal seams appears as black or dark grey layers that are laterally extensive (Eide et al., 2015). An example of lithological interpretation of the virtual outcrop is illustrated in Figure 4.1.1. By using these characteristics, the correspondence between interpreted lithology in the virtual outcrops and the actual lithology observed in field, turn out to be very accurate.

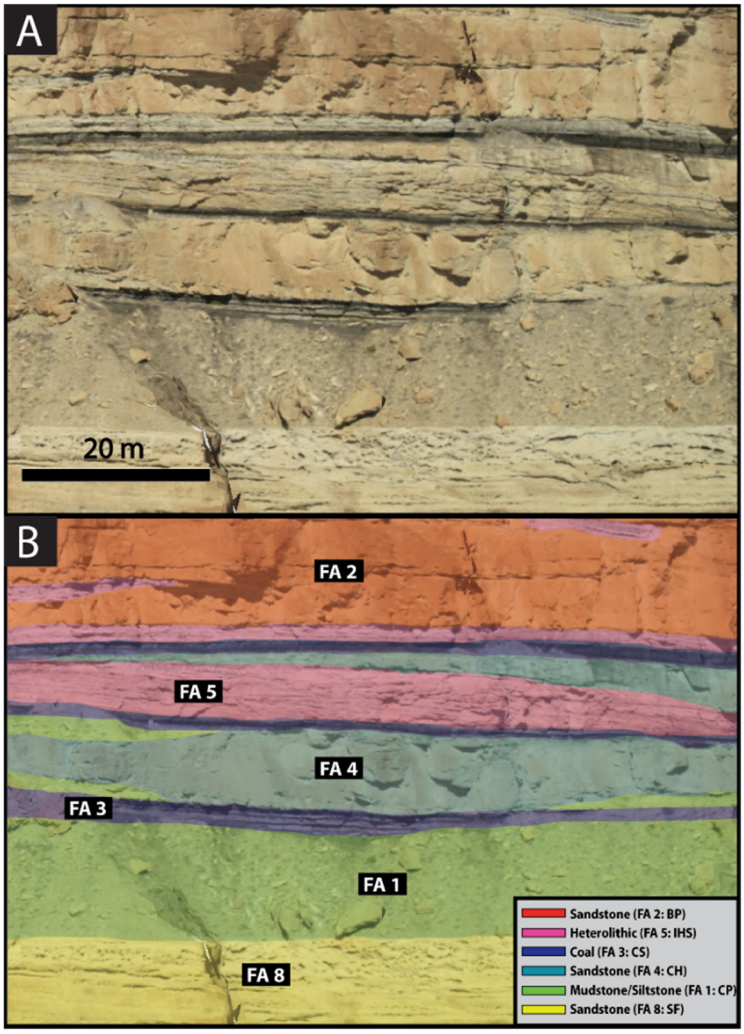

Figure 4.1.1 Illustration of a section in the Beckwith Plateau showing how the virtual outcrop is interpreted. (A) is an uninterpreted image from LiDAR-data while (B) is the corresponding interpreted image. The lithology associated with a specific facies association (FA), is marked with the same colour. Sandstone is marked as red (FA 2), light-blue (FA 4) and yellow (FA 8). Mudstone/siltstone is marked as green (FA 1). Heterolithic deposits are marked in pink (FA 5). Coal is dark-blue/purple (FA 3).

4.2 Logged sections

As the grain size and small-scale sedimentary structures cannot be observed directly in the virtual outcrops, sedimentary logs acquired in the field are included as a dataset to describe the facies of the scanned sections. In addition, observations and established interpretations from earlier studies are used (e.g. Hampson & Howell, 2005; Kamola & Van Wagoner, 1995; Van Wagoner, 1991; 1995; Yoshida, 2000; Young, 1955). One log, acquired in this study, and three other relevant logs, acquired by Eide (pers. comm.), are used as a supplementary dataset. The purpose of the logs is to (1) provide detailed information about the lithology, which is useful when assigning the input properties to the synthetic seismic model, and (2)

verify the interpretations from the virtual outcrop models. The log acquired in this study is from accessible exposures in the Woodside Canyon, behind the vertical cliffs in the north-end of the Beckwith Plateau (Figure 1.2.1). The vertical length of the acquired log is 43 m while the other three logs have a total length of 110 m, and are all mainly from the non-marine part of the Blackhawk Fm. The rest of the shallow-marine members in the Blackhawk Fm. has been thoroughly logged in several other studies (e.g. Eide et al., 2014; 2015; Hampson & Storms, 2003; Pattison, 1995).

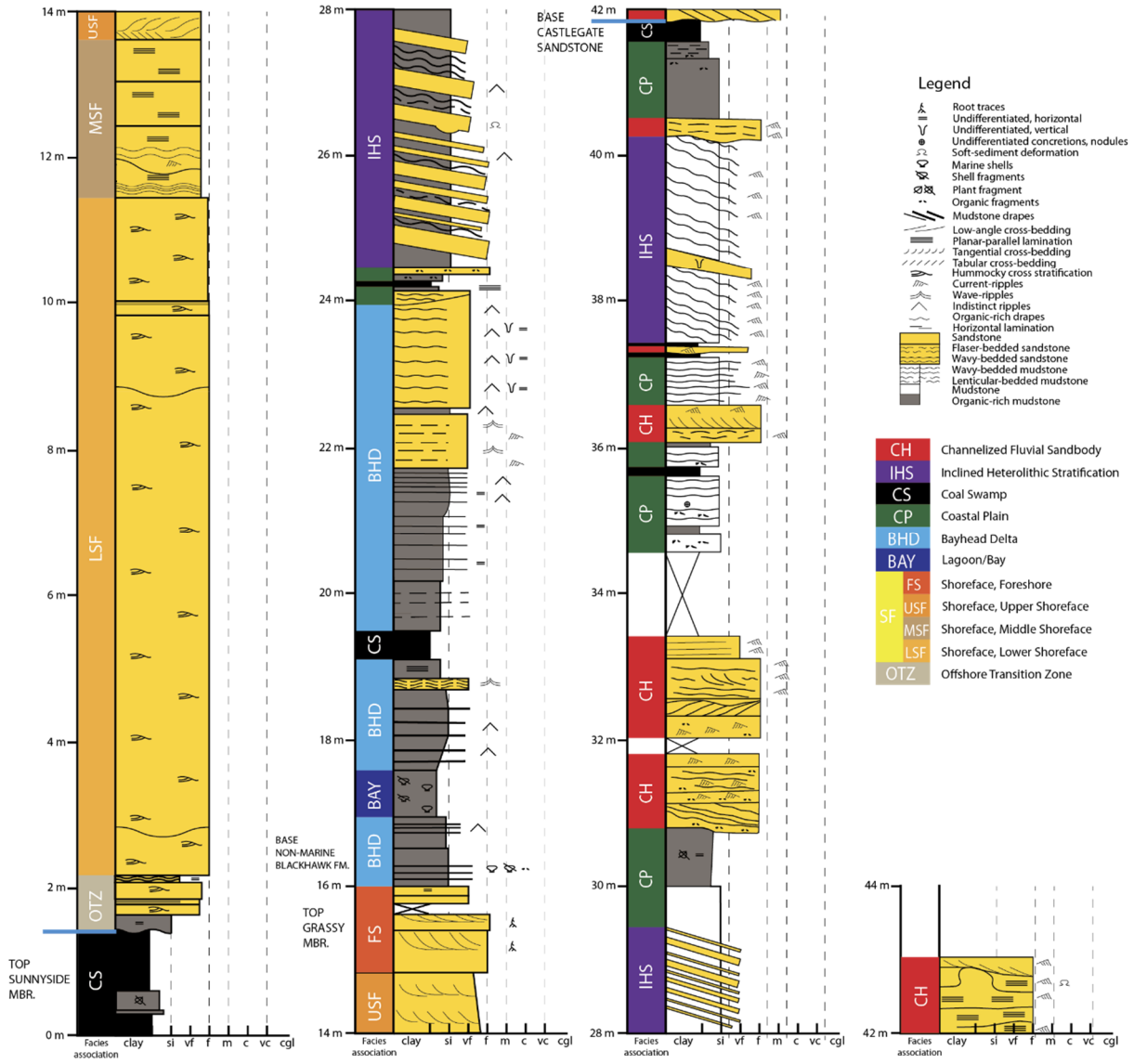

Figure 4.2.1 Stratigraphic log illustrating facies and facies association in the studied intervals. The log is acquired from an outcrop in the Woodside Canyon. The section is from the upper part of the Blackhawk Fm. (Sunnyside Mbr., Grassy Mbr. and non-marine Blackhawk Fm.) and the lower Castlegate Sandstone, showing a 43 m thick interval.

4.3 Facies assosiations

Due to a higher detail-level in the logged outcrop compared to the virtual outcrop, the number of facies and facies associations (FA) defined in the virtual outcrops and the logs differ. In the logged section 11 FAs were identified, while only 8 FAs have been recognised in the virtual outcrop. This is mainly because the degree of exposure is lower in the more mud-rich non-marine facies associations, and these are therefore more difficult to differentiate in virtual outcrop data. Muddy non-marine deposits are divided into Lagoon/Bay (BAY), Bayhead delta (BHD), and Coastal Plain (CP) deposits in the logged section, while these are all defined as Coastal Plain (CP) in the virtual outcrop. Each facies association is described in detail in Table 2, and the relationship between facies associations in logs and virtual outcrops are shown in Table 3.

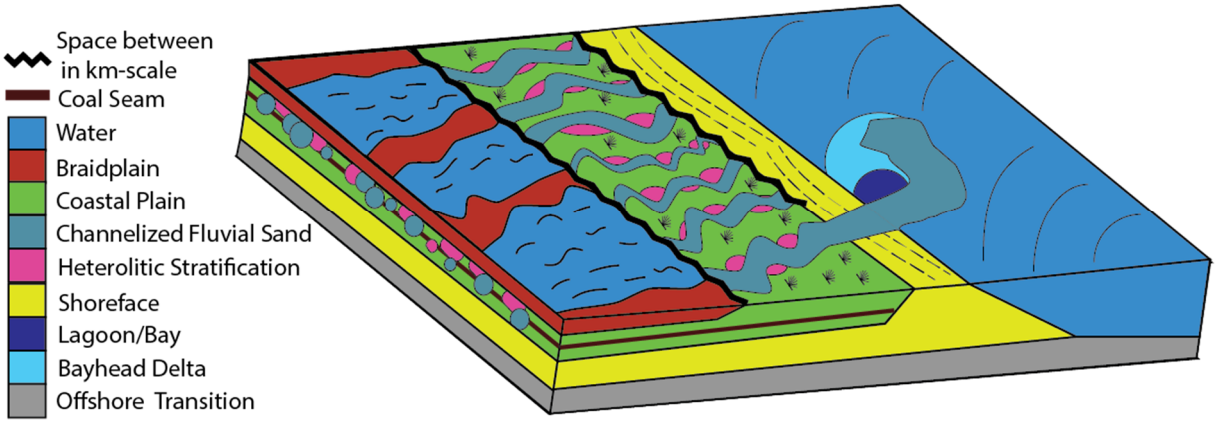

Figure 4.3.1 Illustration how a depositional system of all the studied facies associations might look like. Elements are not to scale.

Table 2 Facies association table for logged section and virtual outcrop.

Facies Association	Lithology and sedimentary structures	Appearance in virtual outcrop	Process interpretation	Observed dimensions
FA 1: Coastal Plain (CP)	Laminated mudstone beds that varies in organic content; thin (1-15 cm) sandstone beds (varying between wavy and planar) dominated by current ripples; < 20 cm thick coal beds, but no overlain roots.	Scree-covered slope of grey mudstone; thin (< 1 m) lateral extensive coal beds; infrequent beige resistant sandstone beds.	Laminated carbonaceous mudstone indicates a quiet dysaerobic environment. Occasional sandstone beds dominated by current ripples indicates events of crevasse splays or overbank deposit. Coal beds could be *ex situ* since roots are lacking.	
FA 2: Braidplain (BP)	Thick cross-stratified fine standstone; some thin (<2 m) interbedded heterolithic layers; erosional bases.	Vertical cliff; sheets of amalgamated sandstone; some heterolithic layers between; large-scale trough cross-bedding is visible.	Interpreted as deposits of braided channels or low sinuosity streams (Van de Graaff, 1972), composed of braid bars from multistory and multilateral channel complexes.	
FA 3: Coal Swamp (CS)	Lateral extensive coal seams with cleats and plant fragments (< 2m thick).	0.5 – 3.5 m thick lateral continuous black coal bed. Apparent discontinuities are due to scree-cover and/or erosion.	Interpreted as deposits of large ombrotrophic raised mire (Davies et al., 2005; Davies et al., 2006), which is a rain-fed type of peatland that typically occurs in flood plains of mature river systems.	Thickness: 0.5 – 3.5 m
FA 4: Channelized Fluvial Sandbody (CH)	Truncating sandbodies in underlaying strata; some organic fragments;	Wide semi-elliptical sandbodies that varies in symmetry; eroding	Interpreted as fluvial systems transecting a low-gradient landscape of a	Beckwith Plateau Width: 47 m – 367 m Thickness: 3 m – 8 m

	tangential and tabular cross-bedding; current ripples; < 2 cm thick discontinuous mud drapes.	surfaces; varies in mud-content; possible to see lateral accretion surfaces in muddier sandbodies; single-story, multistory and multilateral sandbodies.	coastal plain (Flores et al., 1984). Dominating fluvial system is interpreted as isolated meander-belt deposits of transgressive and highstand systems tract (Adams & Bhattacharya, 2005)	<u>Wasatch Plateau</u> Width: 28 m – 657 m Thickness: 5 m – 26 m
FA 5: Inclined Heterolithic Stratification (IHS)	Low angled (0° - 20°) sand beds interbedded in mudstone; sand beds vary in thickness (mm-scale – 20 cm) and curvature between wavy and parallel; current-ripples.	Visable interbedding between grey mudstone and beige sandstone. Often appears close to sandy CH. Also appears as isolated beds in CP and BP.	Interpreted to be deposition on point bars that lateral accreted from channel margins (Hampson et al., 2012). This can indicate that the channel was sinuous, meandering and varied in flow velocity (Hampson, 2010).	Width: < 235 m Thickness: < 11 m
FA 6: Lagoon/Bay (BAY)	Organic-rich mud; shells and shell-fragments	Undifferentiated as CP	Quiet shallow marine environment. Little influence of sediment flux due to lack of sand.	
FA 7: Bayhead Delta (BHD)	Organic-rich mud and shale; horizontal interbedded sand beds (<10cm); coarsening-upwards trend; simple horizontal burrows; small scale ripples.	Undifferentiated as CP	Interpreted as a bayhead delta downdipping into a lagoon/bay (Yoshida, 2000). Quiet environment, due to absence of wave reworking.	
FA 8: Shoreface (SF) ***Lower Shoreface (LSF)*** ***Middle Shoreface (MSF)*** ***Upper Shoreface (USF)*** ***Foreshore (FS)***	Homogenous amalgamated sandstone; *LSF:* hummocky cross-stratification (HCS); *MSF:* Planar-parallel lamination (PPL)	Homogenous, beige, resistant and almost vertical cliffs. Internal facies (LSF, MSF, USF, FS) cannot be identified in the virtual outcrop.	Interpreted as wave-dominated delta shoreline (Hampson & Howell, 2005; Young, 1955) A combination of river avulsion and efficient longshore drift that	

	USF: trough cross-stratification (TCS) *FS: Roots; TCS*		redistributed sediments by wave processes, resulted in a linear shoreline and well sorted sediments (Hampson & Howell, 2005)	
FA 9: Offshore Transition Zone (OTZ)	Fine grained sandstone with interbedded siltstone/mudstone layers; Sandstone: upwards coarsening; HCS Siltstone: horizontal burrows, PPL	Horizonal alternating layers of beige resistant sandstone and more eroded grey siltstone/mudstone; below thicker sandstone beds (SF)	Sand deposited during storm-events, while mud and stilt are fair-weather deposits (Elliott, 1986).	
FA 10: Offshore (OS)	Not logged	Scree-covered slope of dark-grey mudstone.	Interpreted to been deposited from suspension in an open marine environment, but in shallow water (Young, 1955). Deposits are known as Mancos Shale.	

Table 3 Facies associations that are recognized in virtual outcrops compared to acquired logs.

FAs recognized in virtual outcrops	**FAs recognized in logs**
Coastal plain	Lagoon/bay Bayhead delta Coastal plain
Shoreface	Foreshore Upper shoreface Middle shoreface Lower shoreface
Offshore transition zone	Offshore transition zone
Offshore	Not logged

4.4 Fluvial channel deposits

As the focus of the studied deposits is the fluvial channels both in the outcrop of the non-marine Blackhawk Fm. in the Book Cliffs and in the Snadd and Kobbe formations in the Barents Sea, a few concepts related to fluvial deposits and fluvial reservoirs must be explained. Fluvial reservoir deposits are classified according to two criteria; (a) geometry and origin of the depositional system and (b) geometry of the reservoir bodies (Miall, 1996).

The first criterion, geometry and origin of depositional systems, are divided into two broad styles; the clastic wedge (Figure 4.4.1a-b) and the paleovally fill (Figure 4.4.1c) (Miall, 1996). Major clastic wedges occur when steep paleoslopes and significant reliefs of the longitudinal profile from the hinterland towards the foreland are maintained over time through continuous tectonics (Miall, 1996). The wedges are therefore associated with rift basins and foreland basins, where uplifted mountains are the source areas. The sediments in the wedge are deposited downslope into a major delta or a strandplain system, which is the geological setting of the deposition in both the Blackhawk Fm. (Figure 4.4.1a) and the Snadd and Kobbe formations (Figure 4.4.1b). The geometry and distribution of the fluvial deposits depend on the base-level.

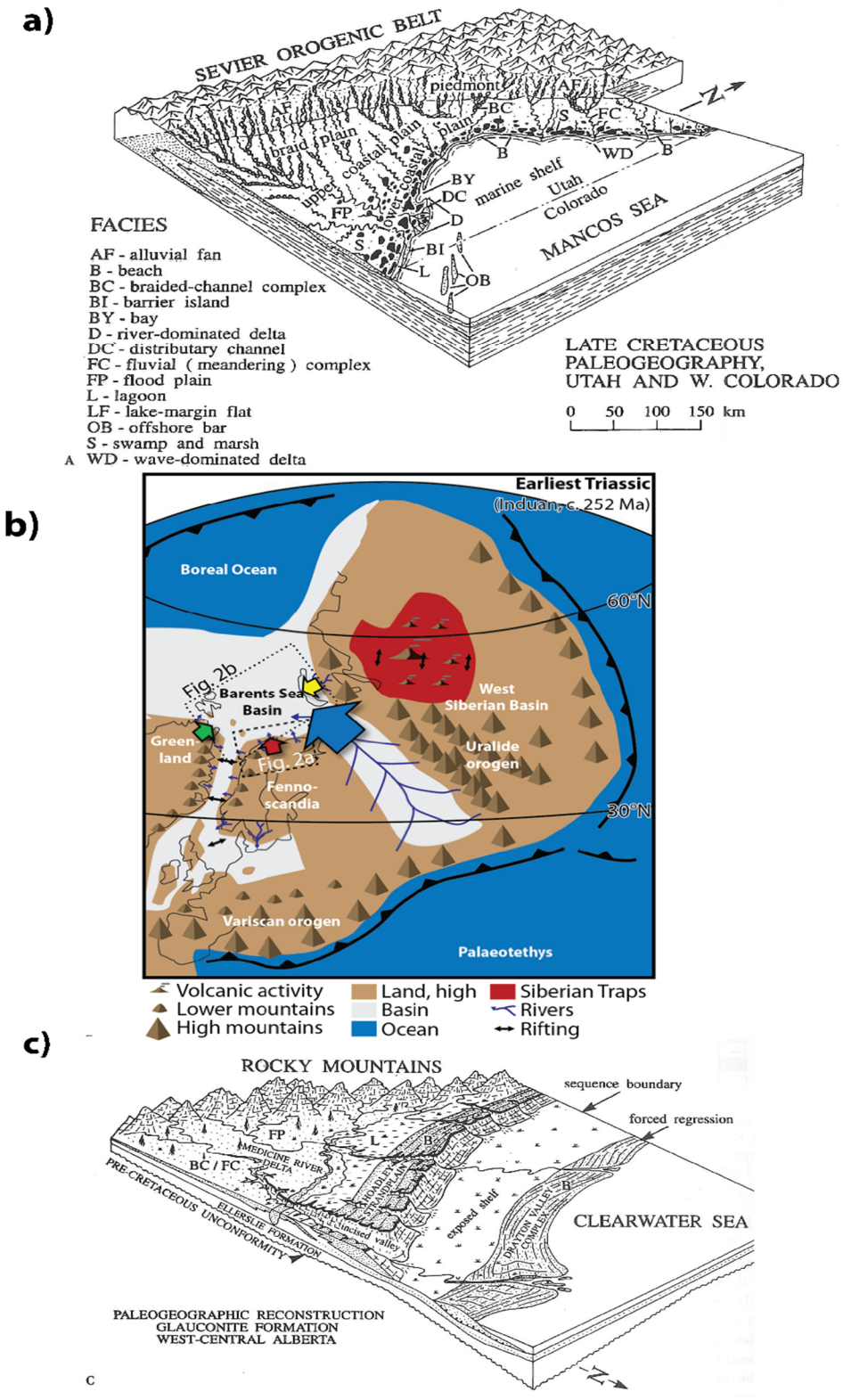

Figure 4.4.1 Illustrations of different styles of fluvial depositional systems. (a) and (b) show clastic wedge systems where uplifted mountains feed deltas in (a) Utah-Colorado (Cole & Friberg, 1989) and in (b) the Barents Sea (Eide et al., 2017a). (c) Shows a typical paleovally system from west-central Alberta (Rosenthal, 1988), where valleys are formed by subaerial channel incision during falling base-level. The valleys may be entirely or partly filled with fluvial deposits.

The second criterion to classify fluvial reservoir deposits, is the geometry of the fluvial sandbody. Gibling (2006) suggest that channel bodies in cross-sectional view can be divided into either single-story bodies (Figure 4.4.2a) or multistory bodies (Figure 4.4.2b). Single-story channel sandstone bodies are composed by single, sharp-based, fining-upwards sandbodies (Friend et al., 1979). Multistory is the term when sandbodies are composed by several stories that are arranged both vertical and lateral to each other (Gibling, 2006). Another classification by Friend (1983); Friend et al. (1979), suggested that fluvial sandbody geometry can be divided into two types; lateral extensive sheets (Figure 4.4.2c) and more lateral restricted ribbons and lenses (Figure 4.4.2d).

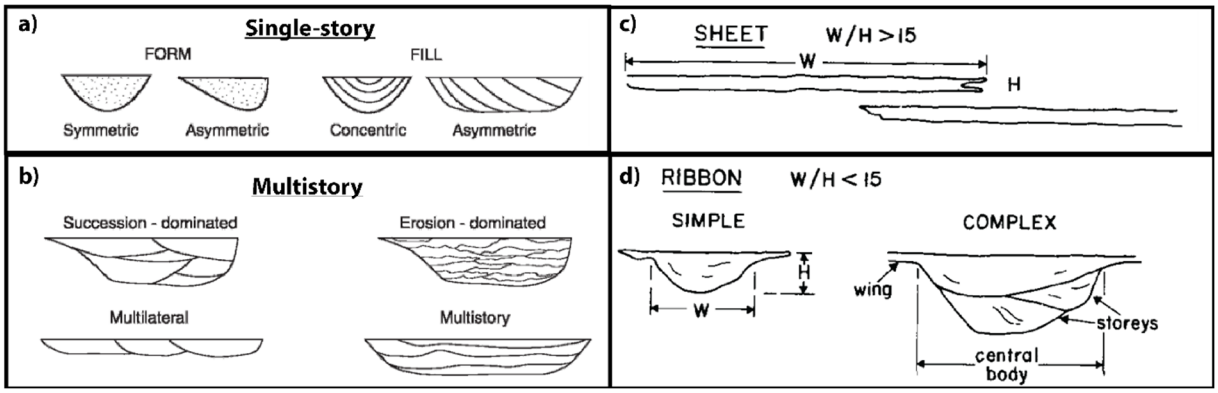

Figure 4.4.2 Two ways to characterize fluvial sandbodies. (a) and (b) are the characterization by Gibling (2006), suggesting that sandbodies are either (a) single-stories or composed by several stories, both laterally and vertically, as (b) multistories. (c) and (d) are the two types Friend (1983); Friend et al. (1979) suggest fluvial sandbody geometries can be divided into. (c) is laterally extensive sheet-deposit, typically accumulated by braided rivers. (d) show two types of isolated channel deposits, where the simple ribbon is only a single story and the complex ribbon is composed by several channel stories.

Sheet sandstone are commonly formed by bed-load systems, like braided rivers, that frequently migrate across a broad area of plain-floor with a steep gradient. Ribbon and lenses of sandstone are accumulated within channel systems that are isolated by fine-grained overbank deposits. Friend et al. (1979) also proposed that the fixed channels that deposits ribbon bodies do not have a greater width/depth ratio than 15, while sheets and more mobile channel belts have a ratio greater than 15. The ribbons can either be simple (single-story *sensu* Gibling (2006)) or complex (multistory *sensu* Gibling (2006)). Point bars are the best known type of such ribbon-shaped sandbodies (Miall, 1996).

Point bars develop on the inside bend of meandering channels, where they accrete laterally as the mender bend migrates downstream and transverse to the flow direction (Allen, 1964). The lateral-accretion deposits in a point bar develop as the main flow of a channel is directed away from the outer bank and towards the inner bend (Figure 4.4.3). The surface flow builds up a higher water level and pressure against the outer bank and erodes actively (Miall, 1996). The return flow is overturned and moves towards the inner bank along the bed, increasing the friction between the flow and the bed. Towards the inner bank, this results in reduced flow velocity, bed shear stress, stream power, flow depth and increased sedimentation of suspended fine-material (Jackson, 1976). As the meanders evolve by lateral growth and corresponding large-scale, gently dipping accretion surfaces, deposits termed point bars are developed (McGowen & Garner, 1970).

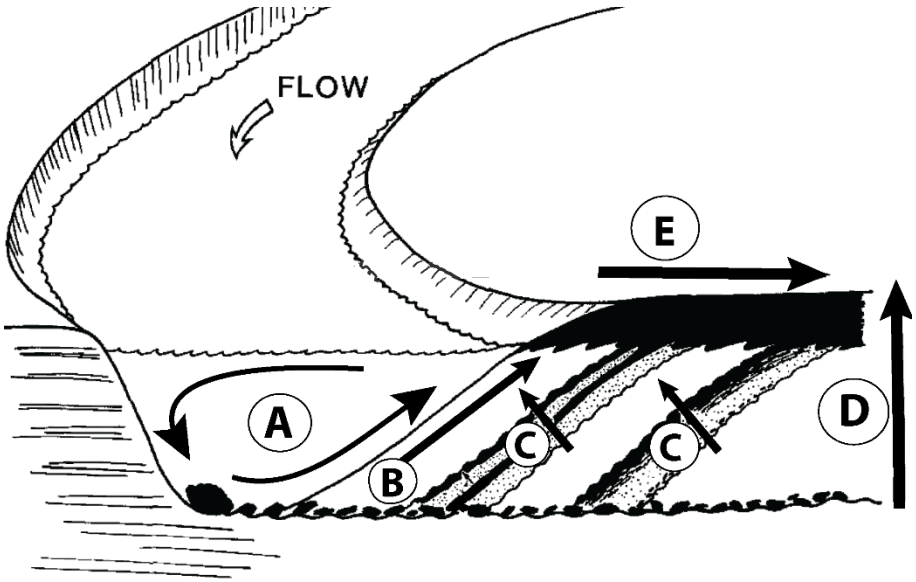

Figure 4.4.3 Illustration of lateral accretion deposition in a meander bend. (A) shows how the surface flow is overturned in the outer bank and directed towards the inner bank along the channel bed. (B) illustrates an up-dip fining within the inclined units. (C) show a fining perpendicular to the inclined lateral accretion surfaces within the inclined units. (D) symbolizes an overall vertical upward fining of point bars. (E) illustrates a lateral fining away from the channel and into the overbank. Modified from Thomas et al. (1987).

The internal geometry and lithofacies of lateral accretion deposits are very variable, depending on e.g. channel geometry and sediment load. In this study, there are two facies associations linked to fluvial deposits; channelized fluvial sandbody (FA 4) and inclined heterolithic stratification (FA 5). The channelized fluvial sandbody (CH) is composed by dominantly fine cross-stratified sandstone, whereas the inclined heterolithic stratification

(IHS) is composed by alternations of parallel, dipping fine-grained sandstone beds and mudstone/siltstone beds (Figure 4.4.4). The IHS deposits represent an episodic growth of a point bar, where fines are deposited in the inner bank during periods of lower energy level in the channel and sand during higher energy level (Thomas et al., 1987). When the paleocurrent direction is known and dip directions of the IHS are exposed in a cross-cut of the outcrop, these two factors can be used to determine where in the meander bend the cross-cut is from (Ghinassi et al., 2014).

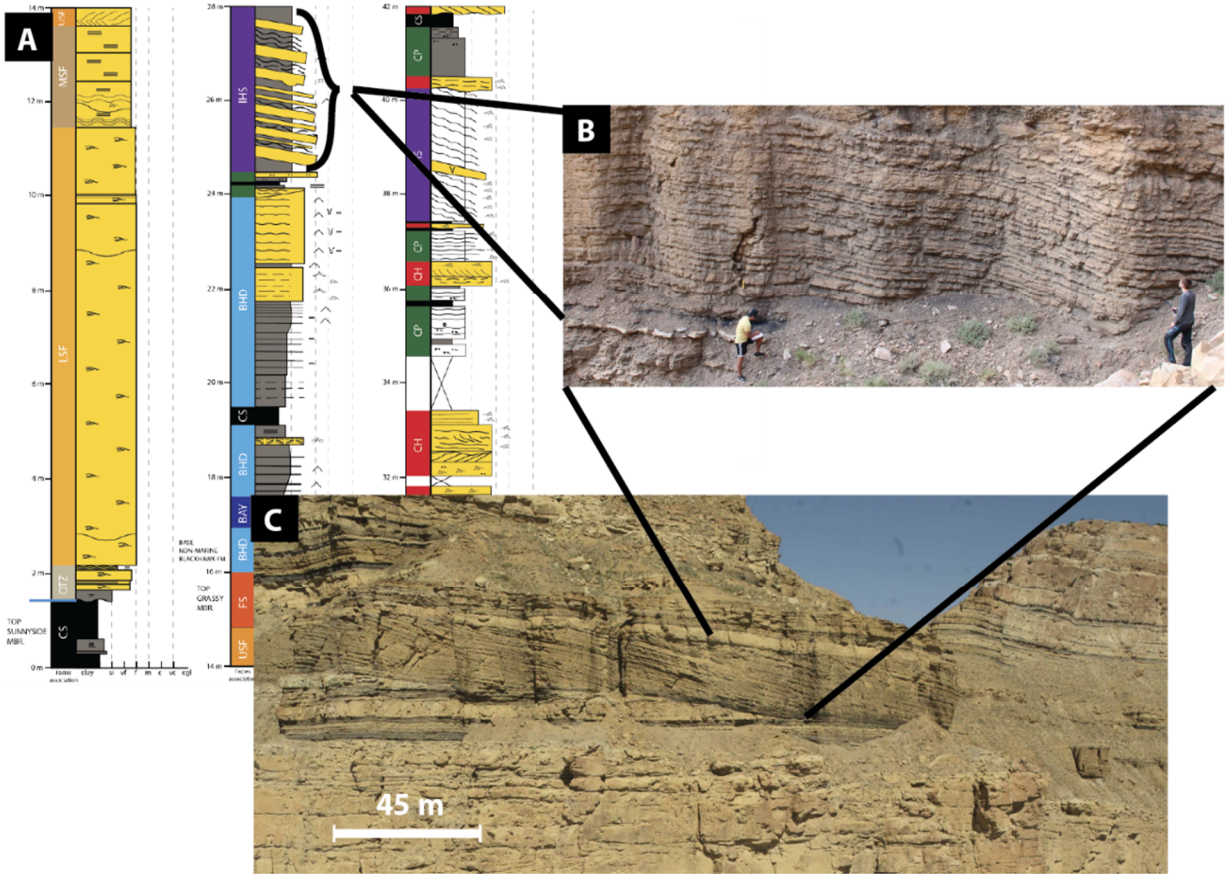

Figure 4.4.4 Illustration of how IHS deposits appear in logs and in the field. (B) shows how the logged IHS (A) from Figure 4.2.1 looks like in an outcrop (humans for scale). (C) shows how such deposits appear from a distance in a large-scale outcrop. (A) and (B) are taken from an outcrop in Woodside Canyon, while (C) is from further south in the Beckwith Plateau. However, none of these are from the exact same area.

5 RESULTS

In this section, the results from the synthetic seismic modelling will be presented, where three different aspects of the modelling will be highlighted. First, the geological interpretation of the outcrop from the Beckwith Plateau will be presented (5.1). Then, the resulting synthetic seismic images of the outcrop, using different frequencies, are presented (5.2). Thereafter, a reduced detail-level in the geological input model will be tested to see how this affects the seismic (5.3). Finally, synthetic seismic using 1D convolution is presented and compared to 2D convolution (5.4).

5.1 Interpretation of northern Beckwith Plateau

The interpretation of the outcrop in the northern part of the Beckwith Plateau is done with focus on the non-marine part of the Blackhawk Fm. As the purpose is to get a lithological interpretation to use as an input for the synthetic seismic modelling, the focus is to map only lithological changes for elements that are larger than 1 m. This is because the seismic resolution would be out of scope for this thesis, as features this small would be below seismic resolution (e.g. Lebedeva-Ivanova et al., 2018). The exception is for bodies of inclined heterolithic stratigraphy, where details are mapped down to 14 cm as the seismic effect of such small-scaled details in fluvial deposits will be tested in this study. Previous studies have established the large-scale lithology and parasequences within the Book Cliffs and Beckwith Plateau (Davies et al., 2006; Eide et al., 2014; 2015; Rittersbacher et al., 2014a; Yoshida, 2000; Young, 1955), and these are used as guidelines when interpreting the virtual outcrop. As heterogeneities in the coastal plain deposits are mostly undifferentiated in previous studies, these interpretations are mainly based on observations in field and in the virtual outcrop.

5.1.1 Lithological interpretation

When looking at the outcrop from distance (Figure 5.1.1), four lateral continuous beige resistant ledges and cliffs stands out. One additional similar ledge stands out, but this is not lateral continuous as it abruptly stops after the first kilometre towards SSW. By using the virtual outcrop interpretation characteristics described in 4.1, are all the beige resistant ledges in the outcrop interpreted as sandstone ledges. Three of these sandstone ledges have a prominent, laterally continuous white zone in the upper part, interpreted as a result of bleaching of iron carbonates (Van de Graaff, 1972). When zooming in to the thickest beige sandstone cliff at the top of the outcrop, is differs from the others by having a much more chaotic internal bedding with discontinuous mud draped surfaces dipping in several directions. The scree-dominated interval below also contains sandstone in form of stacked lensoidal sandstone bodies that are smaller and more constrained, ranging up to 270 m wide and 14 m thick. These lenticular bodies also have visible internal bedding, with more parallel dipping mud draped surfaces. Close to the bottom of the outcrop, an additional thin (< 6 m) sandstone ledge appears. This ledge starts in the last third of the outcrop towards SSW, and is lateral continuous further south outside of the study area.

From distance, three thick (< 60 m) intervals dominated by scree-cover are identifiable. One additional thin (< 25 m) interval can be identified at the lowermost part of the outcrop. According to 4.1, these scree-covered intervals are interpreted to be mudstone/siltstone dominated. When the two upper scree-covered intervals are studied on a kilometre-scale, they consist of three additional lithologies; lensoidal sandbodies, bodies of thin (< 20 cm) alternating dipping layers and thicker (< 3.5 m) lateral extensive black to dark grey layers. The thin alternating layers are interpreted to be heterolitic deposits, while the extensive dark layers are interpreted to be coal seams. Lateral extensive heterolithic deposits, that are not dipping, are also identified in the lower scree-covered intervals.

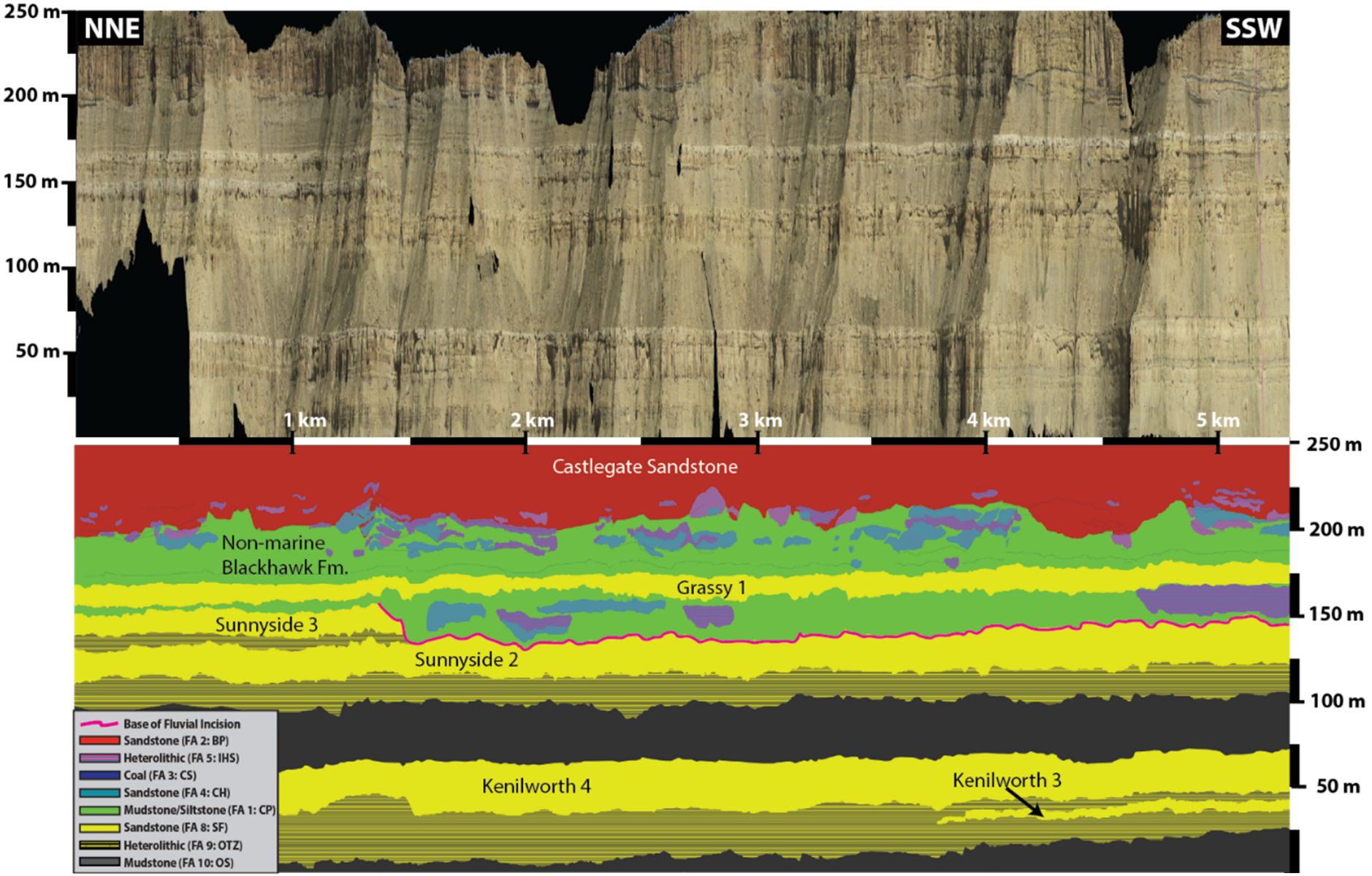

Figure 5.1.1 Panel-view of northern part of Beckwith Plateau in the upper picture and the resulting interpreted image with members and formation below. Both images are in the same scale and are shown with a 6,5x vertical exaggeration. As the panel-view is zoomed-out, all the interpreted details might not be visible in this image.

5.1.2 Facies associations and formations

By using the logged sections and facies association table in Table 2, it is possible to interpret and connect the observations and lithology to a specific facies association. This can be further linked to members of the Blackhawk Fm. The sandstone lithology is interpreted to three different facies associations; braidplain (BP), channelized fluvial sandbody (CH) and shoreface (SF) (Table 2). The uppermost thick sandstone bed with chaotic internal bedding is interpreted as a braidplain (facies association BP), where the deposits are composed by several braid bars in a multistory and multilateral channel complex. This is known as the Castlegate Sandstone, where the lower boundary separates it from the Blackhawk Fm. (Spieker & Reeside Jr., 1925). The lenticular-shaped sandstone bodies in the two upper mudstone/siltstone dominated intervals are interpreted to be channelized fluvial sandbodies (facies association CH), where the dipping internal structure represent lateral accretion surfaces. These intervals represent the non-marine Blackhawk Fm. The rest of the homogenous sandstone ledges are interpreted as shoreface (facies association SF) deposits. Each of the SF intervals represent a specific parasequence/member of the Blackhawk Fm. The thin sandstone ledge that only appears in the SSW-end, represents the end-point of the SF deposits to the Kenilworth 3 member. The four SFs above this represent the following parasequences moving upwards in the outcrop; Kenliworth 4, Sunnyside 2, Sunnyside 3, Grassy 1 (Figure 5.1.1) (Eide et al., 2015).

The thick mudstone/siltstone dominated intervals are linked to two main facies associations; coastal plain (facies association CP) and offshore (facies association OS). The two upper scree-covered intervals, containing bodies of CHs, heterolithic deposits and extensive coal seams, are interpreted as CP deposits in the non-marine Blackhawk Fm. The lower CP is interpreted to be a result of subaerial filling of an incision, as it is deposited next to the cut-off SF deposit of Sunnyside 3 (Howell & Flint, 2003a). The two lower mudstone/siltstone intervals are of OS origin, where all OS deposits in the Book Cliffs are named Mancos Shale (Young, 1955). As for the heterolithic deposits, these are divided into two facies associations; inclined heterolithic stratification (IHS) and offshore transition zone (OTZ). These are distinguished by the differences in lateral extension, apparent dip and surrounding depositional environment. The interpreted thin lateral extensive coal seams (CS) are all within the interpreted terrestrial depositional environment.

As the deposits in the Book Cliffs are not significantly affected by tectonics after sedimentation, interpreting lateral extensive facies associations are rather uncomplicated. Interpreting facies within muddy deposits (such as coastal plain deposits) on the other hand, is a challenge due to the coverage of scree. For this reason, several CHs may not be mapped, as their sandbodies are not visible in the virtual outcrop. The mapped CHs have large variation in size. However, since individual CHs within multistory sandbodies are not interpreted in this study, it is difficult to make a detailed comparison of the ancient channel widths and depths.

For interpretation of IHS, there are a lot of variation in terms of dip directions. As interpreting the accurate dip direction for all IHS is both time-consuming and challenging, an average dip direction is assigned for most of the mapped IHS deposits. The majority of the interpreted IHS deposits have an apparent horizontal dip, where a possible dip direction can be either away from- or towards the outcrop face. The thickness of the alternating beds in the IHS are also generalized. In reality, the thickness of the alternating sandstone and siltstone beds within a IHS deposit varies much (Figure 4.4.4), but in this model the beds are set to a constant thickness of 14 cm, which is a realistic thickness according to the acquired logs.

The results after mapping the whole outcrop by the characteristics described in 4.1 and connecting them to the described facies associations in Table 2, show some general observations (Figure 5.1.2a-f):

There are two dominating marine parasequences at the bottom-half of the outcrop, Kenilworth 4 and Sunnyside 2, which are composed by offshore, offshore transition zone and shoreface deposits (Figure 5.1.2a). The upper half is dominated by non-marine deposits from both the upper Blackhawk Fm. and the Castlegate Sandstone (Figure 5.1.2b). The marine deposits of Sunnyside 3 are suddenly eroded away after 1.5 km towards SSW, where the void has been filled by non-marine deposits (Figure 5.1.2c). The Grassy 1 shoreface deposits separates this non-marine interval from the non-marine Blackhawk Fm. interval above (Figure 5.1.2d). The channel deposits are larger and more sparsely distributed in the lower interval (Figure 5.1.2e). The mapped fluvial channelized sandbodies and inclined heterolithic stratification are often linked together (Figure 5.1.2f). The boundary between the non-marine

Blackhawk Fm. and Castlegate Sandstone is sharp, but there are still channel deposits within this boundary.

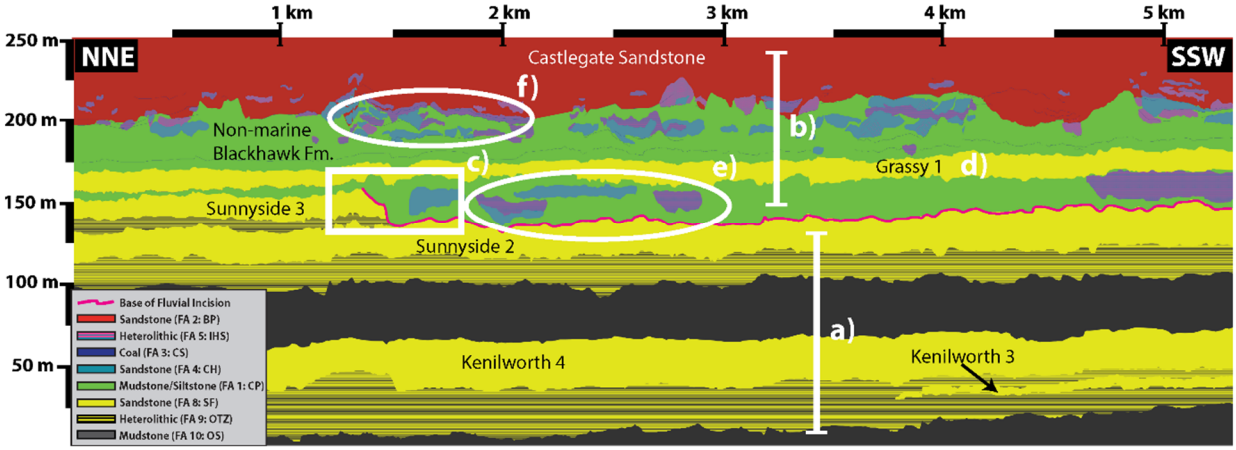

Figure 5.1.2 General observations after mapping the whole outcrop; (a) Two marine parasequences (Kenilworth 4 and Sunnyside 2) dominating the lower-half of the outcrop. (b) Non-marine deposits dominating the upper-half of the outcrop. (c) Eroded marine deposits of Sunnyside 3 that are filled with non-marine deposits. (d) Grassy 1 shoreface separating the two intervals of non-marine deposits. (e) Large and sparsely distributed channel deposits in the lower non-marine interval. (f) Smaller and densely spaced deposits of fluvial sandbodies and inclined heterolitic stratification in the sharp boundary between the Blackhawk Fm. and the Castlegate Sandstone.

5.2 Synthetic seismic at different dominant frequencies

Synthetic seismic is generated of the mapped outcrop by populating each lithology with elastic properties and defining a seismic modelling setup. The setup involves specifying what dominating frequency wavelets to use in the modelling process. The chosen frequency is fundamental to what geological features from the mapped outcrop that will be illuminated in the seismic. As there are a wide range of frequencies that can be selected, it is important that the selected frequencies reflect the aim of the study.

The dominant frequency of the wavelets in this is varied from 10 Hz – 50 Hz, which are typical frequencies used in seismic surveys with reservoir targets in the subsurface Norwegian continental shelf. 100 Hz is also tested, because modern high-resolution seismic is also becoming available. An example of this is the so-called "P-Cable"-technology, which has been used to acquire seismic data from reservoir targets in the subsurface Barents Sea with frequencies up to 250 Hz (Planke et al., 2009). The focus in this part of the study is to describe differences in synthetic data in terms of illuminated geometries and amplitudes. The chosen frequencies that will be described are: 20 Hz, 30 Hz, 50 Hz and 100 Hz.

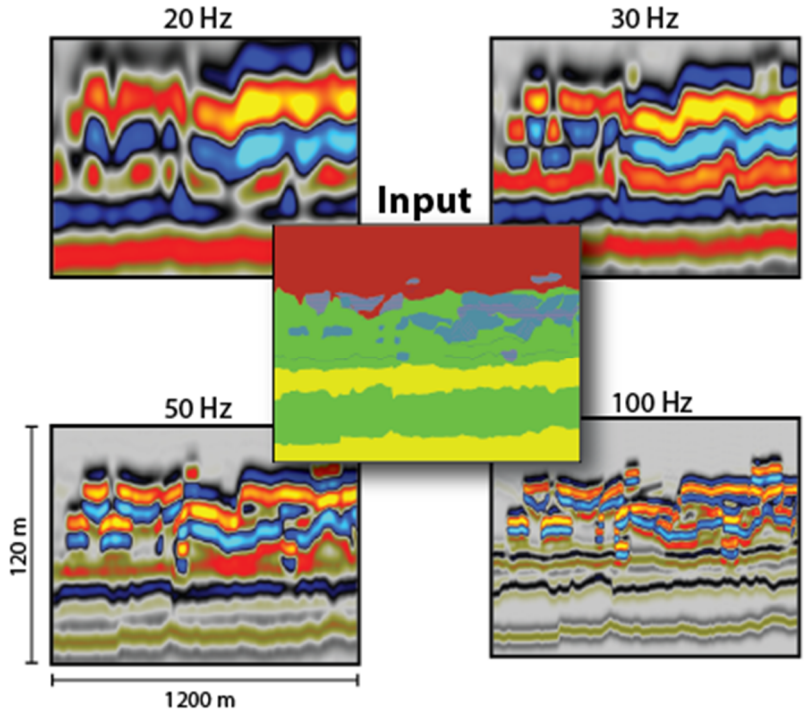

Figure 5.2.1 Illustration of how different synthetic seismic can appear when modelling the same input-model using different dominant wavelet frequencies.

5.2.1 Survey

The generated synthetic seismic for all four frequency wavelets has been interpreted by nine participants in a survey. The workflow of the survey is to interpret each seismogram on separate sheets, starting from the lowest resolution and gradually interpreting seismic with higher dominant frequency. This is because the participants should not be affected by the other seismograms when interpreting, as different resolutions reveal different details. Two types of information were provided prior to the interpretation; (1) channels in this this model often start as red amplitudes at the top and are blue amplitudes at the base and (2) there are no faults in the modelled area. This information was provided as interpreters usually have some information about the seismic data and the regional geology before they start interpreting real seismic as well. The results of the survey are used along with observations by the author to describe how the synthetic seismic changes from frequency to frequency. Two typical responses of the survey are presented in Figure 5.2.2, whereas the rest of the results from the survey are compiled and further discussed in section 6.2.

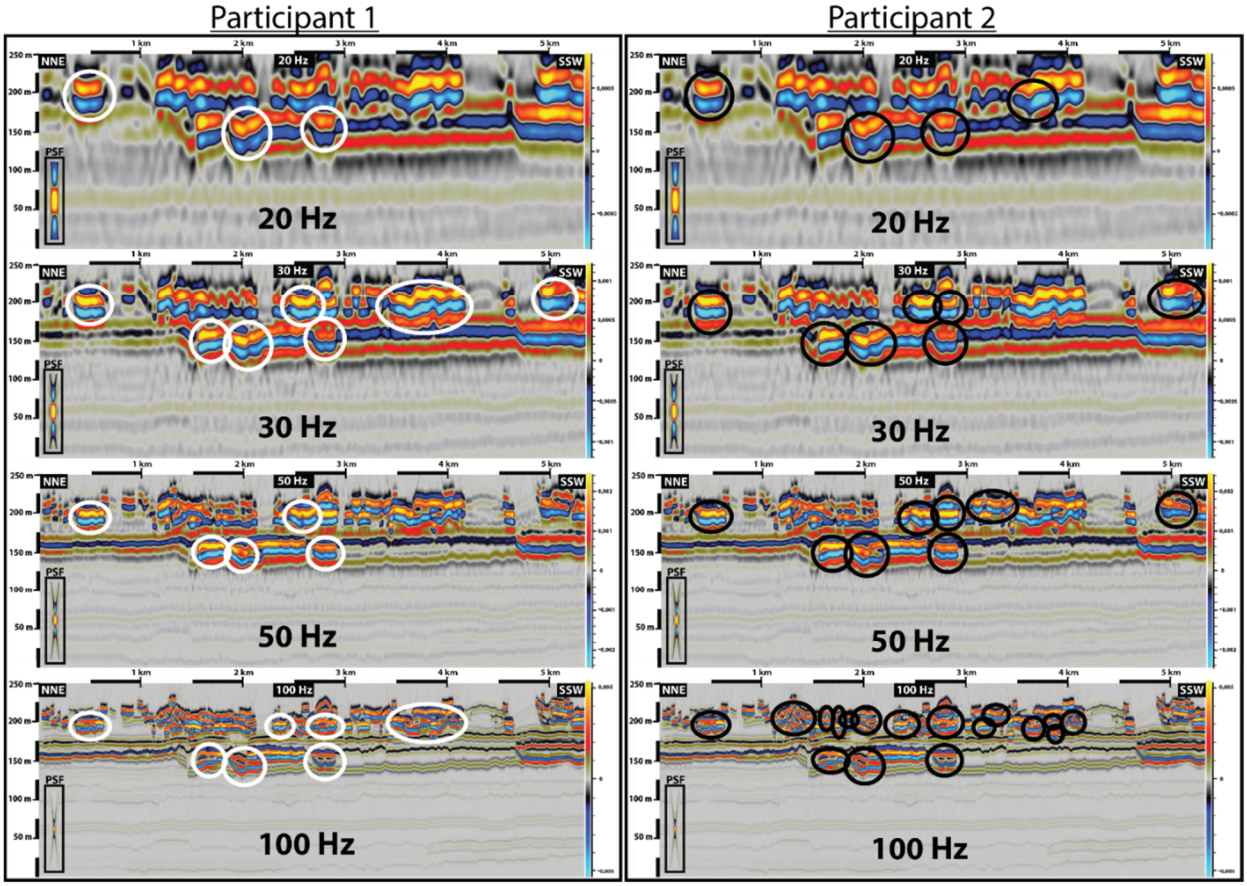

Figure 5.2.2 Typical response from two different survey participants. Ringed out areas represent the interpreted channel deposits.

5.2.2 30 Hz

First, the synthetic seismic image of the outcrop with 30 Hz frequency is presented. This is similar to typical dominant frequencies in seismic data for targets at *c.* 2 km depth (e.g. Eide et al., 2017b; Klausen et al., 2018), which is a typical depth interval for many hydrocarbon reservoirs on the Norwegian Continental Shelf. In generated synthetic image, most of the large sandstone-dominated channels (Figure 5.2.3a, b, d, g) are visible, as well as composite high-amplitude reflections in the areas with channels dominated by heterolitic deposit (Figure 5.2.3c, e, f). It is possible to see the channel body geometry of several deposits, where the most isolated deposits are easiest to tell apart as convex lenticular shapes (e.g. Figure 5.2.3f'). Seven of the large channel deposits seem to stand out in the seismic (Figure 5.2.3a-g). While where the channel deposits are located close to each other, it is more challenging to distinguish the individual bodies. In the survey, the participants have on average interpreted six channels for the 30 Hz synthetic seismic.

Channel bodies are visible as a red peak (increase in acoustic impedance) at the top and blue trough (decrease in acoustic impedance) at the base, which is same for all the frequencies. Several of the channels reach the highest values of both positive and corresponding negative amplitudes of the defined scale. The tuning thickness at 30 Hz is 30.8 m. Thicknesses of channel bodies in the seismic data, measured from the peak amplitude at the top to the trough amplitude at the base, is significantly thicker than the real thickness measured in the outcrop data. The dimensions of channel "d" in Figure 5.2.3 has been measured in all the generated synthetic seismograms, where the apparent thickness of this channel is further discussed in section 6.2.

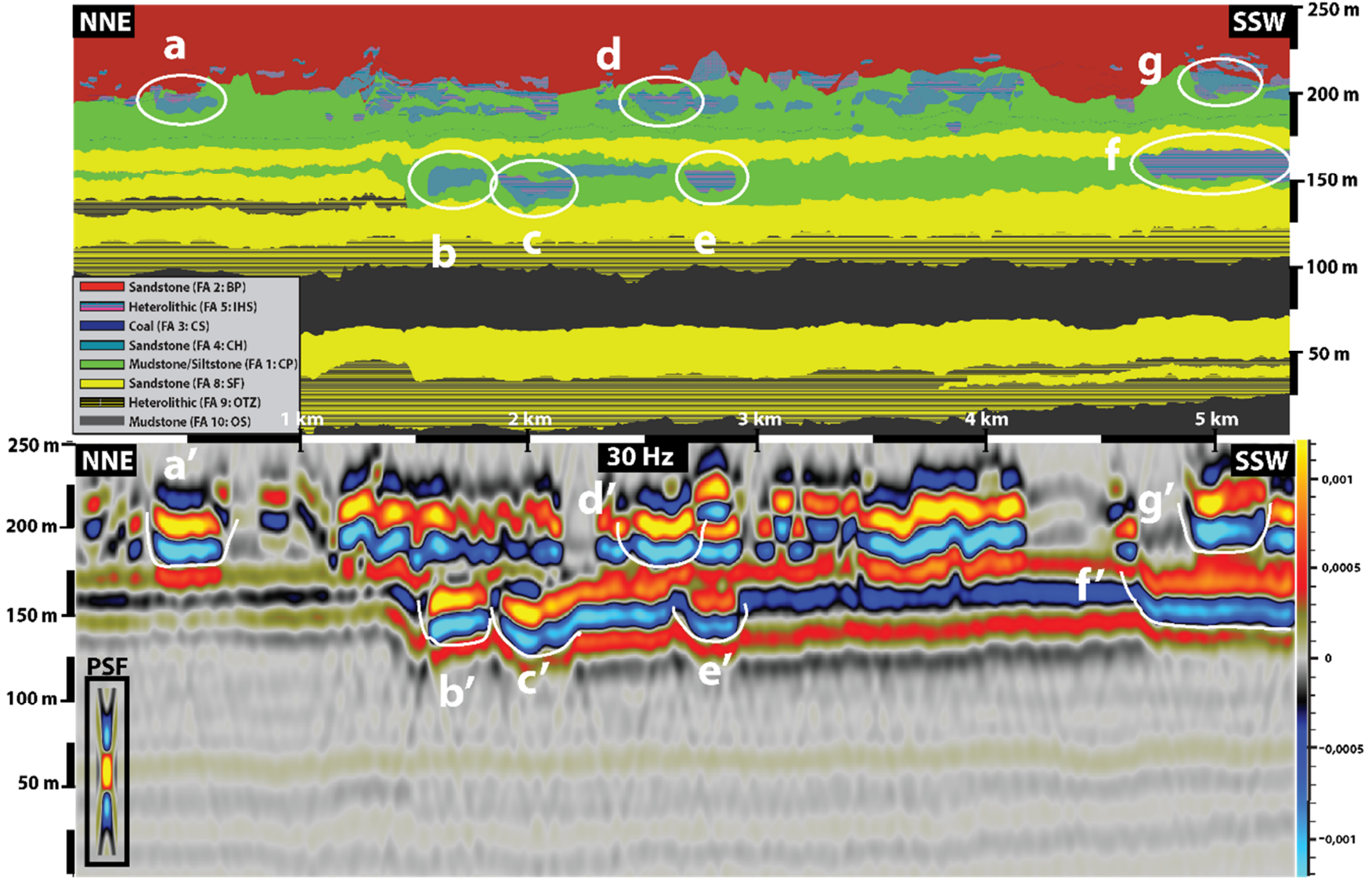

Figure 5.2.3 Comparison between the mapped input-outcrop and the resulting synthetic seismic image using 30 Hz. Focusing on fluvial channel deposits, seven of the large channels in the mapped outcrop are also identifiable as channels in the seismic: a-a', b-b', c-c', d-d', e-e', f-f' and g-g'. (For uninterpreted version of 30 Hz synthetic seismic, see Appendix Figure A.2)

5.2.3 20 Hz

The synthetic seismic image using 20 Hz, is the seismic that has largest variation of the studied frequencies when looking at a change of 10 Hz between each. A dominant frequency of 20 Hz is comparable to typical data quality at depths of *c.* 3 km on the Norwegian continental shelf (Eide et al., 2017b). Channel geometries are not illuminated as well as in 30 Hz, where the bodies do not seem as isolated anymore but rather laterally linked (e.g. Figure 5.2.4e – e'). However, the convex geometries of the largest channel deposits are still visible, where especially four seem to stand out (see a – a', c – c', d – d' and f – f' in Figure 5.2.4). The survey

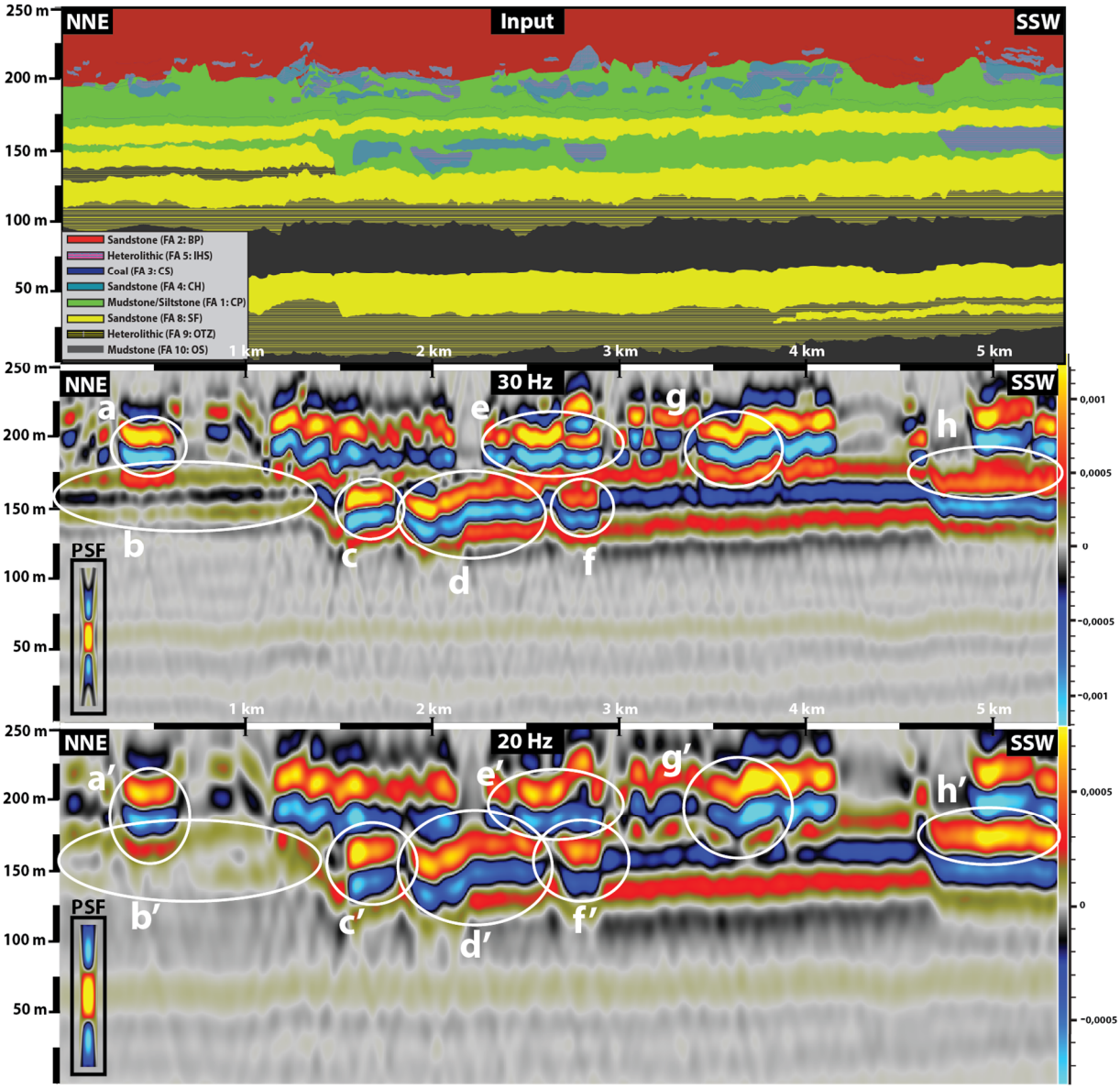

Figure 5.2.4 Comparison between synthetic seismic generated with 30 Hz and 20 Hz, focusing on different features in 20 Hz. These features are highlighted with letters in 30 Hz and corresponding marked letters in 20 Hz. (For uninterpreted version of 20 Hz synthetic seismic, see Appendix Figure A.3)

also supports this, where the participants on average were able to identify five channels within this frequency, compared to six at 30 Hz.

Two of the channel deposits even seem to have a clearer lenticular geometry in 20 Hz than in 30 Hz (a – a' and g – g' in Figure 5.2.4). The amplitude change from 30 Hz to 20 Hz is also remarkable, where only two of the channels remain with the max/-max amplitude (a – a' and g – g' in Figure 5.2.4). Some of the reflections disappear when using 20 Hz (b – b' in Figure 5.2.4), while others even seem to appear clearer than with 30 Hz (h – h' in Figure 5.2.4). This is a result of interference, which is a concept further discussed in section 6.2. As the wavelength gets longer at 20 Hz compared to 30 Hz, the apparent thickness and tuning thickness also gets thicker. The tuning thickness for fluvial deposits are now 46.1 m.

5.2.4 50 Hz

When increasing the frequency to 50 Hz, the seismic image gets more detailed. Such frequencies would be expected in shallow depths of 3D seismic datasets, and could be used to map shallow reservoirs (such as the Wisting Field reservoir or to store produced water), for site surveys to detect drilling hazards, and possibly in shallow seismic for geotechnical purposes. When comparing 30 Hz to 50 Hz, the channel geometries are illuminated at a higher detail-level and smaller channel deposits appears as distinct bodies. The area marked as "c" in Figure 5.2.5 appears as multiple inclined deposits in 30 Hz and could have been interpreted as inclined heterolithic stratification (as it was by one survey participant). However, in 50 Hz, these inclined reflections appear as separate horizontal deposits (c – c' in Figure 5.2.5). Another area appears as a continuous wiggly deposit in 30 Hz, but turns into more chaotic heterolithic deposits in 50 Hz (g – g' in Figure 5.2.5). This chaotic effect is also reflected in the 50 Hz seismic interpretation in the survey, where only one more channel is on average interpreted compared to the less detailed 30 Hz.

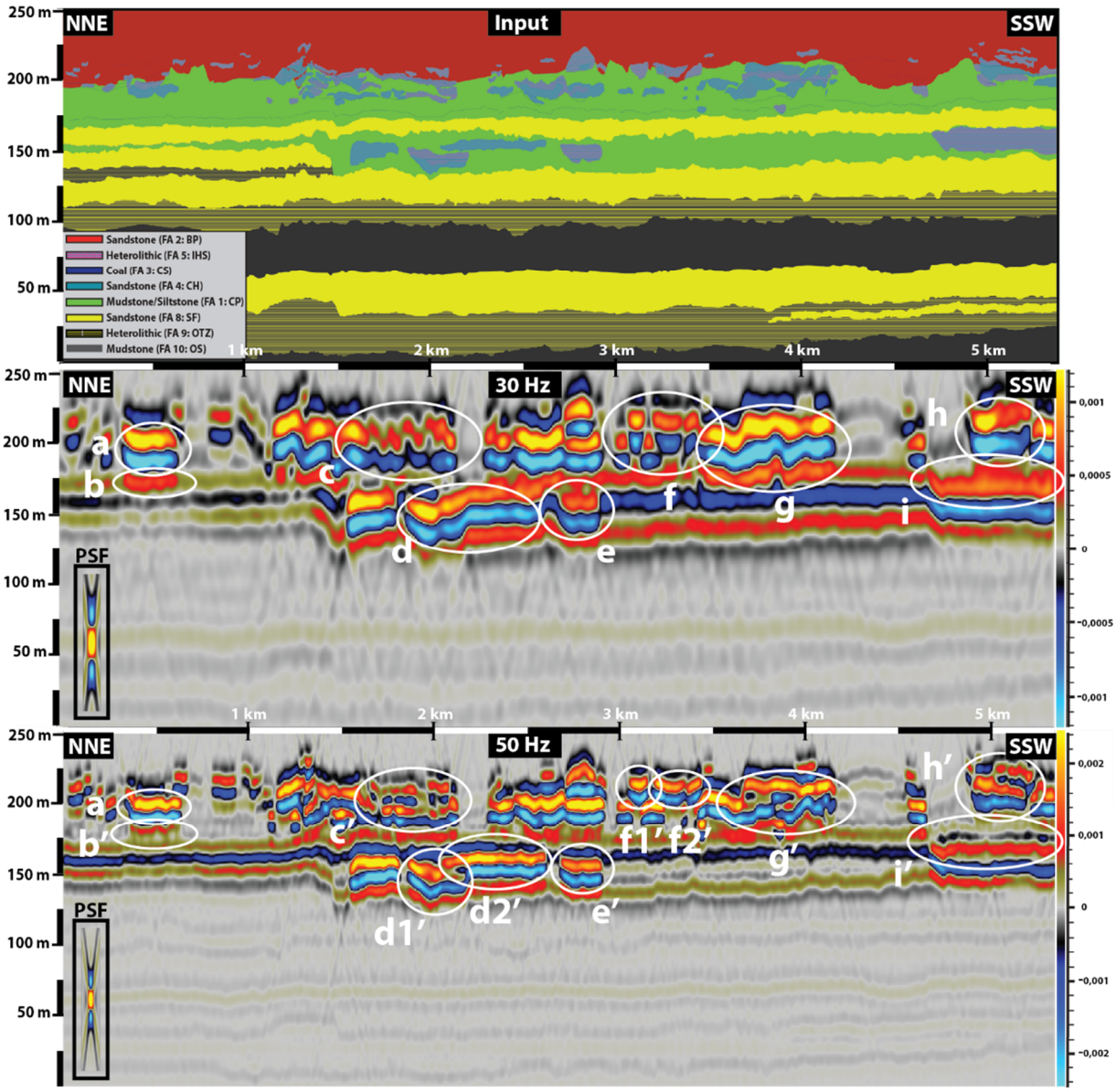

Figure 5.2.5 Comparison between synthetic seismic generated with 30 Hz and 50 Hz, focusing on different features in 50 Hz. These features are highlighted with letters in 30 Hz and corresponding marked letters in 50 Hz. (For uninterpreted version of 50 Hz synthetic seismic, see Appendix Figure A.4)

The larger channels appear much more isolated than in 30 Hz, where one of the larger channels even seem to have split into two bodies (d – d1' and d2' in Figure 5.2.5). The convex lenticular geometry also changes, where some of the larger channels seem to flatten out in 50 Hz, while some of the smaller channel get a more distinguishing lens-shape (f – f1' and f2' in Figure 5.2.5). For one of the large channels, it appears connected to a lateral extensive reflection below in 30 Hz, but then disconnects in 50 Hz (b – b' in Figure 5.2.5). The participants of the survey responded to these described effects by interpreting more of the smaller channels.

As for amplitude differences, several of the smaller channels are reaching the max/-max values that did not reach the corresponding values for 30 Hz. More and thinner seismic reflections appear in this image, which gives a more detailed view of the vertical variation where two of the larger channels goes from a thick red reflections (increase in acoustic impedance) to thin red, grey (similar acoustic impedance as above) and blue seismic reflections (decrease in acoustic impedance) (h – h' and i – i' in Figure 5.2.5). The tuning thickness for fluvial deposits is down to 18.5 m for the 50 Hz frequency.

5.2.5 100 Hz

The last frequency that is tested is 100 Hz. For many cases, this is an unrealistic and excessively high dominating frequency to be able to use in seismic acquisition of the subsurface, as such high frequency wavelets do not penetrate deeper reservoir targets. However, recent advances in acquisition technology allows seismic surveys to use high frequencies to illuminate shallow reservoirs at a high level of detail. E.g., has "P-cable"-technology acquired 3D seismic of the Wisting field in the Barents Sea at shallow targets of 250 m below seabed, where the method uses a frequency range of 50 to 250 Hz (Planke et al., 2009). Such frequencies are also common in shallow seismic used for example for site surveys to detect drilling hazards, to select targets in shallow stratigraphic drilling (e.g. Rise & Sættem, 1994) and to investigate geotechnical properties for offshore installations such as wind farms.

When comparing the generated 100 Hz seismic image of the Beckwith Plateau to the 50 Hz, many more details are resolved even though the trends are very similar. The channel base geometry for the larger channels are now much more curved than with 50 Hz (b – b', c – c' and d – d' in Figure 5.2.6), while one of the base-reflections actually changes from flat in 50 Hz to concave down in 100 Hz (a – a' in Figure 5.2.6). All the channels seem much more separated from each other in 100 Hz, which makes it easier to tell them apart. However, this also makes the entire seismic image look much more chaotic. This might be why a few of the participants in the survey seemed to get more insecure when interpreting channels in this detailed seismic image, even though three more channels on average were interpreted compared to 50Hz.

The change in vertical resolution is also reflected in thickness of the seismic reflections. These are now so thin that most of the details in the mapped input-outcrop are resolved. The max/-max amplitudes now seem restricted to where the isolated CHs (unconnected to IHSs) deposits appear. The apparent thickness in this frequency reflects the actual thickness in the mapped outcrop, where the tuning thickness now is down to 9.2 m.

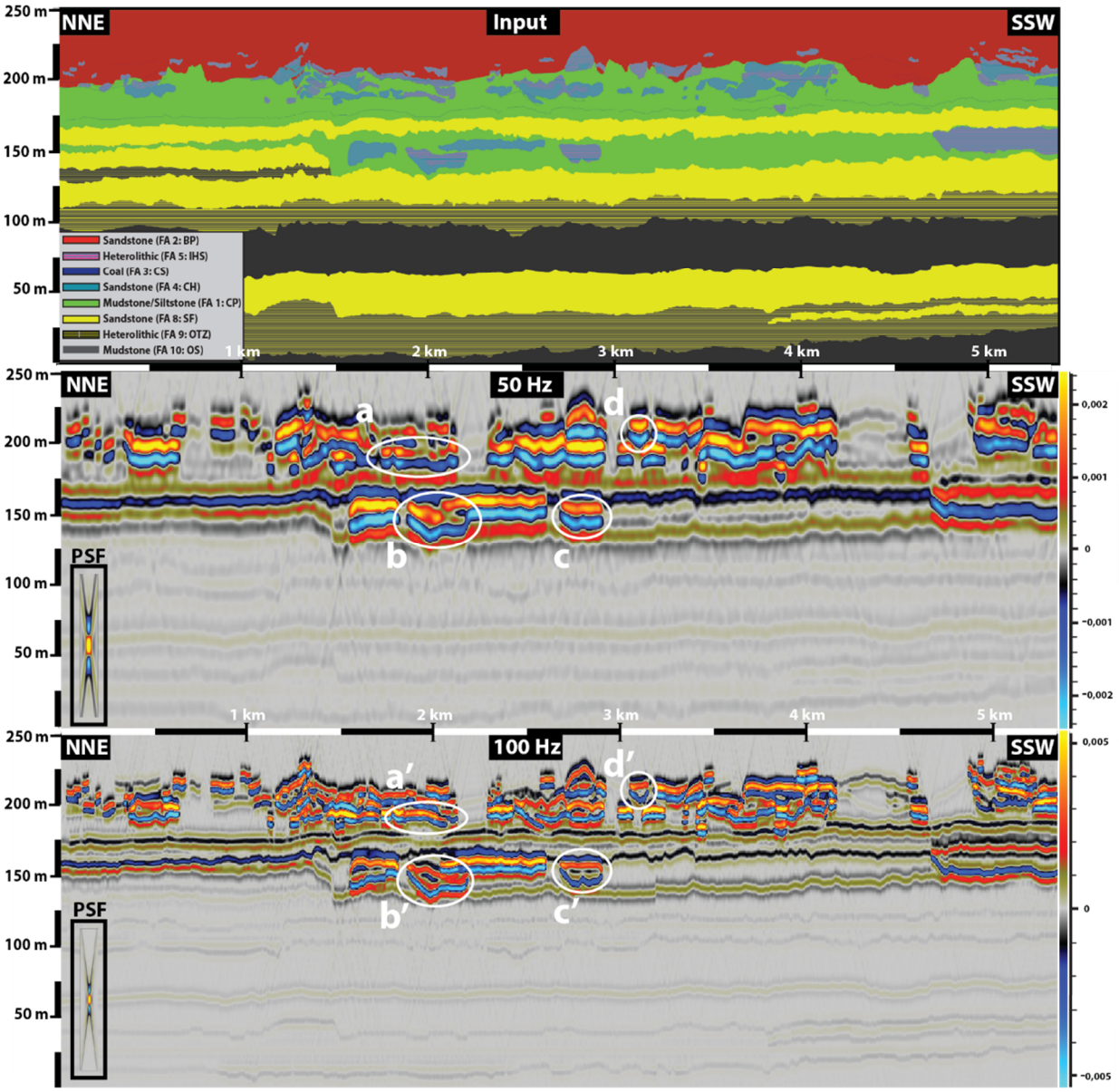

Figure 5.2.6 Comparison between synthetic seismic generated with 50 Hz and 100 Hz, focusing on different features in 100 Hz. These features are highlighted with letters in 50 Hz and corresponding marked letters in 100 Hz. (For uninterpreted version of 100 Hz synthetic seismic, see Appendix Figure A.5)

5.3 Synthetic seismic from input models with reduced detail-level

The synthetic seismograms shown until now has been based on an input model which is faithful to an outcrop interpretation of the non-marine part of the Blackhawk Fm. at a resolution of 14 cm. This detail-level is especially important when interpreting the inclined heterolithic stratification (IHS), as these variable deposits occupy a considerable amount of the coastal plain intervals. However, the impact of such small-scale variation on seismic data is something that often is overlooked when modelling such targets, as the individual beddings are far below the seismic resolution and therefore are too thin to resolve. However, the overall effect of such fine details over the majority of the model, is something that will be tested in this section.

5.3.1 Reflectivity

As the individual sandstone and siltstone layers in the IHS deposits are relatively thin compared to other mapped facies associations, they are not visible in an overview of the full outcrop model used as input. Nevertheless, when zooming into a section, these small layers become visible (Figure 5.3.1a). The generated reflectivity model from the detailed input recognises the individual surfaces of the layers as reflectors (Figure 5.3.1a). This is because the generated reflectors are based on differences in acoustic impedance, where the thickness of the layers does not matter as long as they appear in the velocity- and density input-models with different values. The individual IHS layers represent large changes in reflection coefficients, meaning that the variations between the properties of silt- and sandstone layers are significant. This favours generation of strong seismic reflections from these layers, as the modelling generates synthetic seismic on the base of convoluting the reflectivity with the PSF (Figure 3.3.2).

To visualise the difference in reflectivity when IHS deposits are not present, a new model without these details was created. The individual sandstone and siltstone layers were removed and replaced with a generalized body of average density and velocity between the two lithologies. The new generated reflectivity model in Figure 5.3.1b illustrates how large amount of the selected area that consist of IHS.

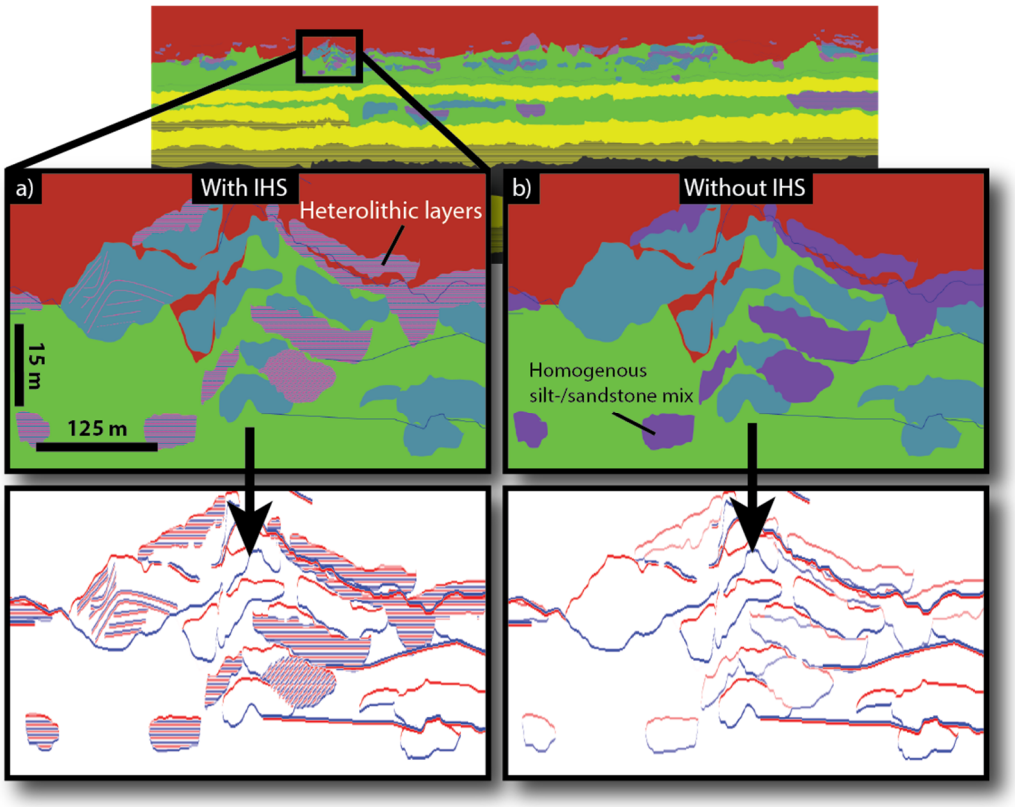

Figure 5.3.1 Differences of the mapped outcrop and corresponding reflectivity in a selected zoomed area between: (a) model with IHS deposits (striped pink and blue lines) and (b) model without layered IHS deposits, but as a homogeneous stratification (purple bodies).

5.3.2 Synthetic Seismic

To see what effect IHS layers have in seismic, the generated seismic of the outcrop with IHS deposits was compared to synthetic seismic without these layers. As the reflectivity model show the individual layers as separate reflectors, one expects these to be separate seismic reflections also. However, as the size of the PSF is the other controlling factor, the ability to resolve of these layers is dependent on whether the PSF is small enough, so the corresponding resolution is high enough to recognise the thin reflectors as separate seismic reflections. To test the effect detailed mapped IHS layers have in seismic, two different resolutions are used; 30 Hz (Figure 5.3.2) and 100 Hz (Figure 5.3.3).

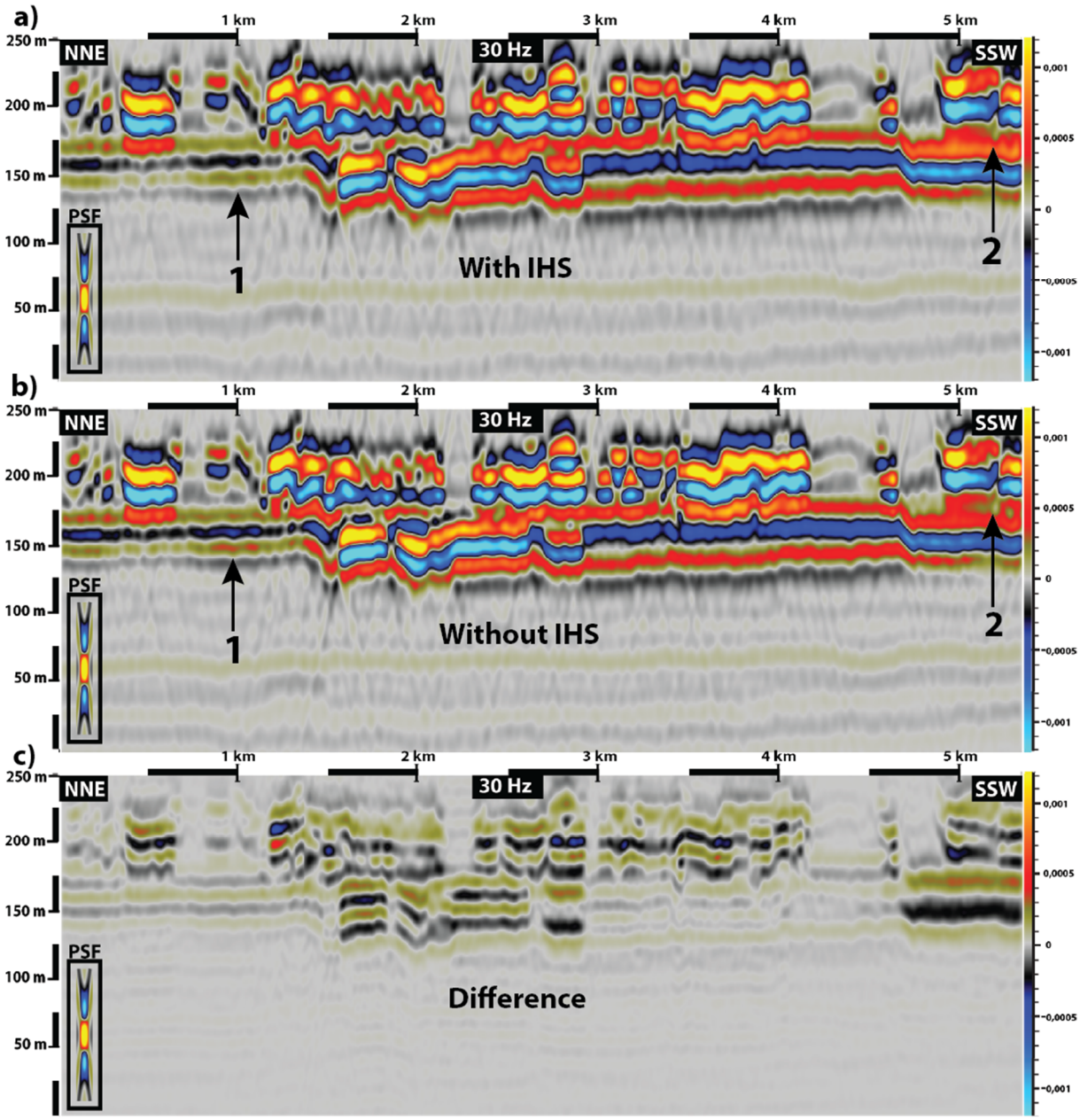

Figure 5.3.2 Three different plots using 30 Hz frequency illustrating the change in seismic due to change in mapped details. The changed details are the individual layers of inclined heterolithic stratification (IHS) which are replaced with a homogenous bed of the average properties from the IHS layers. (a) is the synthetic seismic with IHS layers, (b) is without IHS layers but as a generalized bed and (c) is a difference plot showing the change of seismic data between them. (a.1) shows a weaker amplitude than (b.1), while (a.2) shows a stronger amplitude than (b.2).

When using 30 Hz, the generated seismic image without IHS layers looks almost identical to the previous generated image with these fine-scaled layers of inclined heterolithic stratifications (Figure 5.3.2a, b). There are no observable signs of either fewer or more seismic reflections that would represent the IHS layers when comparing the two. When studying both of the seismic images closely, some minor amplitude differences become apparent in some places (Figure 5.3.2 a.1–b.2 and a.2–b.2). This is further highlighted in a difference plot (Figure 5.3.2c)

where one seismic image is subtracted from the other. This provides an objective way to quantify the differences between the images. However, as visualised in the difference plot in Figure 5.3.2c, the overall differences are relatively vague. Nevertheless, there are some differences, where most of them seem to be related to differences in seismic amplitude. There is no clear indication of geometric change of the seismic related to the change of IHS deposits when comparing the three different images (Figure 5.3.2a, b, c).

If the amplitude in the difference plot are studied closely, the magnitude varies from grey (no difference) to small areas of red (increased amplitude) and blue (decreased amplitude). These max amplitude differences can also be quantified. By comparing the difference-values from the difference plot to the equivalent amplitude values in the seismic, either with or without IHS (the one with the highest value), it is possible to calculate the difference-percentage. For the area in the seismic with max amplitude difference, the amplitude changes with 36 % when comparing seismic with mapped IHS layers to seismic with generalized homogenous beds.

When comparing the difference plot to the two input-models (with and without IHS layers), most of the amplitude differences seem to be related to the change of IHS deposits. However, some amplitudes actually seem to change even though they remain with the same properties in both input-models. E.g., an isolated sandbody and one of the shoreface deposits (Figure 5.3.2a.1-b.1) that do not have any attachment to IHS deposits, increases seismic amplitude in the seismic image where the IHS layers are removed. These deposits are located with a significant distance to the nearest change of IHS deposit.

100 Hz is also tested to see if such high resolution makes a difference in illuminating small-scaled details. As for the 30 Hz, the seismic with and without IHS layers seem very much alike (Figure 5.3.3a, b). Even though many more details are resolved compared to 30 Hz, there are no clear signs of recognising the IHS as thin layers rather than a thick bed. This is visualised by comparing the synthetic seismic with and without IHS, where there are no visible differences in geometry of the seismic reflections. The difference is mainly in amplitudes, which is overall still relatively vague (Figure 5.3.3c). However, the highest amplitude differences are located in other parts of the outcrop than the maximum differences in 30 Hz. Common for both, is that these higher values are related to the change of IHS deposits. The maximum difference-

percentage of amplitude, when using 100 Hz, between the detailed and less detailed synthetic seismic is 31 %. As in 30 Hz, are also deposits that are not directly affected by the change of IHS layers, seem affected by a resulting amplitude change. These changes are minor but could still influence the impression and interpretation of the seismic.

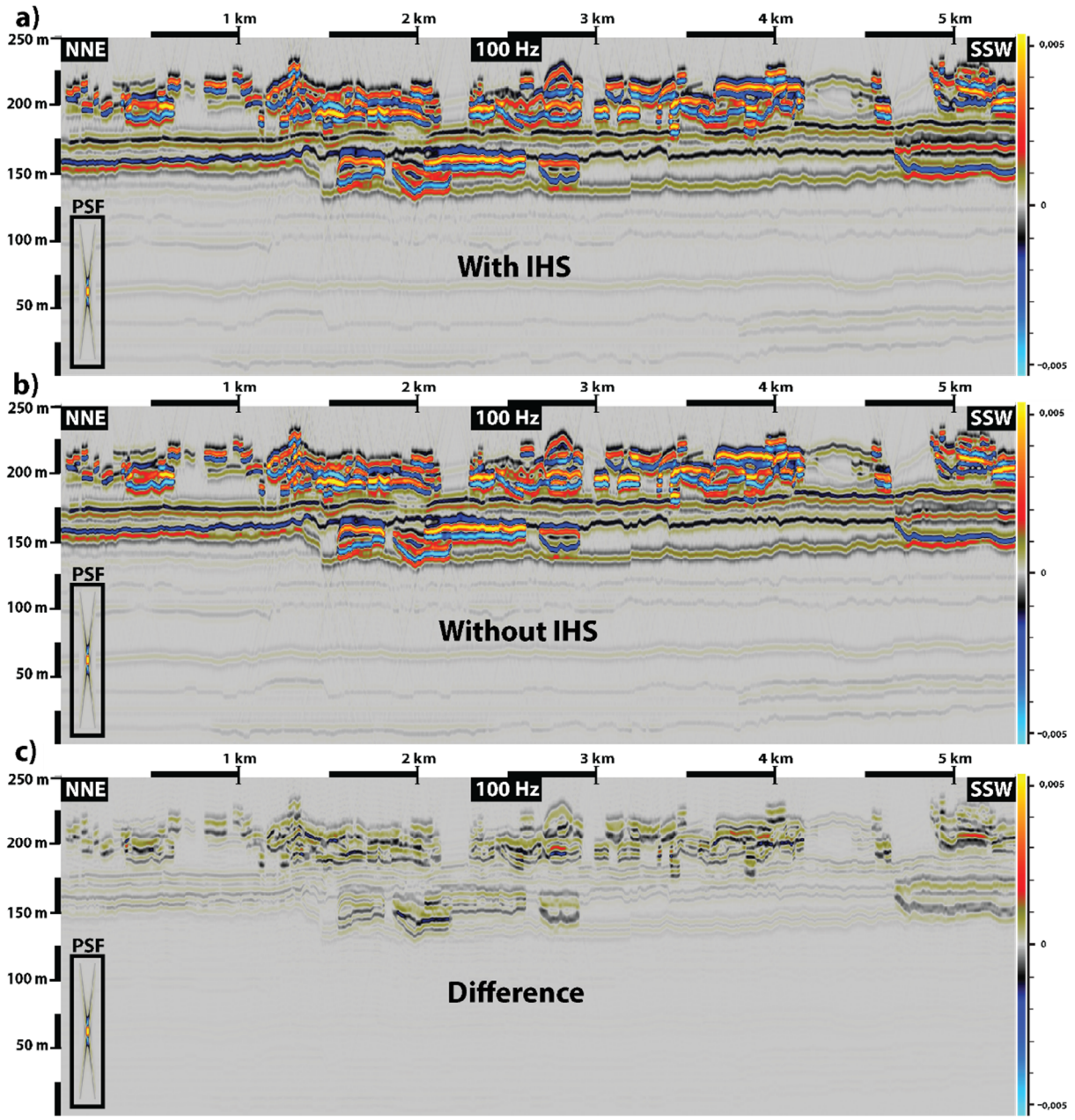

Figure 5.3.3 Three different plots of synthetic seismic using 100 Hz frequency to illustrate the change in seismic due to change in mapped details. (a) is the synthetic seismic with IHS layers, (b) is without IHS layers but as a generalized bed and (c) is a difference plot showing the change in seismic data between them.

5.4 Synthetic seismic using 1D convolution

As using 1D convolution is more common than 2(3)D convolution in the industry, this way of modelling is tested in this section to see what differences the two convolution methods have in an outcrop such as the Beckwith Plateau. To test the response of 1D convolution versus 2(3)D convolution, both normal- and high-resolution seismic are investigated by using 30 Hz and 100 Hz frequency wavelets.

5.4.1 Differences in 1D- and 2D convolution at 30 Hz

When comparing the 1D convoluted seismic in 30 Hz to the equivalent 2(3)D convoluted seismic, one of the main differences is how abrupt the seismic reflections terminates laterally. This makes the impression of the seismic image more dramatic and less smooth compared to the 2(3)D convoluted seismic. This effect decreases the apparent lateral extent to some of the fluvial bodies in the seismic. Furthermore, some of the isolated channel deposits within the coastal plain mudstone could now be interpreted as faulted graben structures instead, as the boundaries are very sharp with different surrounding amplitudes (Figure 5.4.1a). Another effect that might be confusing for interpreters of 1D convoluted synthetic seismic, is how chaotic and discontinuous some of the seismic reflections appear (Figure 5.4.1b). Although the input of the mapped channel deposits might seem chaotic in the first place, some of the deposits appears even more distorted in the 1D convoluted seismic.

There are however some effects of using 1D convolution that makes the synthetic seismic look more realistic compared to 2(3)D convolution using the same dominant frequency. The vertical resolution improves, where some of the reflections that are not visible in 2(3)D convoluted seismic, appears in 1D convoluted seismic. Especially smaller channel deposits, which either do not appear in the seismic or are visualised as smaller geometric bodies than in the input-model, are better illuminated in the 1D convoluted seismic (Figure 5.4.1c).

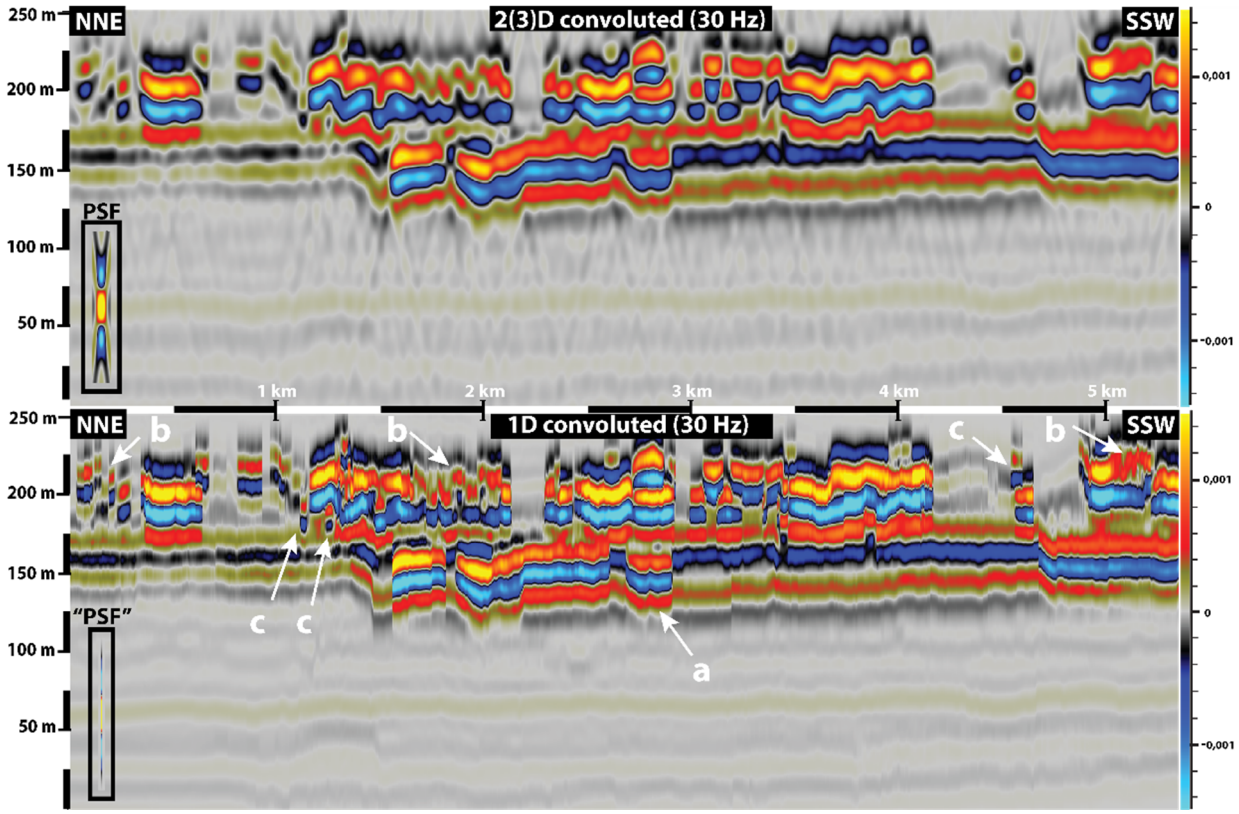

Figure 5.4.1 Two synthetic seismograms that are modelled with different convolution methods. The upper image is modelled using 2(3)D convolution while 1D convolution is used in the lower seismic image. Both are modelled with 30 Hz frequency. Three features in the 1D convoluted seismic that differ the two images are highlighted; (a) sharp terminating seismic lreflections making fluvial deposit look like faulted to graben structures, (b) areas where the seismic becomes more chaotic and (c) small fluvial deposits that are better illuminated.

5.4.2 Differences in 1D- and 2D convolution at 100 Hz

When comparing the two convolution methods in high-resolution seismic using 100 Hz frequency, the differences are minimal. Both the seismic geometries and amplitudes are similar using both convolution methods. This is mainly due to the high resolution of the PSF in 100 Hz, that are able to resolve the reflectivity both laterally and vertically as the equivalent 1D convolution. Figure 5.4.2 illustrates the differences in PSFs for the two convolution methods in 30 Hz and 100 Hz, where the contrast between 2(3)D convolution and 1D convolution is much larger for 30 Hz than for 100 Hz. The lateral resolution of the PSF for 100 Hz in 2(3)D convolution extends to about 10 m. This means that a higher lateral resolution than 10 m does not make much difference when modelling an outcrop like this, as the differences are minimal between 1D- and 2(3)D convolution for 100 Hz. By this reasoning, the convolution method when using such high frequencies does not have a big impact on the

resulting synthetic seismic when modelling an outcrop like the Beckwith Plateau. The differences are larger when using lower resolutions such as 30 Hz.

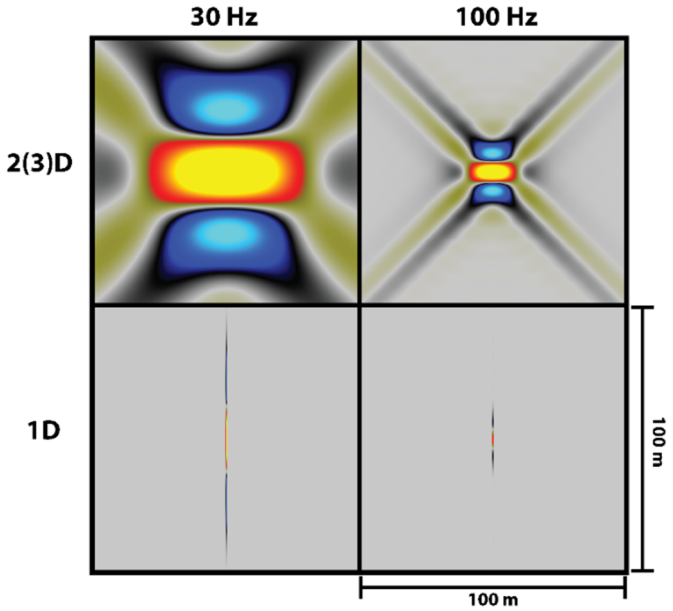

Figure 5.4.2 Four different PSFs for 30 Hz and 100 Hz using 2(3)D- and 1D convolution. The high/width-ratio is 1 and every box is square, where each side is 100 m.

6 DISCUSSION

This study of synthetic seismic modelling of the Beckwith Plateau provides a set of results, which will be evaluated and discussed in this section. First, the interpretation of fluvial channels in the non-marine part of the Blackhawk Fm. will be addressed. Thereafter, the corresponding synthetic seismic using different frequencies will be discussed. Then, the generated synthetic seismic will be compared to real seismic from the Barents Sea. And finally, the way of modelling outcrops such as the Beckwith Plateau will be discussed in terms of convolution method and detail-level.

6.1 Channel interpretation

No previous study has focused on mapping the fluvial channel deposits in non-marine part of Blackhawk Fm. in the Beckwith Plateau before. The mapped and interpreted channel deposits in this study show how the number of channels, size and distribution varies in the lower coastal plain interval compared to the upper. The large and sparse channel deposits within the incised lower coastal plain interval might be further interpreted as a channel complex within an incised valley-fill. This implies that there has been a significant base-level fall leading to incision of both the shoreface and offshore-transition zone deposits of Sunnyside 3. Davies et al. (2006) also acknowledges the incised valley-fill as the "Woodside Canyon IVF", where Howell and Flint (2003a) indicates that these incised valleys in the Blackhawk Fm. proves a base-level drop of 30 m, which fits well with the incision mapped in this outcrop.

The interpreted channel deposits within the valley-fil however, have very different characters. Two of the them are interpreted as completely heterolithic while two others are homogenous sandy channel deposits. This interpretation might have some ambiguity as it is not likely that deposits that are over 200 m wide are completely homogenous/heterogenous and totally changes lithology laterally. Such an interpretation, can in that case be related to significant differences in either the channels (sediment flux and/or sediment source) and/or influence from base-level during deposition, which might be strange as all these channels are deposited within the same level. The width/depth-relationship of the three of channelized bodies in this

interval are below 15, which indicates that these are ribbon deposits from a fixed channel (*sensu* Friend et al., 1979).

A modern example of how this incised valley could have looked like when deposited is from southeast Brazil where the Paraíba do Sul River ends in the Atlantic Ocean (Figure 6.1.1). As in Sunnyside 3, the river here cuts through the shoreface deposits of a wave-dominated shoreline and makes an incision with a fill of coastal plain deposits. As the Paraíba do Sul River closes to the base-level, it visualises how a possible plan-view of the channels within the valley-fill of the Blackhawk Fm. could have looked like. The Paraíba do Sul shoreline and beach ridges has been used as an analogue to the shoreline and beach ridges in both the Kenilworth and Sunnyside members in terms of scale, gross morphology and longshore processes in earlier studies as well (e.g. Hampson & Howell, 2005; Sech et al., 2009; Sømme et al., 2008).

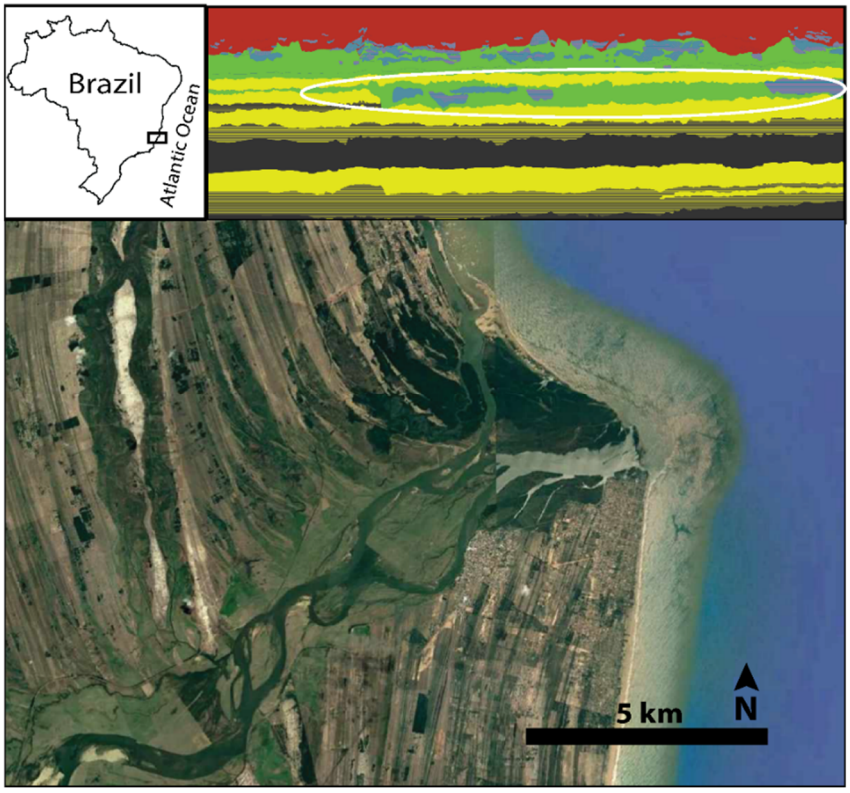

Figure 6.1.1 Satellite photo of where the Paraíba do Sul River flows out in the Atlantic Ocean in southeast Brazil, as a modern analogue to the incised valley-fill in the Beckwith Plateau. The river cuts through all the parallel beach ridges and makes an incised path of coastal plain deposits, just as in Sunnyside 3. Notice the dimensions of the channels. The different appearance at one of the river mouths is due to rainfall from a different imaging date (2017). Satellite photo © Google Earth 2018.

In the upper interval of non-marine deposits in the Blackhawk Fm., the channels have different characteristics compared to the channels in the incised valley-fill below. It has a higher content of channel bodies of varying size that are densely spaced, which represent an environment on a coastal plain that has a higher quantity of river-paths in different dimensions. The high amount of inclined heterolithic stratification, representing point-bars (Table 2), indicates that the deposition is from a meandering channel-complex. Compared to the incised valley environment located close to the coast, this is typically located on a floodplain further away from the base-level. A modern analogue for such environment can be found in the large Zambezi Delta in Mozambique, where the Zambezi River runs out in the Indian Ocean (Figure 6.1.2). The upper coastal plain here visualises how a network of meandering channels could have looked like in the non-marine Blackhawk Fm. during deposition in late Cretaceous.

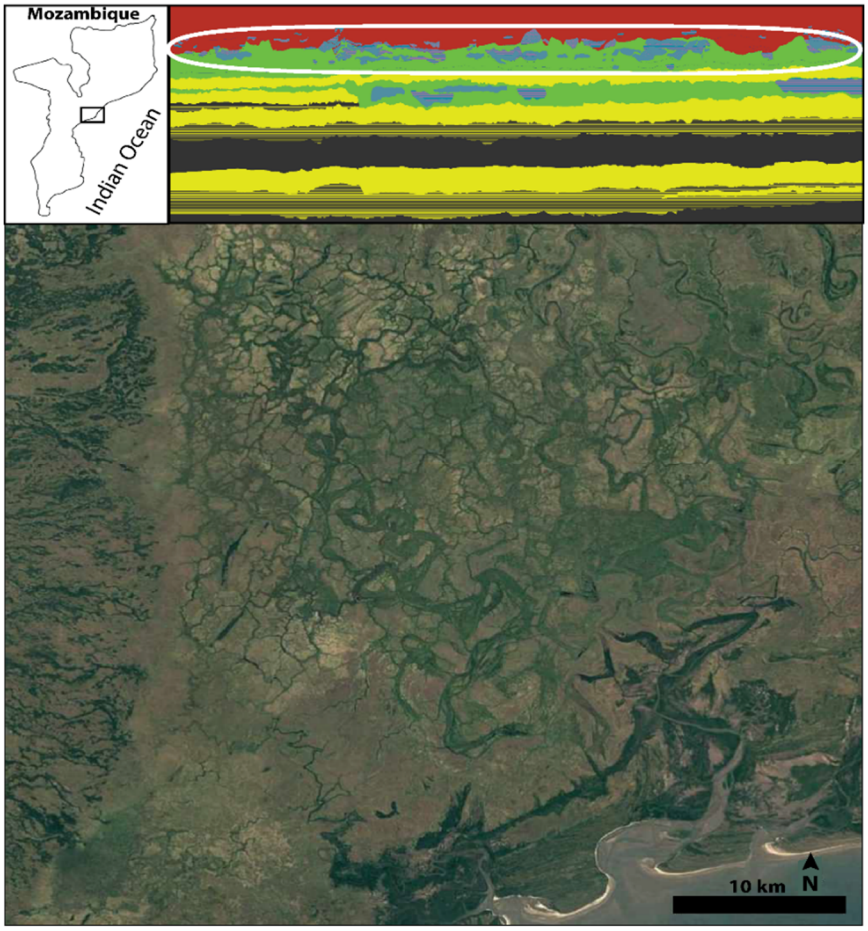

Figure 6.1.2 Satellite photo of the Zambezi Delta in Mozambique, southeast Africa, as a modern analogue to the interpreted channel-system in the non-marine Blackhawk Fm. The photo is showing a complex channel-system in the upper coastal plain, where the channels are varying in both size and shape. Satellite image © Google Earth 2013.

6.2 Seismic interpretation of channels at different dominant frequencies

This is the first study to generate synthetic seismic of an outcrop in the Book Cliffs, whereas Hodgetts and Howell (2000) have earlier generated a more large-scale synthetic seismic of the cross-section to the whole Book Cliffs stratigraphy. There are also no previous studies that have focused on creating synthetic seismic of fluvial deposits in an outcrop by using the same methods as in this study. This makes it difficult to compare the generated seismic to other synthetic seismograms of fluvial deposits. However, several studies have recently used the same methods in seismic modelling of outcrops with different geological targets (Anell et al., 2016; Eide et al., 2017b; Flesland, 2017; Johansen, 2018; Lecomte et al., 2015; Rabbel et al., 2018) where the effects of the synthetic seismic can be compared.

The four generated seismic images (20 Hz, 30 Hz, 50 Hz and 100 Hz) in this study are all able to illuminate the largest interpreted channel deposits in the outcrop. However, the visualisation of these and of the smaller channel deposits are varying between the different frequency wavelets used in this study. The effect these visualisation-differences have for seismic interpreters, is something that will be discussed in this section.

The results of increasing dominant frequency in the synthetic seismic show a corresponding increasing illumination of details. The vertical resolution is the most obvious effect of the detail-differences between the four presented seismic images. The significance of vertical information for an interpreter can be decisive. E.g., for petroleum companies that are drilling wells in the subsurface, either vertical or horizontal, are each un-imaged permeable zones or gas-bearing beds may a potential drilling hazard. In addition, when aiming for smaller reservoir targets like channel deposits, it is crucial to be able to calculate the expected thickness as accurate as possible, both in terms of calculating reservoir volume for potential hydrocarbon content and for well planning.

Many of the seismic effects that are described in section 5.2.2-5.2.5 between the different dominating frequencies in the synthetic seismograms can be explained by the “tuning effect”. This is an effect where the wave-response from closely spaced reflections interferes, either constructively or destructively (Widess, 1973). This interference in zero-phased Ricker

wavelets can either be by the side lobes or the main lobe (Kallweit & Wood, 1982). As shown in Figure 6.2.1 a1-a2, is interference between two lobes creating one large irregular shaped lobe and a resulting thick seismic reflection.

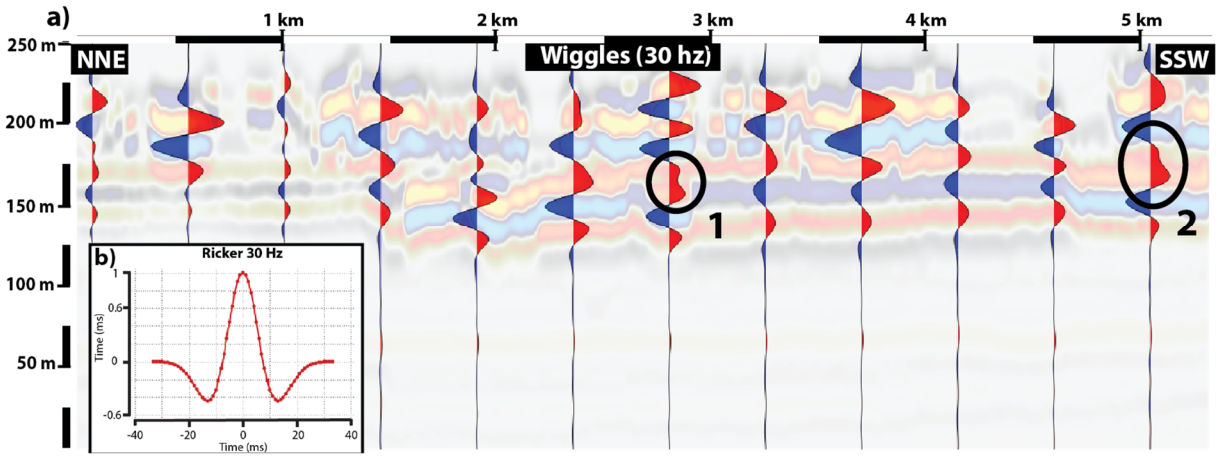

Figure 6.2.1 Illustration of interference in the synthetic seismic of the Beckwith Plateau. (a) Superimposed 30 Hz wiggle-response on synthetic seismic. (1) and (2) show examples of constructive interference and how the shapes differ from the zero-phased Ricker wavelet in (b).

Figure 6.2.2 shows how the vertical resolution and corresponding detail-level can vary for a channel deposit. To quantify the vertical differences in this channel deposit, the apparent thickness is measured (measuring from the centre of max to -max amplitude) and presented in Figure 6.2.3. This figure shows how much the thickness of the deposit changes between 20 Hz, 30 Hz and 50 Hz, but then only have minor changes between 50 Hz, 100 Hz and the input-model. The apparent maximum thickness between 20 Hz and 50 Hz changes from 20 m to 10 m, which is a difference of 50 %. Between 50 Hz and 100 Hz however, the maximum thickness only changes by 1 m. This is most likely due to the tuning thickness, which does not reach the actual thickness of the deposit until 50 Hz. Therefore, it is important for seismic interpreters to be aware of the tuning thickness in the seismic, especially when working with relative thin deposits.

For the lateral resolution, a similar chart is made to quantify how the lateral extension of the channel deposit vary between each frequency wavelet (Figure 6.2.4). This visualises how small the absolute effect is, compared to the vertical thickness, but still shows a similar trend. The apparent width of the channel deposit is 20 % wider in 20 Hz compared to the input-model. The reason why the lateral effects seem so different to vertical for increasing frequency, is

due a higher vertically variation of mapped details compared to laterally. However, the effect of lateral resolution for changing frequency might not be optimal to test in a restricted single channel deposit, as the effect might have a larger impact when several deposits are stacked laterally.

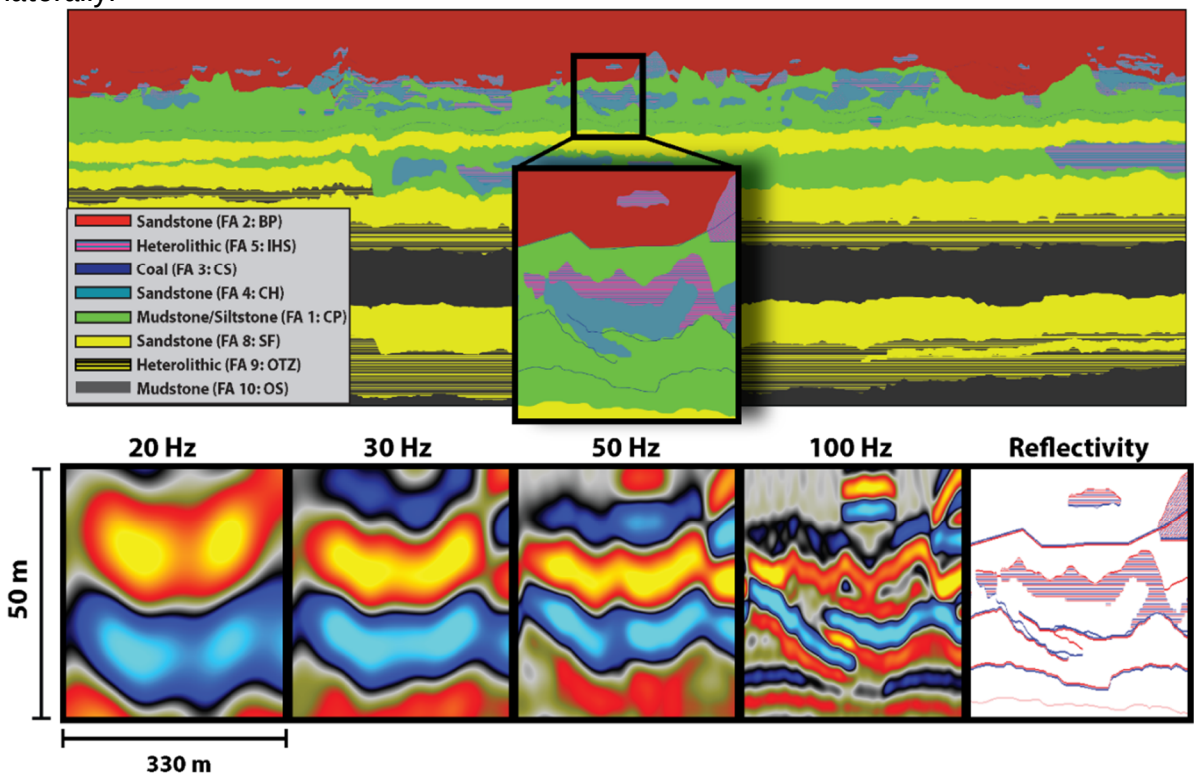

Figure 6.2.2 Variation in synthetic seismic of a selected channel deposit using different frequency wavelets. The selected channel in the zoomed upper image, is one of the large channel deposits in the non-marine Blackhawk Fm. composed by both a sandbody (blue) and surrounding heterolitc deposits (pink and blue reflectors). The selected channel is input to the generated seismic using frequencies of 20 Hz, 30 Hz, 50 Hz and 100 Hz as well as the generated reflectivity. Every box has the same dimensions as the 20 Hz seismic.

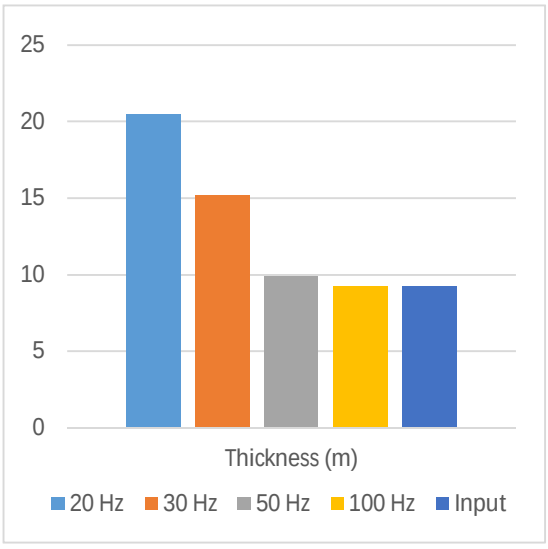

Figure 6.2.3 Chart of measured thickness (max peak to max trough) to the selected channel deposit in synthetic seismic for each frequency and the input-model in Figure 6.2.2.

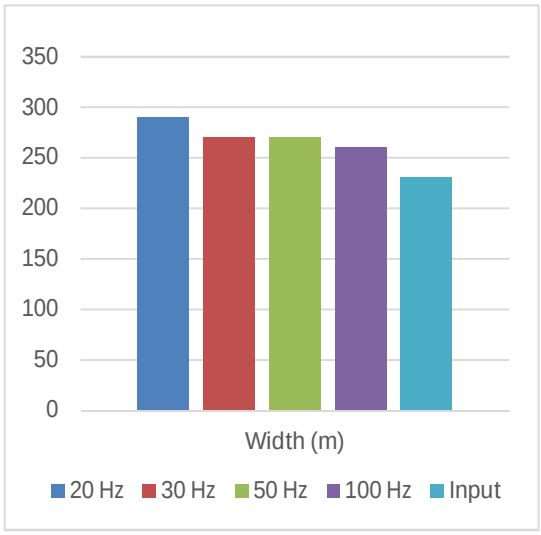

Figure 6.2.4 Chart of measured width to the selected channel deposit for each frequency and the input-model in Figure 6.2.2.

All these three figures (Figure 6.2.2, Figure 6.2.3 and Figure 6.2.4) visualise how an increasing frequency makes the corresponding synthetic seismic appear more and more alike the input-model. In terms of interpretation however, might not the 100 Hz version of the channel deposit in Figure 6.2.2 be so easy to interpret as a channel deposit, as it appears much more chaotic compared to the versions with lower resolution. Some of the participants in the survey support this, as they seemed more uncertain in their interpretations when reaching the final synthetic seismic image of 100 Hz. This is in line with a commonly heard remark about high-resolution seismic data, that it is "difficult to interpret" (Li, 2017). The results of the survey also show that the participants had trouble interpreting the selected channel deposit from Figure 6.2.2 in the more detailed and chaotic 100 Hz seismic. Three participants included the selected channel in three different interpretations, while four participants had the same interpretation of the channel in 30 Hz. This reflects how different fluvial deposits can appear in seismic for different frequencies, where higher resolution does not always make it easier to interpret.

The overall survey results however, show that more channels are interpreted in synthetic seismic with higher frequency. As expected, is it the minor channel deposits that are better illuminated and interpreted more frequently in the 50 Hz and 100 Hz seismograms. All the larger and isolated channel deposits are well illuminated in the seismic for every described dominant frequency, as well as being frequently interpreted by the participants of the survey. As these channel deposits would be the most prominent reservoir targets in an environment like this, it may be asked why one should bother acquiring high-resolution seismic, that often is more expensive, of such targets. The minor channels that are revealed in higher dominant frequencies will most likely not be considered as commercial reservoir targets in the subsurface of offshore shelfs anyway. However, it is important to remember that identifying potential reservoir targets in the seismic is only the first step. Furthermore, these targets need to be analysed in more detail, e.g. thickness, width, connectivity to other channels deposits. As shown in Figure 6.2.2, can channels that seems to appear as a large single-story channel in lower resolution, in fact be composed by several smaller sandbodies and heterolitic bodies. Such knowledge about a hydrocarbon reservoir, can have valuable impact if a deposit is

considered being produced. To do a reservoir analysis as accurate as possible, high-resolution seismic is desirable as it is able to reflect much more of relevant details.

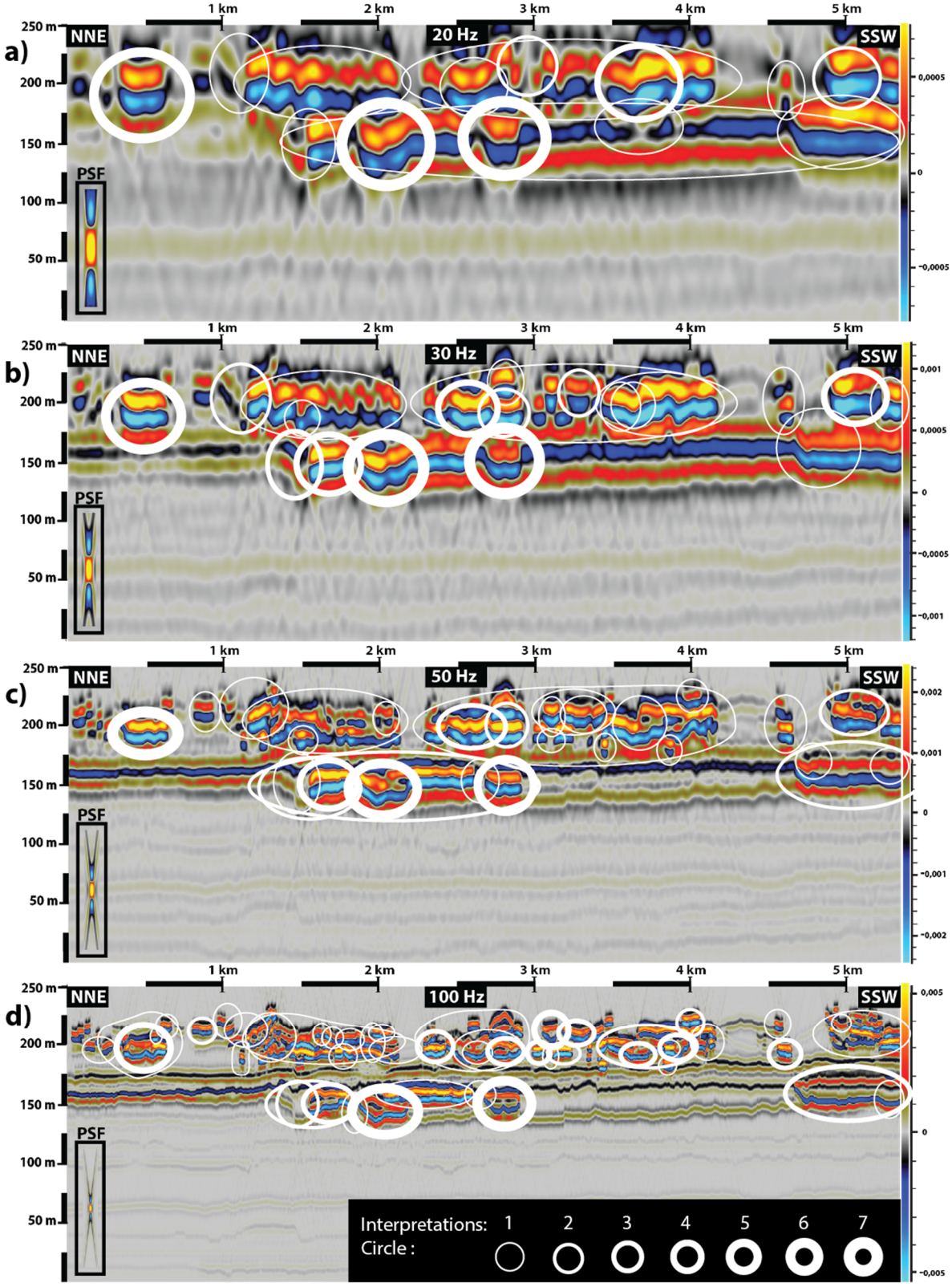

Figure 6.2.5 Results of the survey where participants have ringed out seismic facies that they interpreted as channel deposits. Each seismic image is interpreted individually, starting from low resolution of (a) 20 Hz and increasing to (b) 30 Hz and (c) 50 Hz, before finishing with highest resolution of (d) 100 Hz. The thickness of the stroke represents how many participants that have interpreted the same, ranging from one interpretation at the thinnest to seven at the thickest.

6.3 Comparison between generated seismic and acquired seismic from the Barents Sea

One of the main goals of this study is to use the generated synthetic seismic as an analogue to real seismic data. In order to do so, it is necessary to find out which similarities and differences the modelled seismogram have compared to real seismic. In this study, the results will be compared to real seismic from the Snadd Formation in the Barents Sea due to the previous interpreted depositional environment, even though several other areas with similar depositional environment could have been selected (such as the Ness Formation in the North Sea or the Mungaroo Formation in NW Australia).

For the studied interval in the real seismic datasets, the dominant frequency is approximately 30 Hz, and it will therefore be compared to synthetic seismic of 30 Hz. As channel deposits are challenging to identify only by investigating the seismic in 2D view, a time-slice is created because channels are easier to identify in a plan-view. To visualise the channels even better, a volume attribute that identifies variance in seismic amplitudes are applied to the datasets. Dataset A in the Bjarmeland Platform (Figure 3.4.1) visualises a suitable channel-complex, in both plan-view and 2D seismic-view, for comparison with the generated synthetic seismic.

A selected depth-level shows a network of channel deposits in the variance plan-view that are varying in size and shape, which fits well for comparison with the interpreted environment of the channels in the Beckwith Plateau. One of the largest channel deposits in this interval is analysed at different plan-view depths, where it suddenly expands into a large and bright elliptical shape in the variance map at a shallower depth. This area is in fact drilled, where the shape turned out to be bright elliptical as it is filled with gas (marked as X in Figure 6.3.1). The geometry of this large channel is relatively straight and seem to cut through the smaller surrounding channels, which can be related to the interpreted eroding straight channels in the incised valley in Beckwith Plateau and corresponding modern analogue in the Paraíba do Sul River (Figure 6.1.1). The smaller channels have a more sinuous shape, typical for meandering channels. The network of these channels looks similar to the upper coastal plain of the Zambezi Delta in Mozambique (Figure 6.1.2), the modern analogue to the upper interval of the non-marine Blackhawk Fm.

When looking at the crosscut 2D seismic of these channels, the appearance both has similarities and differences to the generated synthetic seismic. The first noticeable similarity is how the seismic in the Snadd Fm. also appears as heterogenic and chaotic in this interval. The difference is how thick this interval seems compared to in non-marine Blackhawk Fm. interval in the synthetic seismic. Klausen et al. (2014) has measured a formation thickness of 1404 m within this seismic dataset, which only consist of non-marine deposits. In comparison, is measured maximum thickness of the non-marine Blackhawk Fm. in the modelled area only 50 m.

But when focusing on the depth-level of the time-slice in Figure 6.3.1, the illuminated channel deposits in the plan-view also stands out in the cross-cut 2D seismic. These are visible as bodies of higher amplitudes, similar to the channels in the synthetic seismic. However, instead of increasing (red reflections) in acoustic impedance at the top of the channels and decreasing (blue reflections) at the base like in the generated seismic, it is reversed in the real seismic. As the peaks are red and troughs are blue for both seismograms, the reason for the different amplitudes must be due to dissimilar properties. The synthetic seismic uses properties from dataset B to populate the channel deposits and surrounding coastal plain, where the channels in this dataset changes characteristics (Klausen et al., 2014) and might also change properties from dataset A. The geometries of the channel deposits between the real seismic and the synthetic seismic are relatable, where some of the channels show the same convex up shape of the channelized body. But in overall, the seismic channels deposit in 2D from the Snadd Fm. appears more horizontal than in the synthetic seismic. The distribution of the channels in Snadd also seem a bit more sparsely distributed compared to the Blackhawk, where there are more multistory and multilateral channel deposits.

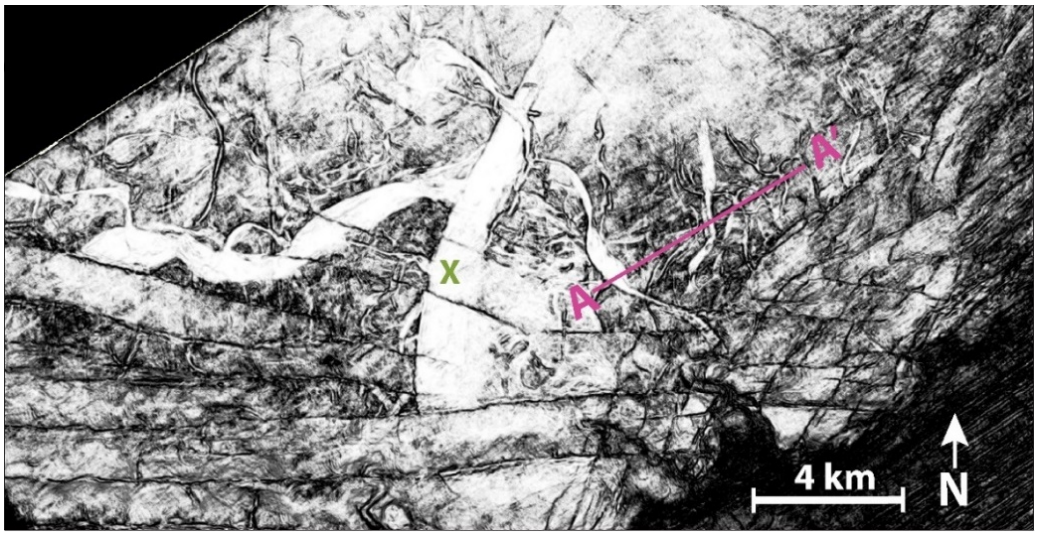

Figure 6.3.1 Variance map showing a plan-view interval of the Snadd Fm.. The variance attribute highlights the channel boundaries and geometries. The channels within the interval A-A' is further studied in 2D seismic in Figure 6.3.2. X marks where well 7222/11-1 has been drilled and discovered gas.

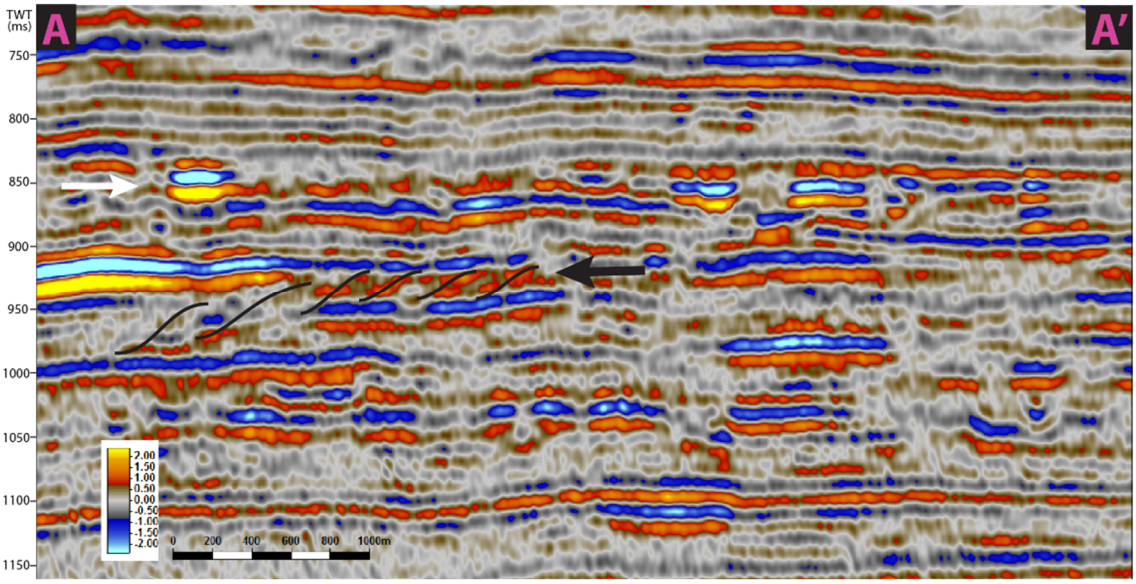

Figure 6.3.2 2D seismic of upper Snadd Fm. in the Barents Sea. The white arrow at 850 ms marks the depth interval of the variance map in Figure 6.3.1. Notice the high amplitude channel bodies in this interval and the interpreted inclined heterolitic stratification in a larger channel in an interval below (indicated by black arrow) (for a version of this figure without interpretations, see Appendix Figure A.1).

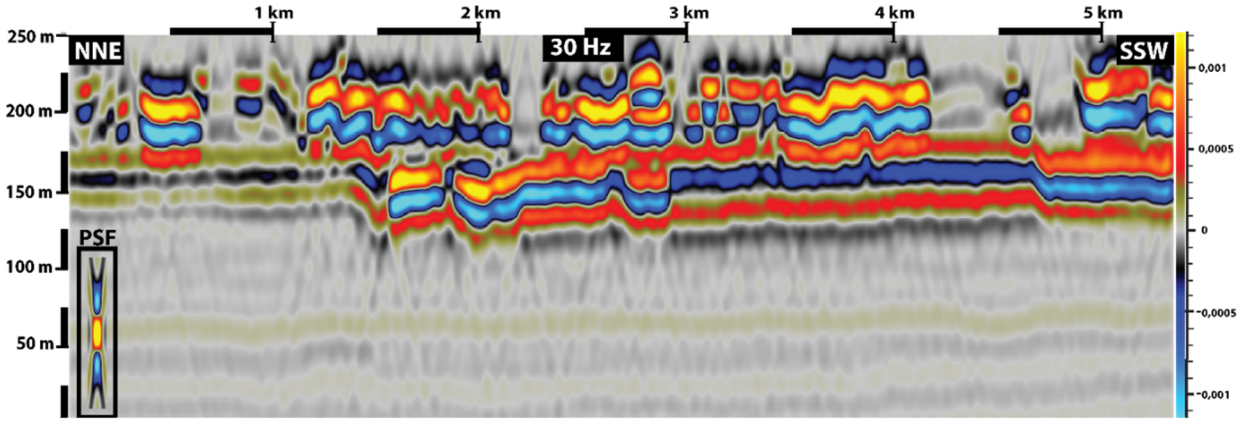

Figure 6.3.3 Synthetic seismic of the Beckwith Plateau at 30 Hz. Notice the similar high amplitude channel bodies as in Snadd Fm..

The size of the channel deposits in the Snadd Fm. appears to be much larger than in the Blackhawk Fm. Klausen et al. (2014) have measured the width and thickness of 714 channels in the Snadd Fm., where 168 of the channels in dataset A have been measured. The mean width of the channels in this dataset for the upper Snadd Fm. is 251 m, while the mean thickness is measured to be 20 m. The size of all the mapped channels in the Beckwith Plateau have not been measured, but an example of a mean-sized channel from the upper Snadd Fm. is created and placed into the input-model at the same scale in Figure 6.3.4 to visualise the difference in dimensions. In addition to being larger, the mean channel illustrates that the width/thickness ratio is also generally lower compared to the wider channel deposits in the Blackhawk Fm. But as this exemplified channel is only based on the mean values, several of the channels in the Snadd Fm. might actually have similar dimensions as the channels in the non-marine Blackhawk Fm.

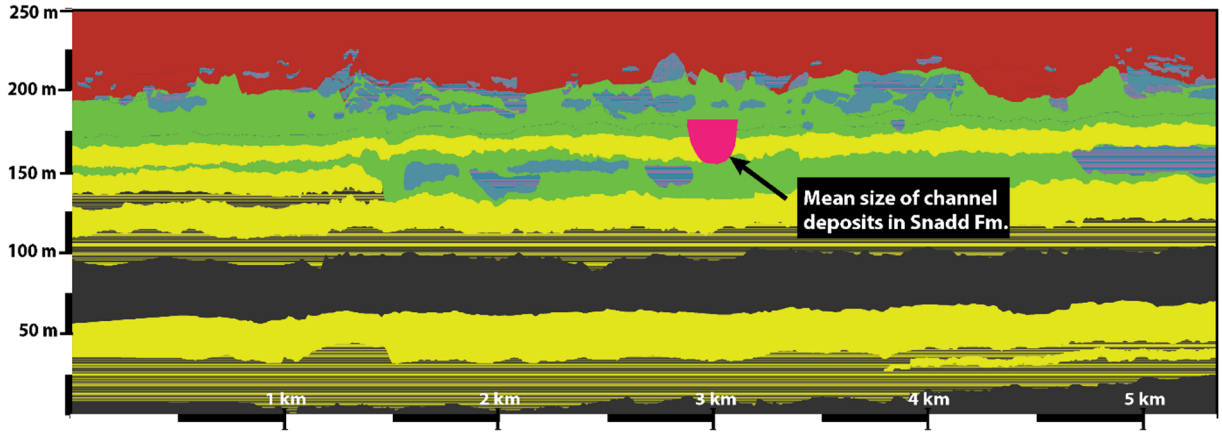

Figure 6.3.4 Illustration of how the size of a mean channel deposit from upper Snadd Fm. from dataset A looks, compared to the channel deposits in the non-marine Blackhawk Fm. Both the mean Snadd channel and the Blackhawk channels are in the same lateral and vertical scale.

One factor that affects the seismic but is not considered much in this study, is the effect of overburden. This is an effect where the elastic properties of the overlaying stratigraphy and architecture influences the seismic signal both towards the target and when returning to receiver (Drottning et al., 2006). To consider overburden however, requires a complex modelling that is outside of the time-range appointed in this study. The overburden that is considered in the model is the 50 m thick amalgamated Castlegate Sandstone. The Snadd Fm. in dataset A has a relative thin overlaying sediment package of 636 m (Norwegian Petroleum Directorate, 2018). Compared to reservoirs in other basins with e.g. thick overlying stratigraphy (e.g. Gulf of Mexico) or stratigraphy with high velocity layers (e.g. salt or

intrusions), is the overburden effect absent for the studied area, which argues for the inconsideration in this study.

6.4 Detail-level and convolution method

Previous input-models in this type of modelling synthetic seismic, has focused on mapping e.g. large igneous intrusions (Eide et al., 2017b; Flesland, 2017; Rabbel et al., 2018), thick pro-deltaic clinoforms (Anell et al., 2016) and whole depositional systems (Hodgetts & Howell, 2000). When mapping such km-scale outcrops, are details below 1 m not considered. To map smaller details might not be necessary for the scope of the study, not be possible due to restricted data and/or could be too time-consuming. As the input-data in this study is high resolution LiDAR-data and the goal is to generate a synthetic seismogram of the outcrop that is as realistic as possible, this study is the first to consider details down to 14 cm within a km-scale outcrop to use as an input in synthetic seismic modelling.

As the results show, these thin inclined heterolitic strata are below seismic resolution and will not be visible as individual seismic reflections for frequencies up to 100 Hz. This shows that the mapped inclined heterolitic stratification in Blackhawk are in a smaller scale than the ones that are visible in Figure 6.3.2 and what has been interpreted in earlier studies of inclined heterolitic stratification in seismic (e.g. Durkin et al., 2017). It is then natural to wonder why mapping these smaller details is needed, as it can be very time-consuming. Even though these mapped details are interpreted and somewhat generalized, is to add them a further step towards making the input-model more realistic. The results do however show that the mapped inclined heterolithic stratification has an impact on the seismic, in terms of amplitude differences. The overall impression of the difference plots (Figure 5.3.2 and Figure 5.3.3) might make the amplitude differences appear as relatively small, so one could still be sceptical to why these details are worth mapping.

In the petroleum industry, amplitudes are used in both exploration and production to e.g. identify bright-spots or to monitor the response to a producing reservoir. When producing oil from reservoirs, water is often injected into the reservoir to push the oil out and improve the

oil recovery (Craig, 1971). The water then replaces the oil in the pores between the sediments, which results in a property change and corresponding amplitude change in the seismic. This means that every percentage of amplitude-change can represent a substantial amount of oil and money in the industry. So even the apparent vague amplitude differences between seismic with and without inclined heterolitic stratification, can have a significant value. Especially when the highest differences show a change of 36 % in amplitude, is it safe to say that modelling and understanding small details can have major repercussions.

In order to make the seismograms as realistic as possible, not only compared to the outcrop, but compared to real seismic as well, the used 2(3)D convolution method need to be discussed against 1D convolution. As visualised in the results, the resulting seismic of the two methods appear very similar, where the largest difference is in lateral resolution. The fine sampling where the PSF and reflectivity is convoluted every 25 cm, is one of the reasons why the resulting seismic of these two convolution methods are so similar. A coarser sampling would lead to larger differences between the two types of synthetic seismic. As shown in Figure 6.4.1, the lateral extent of the selected channel does not vary much between the two convolution methods.

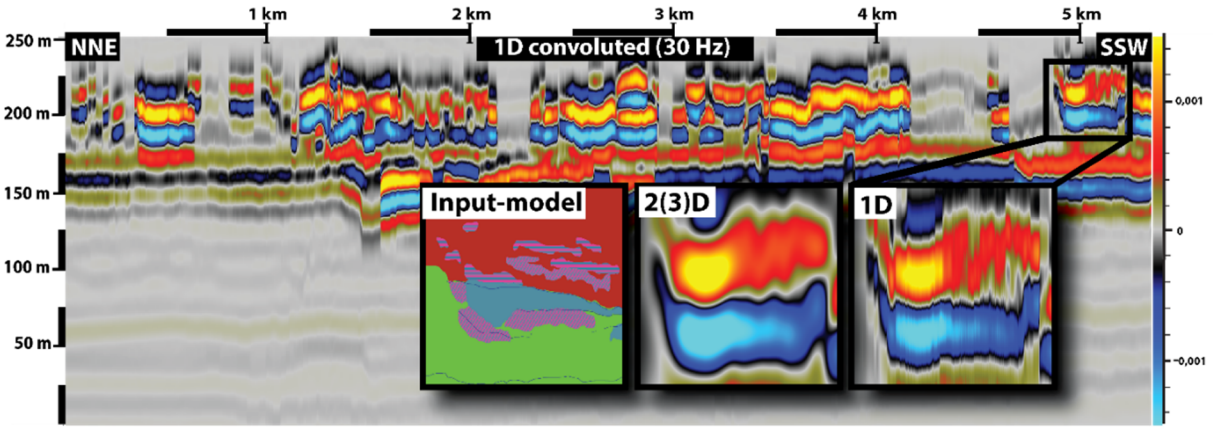

Figure 6.4.1 Comparison of how a selected area of channel deposits differ in seismic between 1D and 2(3)D convolution.

The 1D convolution seem however, to abnormally and abruptly terminate the lateral extent of the channel deposits. The conclusion is that 1D convolution has a higher vertical and lateral resolution than 2(3)D convolution. Other studies that have compared the two methods in modelling of geological outcrops, have discovered much of the same effects as in this study

(Eide et al., 2017b; Grimstad, 2018; Johansen, 2018). The only exception that is not covered in this study, is the illumination effect in steeply dipping surfaces, where 1D convolution can illuminate these while 2(3)D convolution is restricted by the incident angle and corresponding PSF. As the modelled outcrop in the Beckwith Plateau do not have significantly dipping surfaces, this difference was not relevant in this study.

Even though 1D convolution has both a higher vertical and lateral resolution, 2(3)D convolution is still favourable in an analogue study like this. This is because the goal is not to generate synthetic seismograms with the highest possible resolution, but to generate the most realistic seismic image of the outcrop. 1D convolution generates some unrealistic artefacts in the seismic, where areas with lateral variation are illuminated as very fractured seismic reflections. As in Figure 6.4.1 where smaller channel deposits are stacked vertical and lateral to each other, the resulting seismic shows an unnatural high vertical variation along a seismic reflection. Seismic reflections like this cannot be used as an analogue to real seismic data, as real seismic would not respond like this. The corresponding 2(3)D convolution generates a much more recognisable and realistic seismic reflection.

7 CONCLUSIONS AND FURTHER WORK

7.1 Conclusions

This thesis has presented an interpretation of the non-marine Blackhawk Formation in the northern part of the Beckwith Plateau in Utah and used it as an input-model for seismic modelling. The generated synthetic seismograms have increased the understanding of seismic imaging of fluvial deposits. The results and discussion in this thesis have led to the following conclusions:

1. There are two intervals of non-marine deposits in the Blackhawk Fm. in the north Beckwith Plateau, where the lower interval represents an incised valley-fil while the upper interval is from an upper coastal plain environment. The channels characteristics vary from larger and more sparsely distributed channel deposits in the valley-fill, to a large range of sizes and densely spaced deposits in the upper interval.
2. The majority of the mapped fluvial channelized sandbodies are interconnected with inclined heterolitic stratification.
3. Several minor channel deposits are amalgamated into larger multistory and multilateral channel deposits.
4. All the larger channel deposits are resolved in the synthetic seismic data generated with all the frequencies in the study (20, 30, 50 and 100 Hz).
5. A survey was conducted, where geologists with different levels of experience interpreted channels in synthetic seismograms. The survey shows that increasing resolution of the seismic data leads to an increased number of interpreted channels. However, each of the participant interpretations varies, which shows how difficult seismic interpretation of fluvial deposits can be.
6. Comparison between input-models that contain layered inclined heterolitic stratification and a generalized homogenous stratification show a max amplitude-difference of 36 %.

7. Comparison between real seismic from the Snadd Formation and 30 Hz synthetic seismic from the non-marine Blackhawk Formation show similarities in geometry and amplitude, even though the mean size of the channels is much larger in the Snadd Fm.
8. The apparent thickness of one particular channel varies with 50 % between 20 Hz – 50 Hz, due to a tuning thickness variation that is higher than the actual thickness within this interval. This shows how important considering the tuning thickness is in interpretation of seismic data.
9. The seismic resolution attained when using 1D convolution to generate synthetic seismograms, as opposed to using 2(3)D convolution, are in many cases unrealistic. There are also many artefacts in the 1D convolved seismic that would not occur in real seismic data, as lateral variation is not considered in 1D convolution as supposed to real seismic data.

7.2 Further work

The ancient channel-system of the non-marine part of the Blackhawk Formation is very complex, and this thesis is a contribution in understanding this interesting and well-studied formation. However, the following future work ideas could improve and extend the study of fluvial deposits from the Beckwith Plateau as analogue to fluvial reservoirs:

- Measuring the apparent width and depth of the individual channels in the non-marine Blackhawk Fm. and interpreting which channel deposits that are from the same system. These can further be used to make comparison with other channel-systems more quantified.
- Take petrophysical tests of the mapped lithologies in the Beckwith Plateau, so the actual elastic properties can be used as input instead of well data from the Norwegian continental shelf.
- Use the mapped outcrop as input to make statistical 3D reservoir models.
- Use the outcrop data for cross-sectional geometries and satellite images from modern systems to make 3D models of the outcrop and use this to generate synthetic 3D seismic data.
- Compare to other fluvial reservoirs than the Triassic Barents Sea.

REFERENCES

Adams, M. M., & Bhattacharya, J. P. (2005). No change in fluvial style across a sequence boundary, Cretaceous Blackhawk and Castlegate Formations of central Utah, USA. *Journal of Sedimentary Research, 75*(6), 1038-1051.

Allen, J. (1964). Studies in fluviatile sedimentation: six cyclothems from the Lower Old Red Sandstone, Anglowelsh Basin. *Sedimentology, 3*(3), 163-198.

Anell, I., Lecomte, I., Braathen, A., & Buckley, S. J. (2016). Synthetic seismic illumination of small-scale growth faults, paralic deposits and low-angle clinoforms: A case study of the Triassic successions on Edgeoya, NW Barents Shelf. *Marine and Petroleum Geology, 77*, 625-639. doi:10.1016/j.marpetgeo.2016.07.005

Ashton, M. (1993). *Advances in reservoir geology* (Vol. 69). London: Geological Society.

Bellian, J. A., Kerans, C., & Jennette, D. C. (2005). Digital outcrop models: applications of terrestrial scanning lidar technology in stratigraphic modeling. *Journal of Sedimentary Research, 75*(2), 166-176.

Bridge, J. S., & Tye, R. S. (2000). Interpreting the Dimensions of Ancient Fluvial Channel Bars, Channels, and Channel Belts from Wireline-Logs and Cores. *Aapg Bulletin, 84*(8). doi:10.1306/A9673C84-1738-11D7-8645000102C1865D

Buckley, S. J., Howell, J., Enge, H., & Kurz, T. (2008a). Terrestrial laser scanning in geology: data acquisition, processing and accuracy considerations. *Journal of the Geological Society, 165*(3), 625-638.

Buckley, S. J., Vallet, J., Braathen, A., & Wheeler, W. (2008b). Oblique helicopter-based laser scanning for digital terrain modelling and visualisation of geological outcrops. *International Archives of the Photogrammetry, Remote Sensing and Spatial Information Sciences, 37*(Part B4).

Buland, A., Landrø, M., Andersen, M., & Dahl, T. (1996). AVO inversion of Troll Field data. *Geophysics, 61*(6), 1589-1602.

Buller, A. T. (1990). *North Sea oil and gas reservoirs - II : proceedings of the 2nd North Sea Oil and Gas Reservoirs Conference organized and hosted by the Norwegian Institute of Technology (NTH), Trondheim, Norway, May 8-11, 1989*. London: Graham & Trotman.

Burchfiel, B., & Davis, G. A. (1975). Nature and controls of Cordilleran orogenesis, western United States: Extensions of an earlier synthesis. *American Journal of Science, 275*, 363-396.

Cole, R. D., & Friberg, J. F. (1989). Stratigraphy and sedimentation of the Book Cliffs, Utah. *Cretaceous Shelf Sandstones and Shelf Depositional Sequences, Western Interior Basin, Utah, Colorado and New Mexico: Salt Lake City, Utah to Albuquerque, New Mexico June 30–July 7, 1989*, 13-24.

Craig, F. F. (1971). *The reservoir engineering aspects of waterflooding* (Vol. 3): HL Doherty Memorial Fund of AIME New York, NY.

Davies, R., Diessel, C., Howell, J., Flint, S., & Boyd, R. (2005). Vertical and lateral variation in the petrography of the Upper Cretaceous Sunnyside coal of eastern Utah, USA—implications for the recognition of high-resolution accommodation changes in paralic coal seams. *International Journal of Coal Geology, 61*(1), 13-33. doi:https://doi.org/10.1016/j.coal.2004.06.003

Davies, R., Howell, J., Boyd, R., Flint, S., & Diessel, C. (2006). High-resolution sequence-stratigraphic correlation between shallow-marine and terrestrial strata: Examples from the Sunnyside Member of the Cretaceous Blackhawk Formation, Book Cliffs, eastern Utah. *Aapg Bulletin, 90*(7), 1121-1140.

DeCelles, P. G. (2004). Late Jurassic to Eocene evolution of the Cordilleran thrust belt and foreland basin system, western USA. *American Journal of Science, 304*(2), 105-168.

DeCelles, P. G., & Coogan, J. C. (2006). Regional structure and kinematic history of the Sevier fold-and-thrust belt, central Utah. *Geological Society of America Bulletin, 118*(7-8), 841-864.

Drottning, Å., Lecomte, I., Gjøystdal, H., Skorstad, A., Kolbjørnsen, O., & Huseby, O. (2006). Modelling the seismic response to production: A closer look at the sensitivity to overburden, survey, rock physics model and seismic modelling approach: Biennial Geophysical Seminar. *Norwegian Petroleum Society (NPF), Extended Abstracts*, 69-72.

Durkin, P. R., Boyd, R. L., Hubbard, S. M., Shultz, A. W., & Blum, M. D. (2017). Three-Dimensional Reconstruction of Meander-Belt Evolution, Cretaceous Mcmurray Formation, Alberta Foreland Basin, Canada. *Journal of Sedimentary Research, 87*(10), 1075-1099. doi:10.2110/jsr.2017.59

Eide, C. H., Howell, J., & Buckley, S. (2014). Distribution of discontinuous mudstone beds within wave-dominated shallow-marine deposits: Star Point Sandstone and Blackhawk Formation, Eastern Utah. *Aapg Bulletin, 98*(7), 1401-1429.

Eide, C. H., Howell, J. A., & Buckley, S. J. (2015). Sedimentology and reservoir properties of tabular and erosive offshore transition deposits in wave-dominated, shallow-marine strata: Book Cliffs, USA. *Petroleum Geoscience, 21*(1), 55-73. doi:10.1144/petgeo2014-015

Eide, C. H., Klausen, T. G., Katkov, D., Suslova, A. A., & Helland-Hansen, W. (2017a). Linking an Early Triassic delta to antecedent topography: Source-to-sink study of the southwestern Barents Sea margin. *Bulletin, 130*(1-2), 263-283.

Eide, C. H., Schofield, N., Lecomte, I., Buckley, S. J., & Howell, J. A. (2017b). Seismic interpretation of sill complexes in sedimentary basins: implications for the sub-sill imaging problem. *Journal of the Geological Society*, jgs2017-2096-2096v2011. doi:10.1144/jgs2017-096

Elliott, T. (1986). Chapter 6. Deltas. *Sedimentary Environments and Facies, 2nd Edition: Oxford, UK, Blackwell*, 155-188.

Enge, H. v. D., Buckley, S. J., Rotevatn, A., & Howell, J. A. (2007). From outcrop to reservoir simulation model: Workflow and procedures. *Geosphere, 3*(6), 469-490.

Falivene, O., Arbues, P., Ledo, J., Benjumea, B., Munoz, J. A., Fernandez, O., & Martinez, S. (2010). Synthetic seismic models from outcrop-derived reservoir-scale three-dimensional facies models: The Eocene Ainsa turbidite system (southern Pyrenees). *Aapg Bulletin, 94*(3), 317-343. doi:10.1306/08030908157

Flesland, M. (2017). *Controls on architecture and seismic imaging of igneous intrusions: Examples from LIDAR outcrop data on Traill Ø (East Greenland) and seismic data from the conjugate Møre Margin.* (Master Master), University of Bergen, Bergen.

Flint, S. S., & Bryant, I. D. (1993). *The Geological modelling of hydrocarbon reservoirs and outcrop analogues* (Vol. 15). Oxford: Blackwell Scientific.

Flood, Y. (2015). Combined facies analysis and quantitative characterisation of fluvial stratigraphic architecture at outcrop and in subsurface well data: ProQuest Dissertations Publishing.

Flores, R. M., Blanchard, L. F., Sanchez, J. D., Marley, W. E., & Muldoon, W. J. (1984). Paleogeographic controls of coal accumulation, Cretaceous Blackhawk Formation and Star Point Sandstone, Wasatch Plateau, Utah. *Geological Society of America Bulletin, 95*(5), 540-550.

Ford, G. L., & Pyles, D. R. (2014). A hierarchical approach for evaluating fluvial systems: Architectural analysis and sequential evolution of the high net-sand content, middle Wasatch Formation, Uinta Basin, Utah. *Aapg Bulletin, 98*(7), 1273-1304. doi:10.1306/12171313052

Friend, P. (1983). Towards the field classification of alluvial architecture or sequence. *Modern and ancient fluvial systems*, 345-354.

Friend, P., Slater, M., & Williams, R. (1979). Vertical and lateral building of river sandstone bodies, Ebro Basin, Spain. *Journal of the Geological Society, 136*(1), 39-46.

Ghinassi, M., Nemec, W., Aldinucci, M., Nehyba, S., Özaksoy, V., & Fidolini, F. (2014). Plan-form evolution of ancient meandering rivers reconstructed from longitudinal outcrop sections. *Sedimentology, 61*(4), 952-977.

Gibling, M. R. (2006). Width and thickness of fluvial channel bodies and valley fills in the geological record: a literature compilation and classification. *Journal of Sedimentary Research, 76*(5), 731-770.

Golyan, M. F. (2012). *Compaction, rock property evolution and rock physics diagnostics of Askeladd discovery, Norwegian Barents Sea.*

Grimstad, T. J. (2018). *Modelling illumination and resolution effects in seismic with a 2(3)D convolution method (in press).* (Master), University of Bergen, Bergen.

Hampson, G. J. (2010). Sediment dispersal and quantitative stratigraphic architecture across an ancient shelf. *Sedimentology, 57*(1), 96-141.

Hampson, G. J., Davies, W., Davies, S. J., Howell, J. A., & Adamson, K. R. (2005). Use of spectral gamma-ray data to refine subsurface fluvial stratigraphy: Late Cretaceous strata in the Book Cliffs, Utah, USA. *Journal of the Geological Society, 162*(4), 603-621.

Hampson, G. J., & Howell, J. A. (2005). Sedimentologic and geomorphic characterization of ancient wave-dominated deltaic shorelines: Upper Cretaceous Blackhawk Formation, Book Cliffs, Utah, USA.

Hampson, G. J., Royhan Gani, M., Sahoo, H., Rittersbacher, A., Irfan, N., Ranson, A., . . . Buckley, S. J. (2012). Controls on large-scale patterns of fluvial sandbody distribution in alluvial to coastal plain strata: Upper Cretaceous Blackhawk Formation, Wasatch Plateau, Central Utah, USA. *Sedimentology, 59*(7), 2226-2258.

Hampson, G. J., & Storms, J. E. (2003). Geomorphological and sequence stratigraphic variability in wave-dominated, shoreface-shelf parasequences. *Sedimentology, 50*(4), 667-701.

Haq, B. U., Hardenbol, J., & Vail, P. R. (1988). Mesozoic and Cenozoic chronostratigraphy and cycles of sea-level change.

Haskell, N. A. (1953). The dispersion of surface waves on multilayered media. *Bulletin of the seismological Society of America, 43*(1), 17-34.

Helland-Hansen, W., Helle, H. B., & Sunde, K. (1994). Seismic modeling of Tertiary sandstone clinothems, Spitsbergen. *Basin Research, 6*(4), 181-191. doi:10.1111/j.1365-2117.1994.tb00084.x

Hodgetts, D., & Howell, J. A. (2000). Synthetic seismic modelling of a large-scale geological cross-section from the Book Cliffs, Utah, USA. *Petroleum Geoscience, 6*(3), 221-229. doi:DOI 10.1144/petgeo.6.3.221

Horton, B. K., Constenius, K. N., & DeCelles, P. G. (2004). Tectonic control on coarse-grained foreland-basin sequences: An example from the Cordilleran foreland basin, Utah. *Geology, 32*(7), 637-640.

Howell, J., & Flint, S. (2003a). Siliciclastics case study: the Book Cliffs. *The sedimentary record of sea-level change. Cambridge University Press, Cambridge*, 135-208.

Howell, J. A., & Flint, S. S. (2003b). *Tectonic setting, stratigraphy and sedimentology of the Book Cliffs*: Cambridge University Press.

Jackson, C. A.-L., Grunhagen, H., Howell, J. A., Larsen, A. L., Andersson, A., Boen, F., & Groth, A. (2010). 3D seismic imaging of lower delta-plain beach ridges: lower Brent Group, northern North Sea. *Journal of the Geological Society, 167*(6), 1225-1236.

Jackson, R. G. (1976). Depositional model of point bars in the lower Wabash River. *Journal of Sedimentary Research, 46*(3), 579-594.

Johansen, M. K. (2018). *A modelling workflow for seismic characterization of paleokarst reservoirs (in press).* (Master), University of Bergen, Bergen.

Kallweit, R., & Wood, L. (1982). The limits of resolution of zero-phase wavelets. *Geophysics, 47*(7), 1035-1046.

Kamola, D. L., & Van Wagoner, J. C. (1995). Stratigraphy and facies architecture of parasequences with examples from the Spring Canyon Member, Blackhawk Formation, Utah.
Kauffman, E., & Caldwell, W. (1993). The Western Interior Basin in space and time. *Evolution of the Western Interior Basin: Geological Association of Canada, Special Paper, 39*, 1-30.
Kearey, P., Brooks, M., & Hill, I. (2002). *An introduction to geophysical exploration* (3rd ed. ed.). Oxford: Blackwell Science.
Klausen, T. G., Ryseth, A. E., Helland-Hansen, W., Gawthorpe, R., & Laursen, I. (2014). Spatial and Temporal Changes In Geometries of Fluvial Channel Bodies From the Triassic Snadd Formation of Offshore Norway. *Journal of Sedimentary Research, 84*(7), 567-585. doi:10.2110/jsr.2014.47
Klausen, T. G., Torland, J. A., Eide, C. H., Alaei, B., Olaussen, S., Chiarella, D., & Plink-Björklund, P. (2018). Clinoform development and topset evolution in a mud-rich delta - the Middle Triassic Kobbe Formation, Norwegian Barents Sea (pp. 1132-1169). [Oxford] :.
Klausen, T. G., Torland, J. A., Eide, C. H., Alaei, B., Olaussen, S., Chiarella, D., . . . Plink-Björklund, P. (2017). Clinoform development and topset evolution in a mud-rich delta - the Middle Triassic Kobbe Formation, Norwegian Barents Sea. *Sedimentology*. doi:10.1111/sed.12417
Lebedeva-Ivanova, N., Polteau, S., Bellwald, B., Planke, S., Berndt, C., & Stokke, H. H. (2018). Toward one-meter resolution in 3D seismic. *The Leading Edge, 37*(11), 818-828. doi:10.1190/tle37110818.1
Lecomte, I. (2008). Resolution and illumination analyses in PSDM: A ray-based approach. *The Leading Edge, 27*(5), 650-663.
Lecomte, I., Lavadera, P. L., Anell, I., Buckley, S. J., Schmid, D. W., & Heeremans, M. (2015). Ray-based seismic modeling of geologic models: Understanding and analyzing seismic images efficiently. *Interpretation, 3*(4), SAC71-SAC89.
Lecomte, I., Lavadera, P. L., Botter, C., Anell, I., Buckley, S. J., Eide, C. H., . . . Kjoberg, S. (2016). 2 (3) D convolution modelling of complex geological targets beyond–1D convolution. *First Break, 34*(5), 99-107.
Li, Q. (2017). *High-resolution Seismic Exploration*: Society of Exploration Geophysicists.
Liu, S., Nummedal, D., & Liu, L. (2011). Migration of dynamic subsidence across the Late Cretaceous United States Western Interior Basin in response to Farallon plate subduction. *Geology, 39*(6), 555-558.
Martin, J. H. (1993). A review of braided fluvial hydrocarbon reservoirs: the petroleum engineer's perspective. *Geological Society, London, Special Publications, 75*(1), 333-367. doi:10.1144/GSL.SP.1993.075.01.20
McGowen, J., & Garner, L. (1970). Physiographic features and stratification types of coarse-grained pointbars: modern and ancient examples. *Sedimentology, 14*(1-2), 77-111.
Miall, A. D. (1996). *The geology of fluvial deposits : sedimentary facies, basin analysis, and petroleum geology*. Berlin: Springer.
Miall, A. D. (2006a). *The geology of fluvial deposits : sedimentary facies, basin analysis, and petroleum geology* (4th ed.). Berlin: Springer.
Miall, A. D. (2006b). Reconstructing the architecture and sequence stratigraphy of the preserved fluvial record as a tool for reservoir development: A reality check. *Aapg Bulletin, 90*(7), 989-1002. doi:10.1306/02220605065
Miall, A. D., Catuneanu, O., Vakarelov, B. K., & Post, R. (2008). The Western interior basin. *Sedimentary basins of the world, 5*, 329-362.
Miall, A. D., & Tyler, N. (1991). *The Three-dimensional facies architecture of terrigenous clastic sediments and its implications for hydrocarbon discovery and recovery* (Vol. 3). Tulsa, Okla: SEPM.
Norwegian Petroleum Directorate. (2018). FactPages. Retrieved 18. September 2018 http://factpages.npd.no/factpages/Default.aspx?culture=no

Parker, L. R. (1976). *The paleoecology and flora of the Blackhawk Formation (Upper Cretaceous) from central Utah*.
Pattison, S. A. (1995). Sequence stratigraphic significance of sharp-based lowstand shoreface deposits, Kenilworth Member, Book Cliffs, Utah. *Aapg Bulletin, 79*(3), 444-462.
Planke, S., Berndt, C., Mienert, J., & Bünz, S. (2009). *P-Cable: High-Resolution 3D Seismic Acquisition Technology.* Paper presented at the INVEST 2009 Workshop.
Rabbel, O., Galland, O., Mair, K., Lecomte, I., Senger, K., Spacapan, J. B., & Manceda, R. (2018). From field analogues to realistic seismic modelling: a case study of an oil-producing andesitic sill complex in the Neuquén Basin, Argentina. *Journal of the Geological Society*. doi:10.1144/jgs2017-116
Ricker, N. (1940). The form and nature of seismic waves and the structure of seismograms. *Geophysics, 5*(4), 348-366.
Rise, L., & Sættem, J. (1994). Shallow stratigraphic wireline coring in bedrock offshore Norway. *Scientific Drilling, 4*, 243-257.
Rittersbacher, A., Buckley, S. J., Howell, J. A., Hampson, G. J., & Vallet, J. (2014a). Helicopter-based laser scanning: a method for quantitative analysis of large-scale sedimentary architecture. *Geological Society, London, Special Publications, 387*(1), 185-202. doi:10.1144/SP387.3
Rittersbacher, A., Howell, J. A., & Buckley, S. J. (2014b). Analysis Of Fluvial Architecture In the Blackhawk Formation, Wasatch Plateau, Utah, U.S.A., Using Large 3D Photorealistic Models. *Journal of Sedimentary Research, 84*(2), 72-87. doi:10.2110/jsr.2014.12
Rosenthal, L. (1988). Wave dominated shorelines and incised channel trends: Lower Cretaceous Glauconite Formation, west-central Alberta.
Schwans, P. (1995). Controls on sequence stacking and fluvial to shallow-marine architecture in a foreland basin.
Sech, R. P., Jackson, M. D., & Hampson, G. J. (2009). Three-dimensional modeling of a shoreface-shelf parasequence reservoir analog: Part 1. Surface-based modeling to capture high-resolution facies architecture. *Aapg Bulletin, 93*(9), 1155-1181.
Sheriff, R. E., & Geldart, L. P. (1995). *Exploration seismology* (2nd ed. ed.). Cambridge: Cambridge University Press.
Shi, J.-Q., Imrie, C., Sinayuc, C., Durucan, S., Korre, A., & Eiken, O. (2013). Snøhvit CO2 Storage Project: Assessment of CO2 Injection Performance Through History Matching of the Injection Well Pressure Over a 32-months Period. *Energy Procedia, 37*, 3267-3274. doi:https://doi.org/10.1016/j.egypro.2013.06.214
Simm, R., & Bacon, M. (2014). *Seismic Amplitude: An interpreter's handbook*: Cambridge University Press.
Society of Exploration Geophysicists. (2002). *SEG Y rev 1 Data Exchange format*. Retrieved from
Spieker, E. M., & Reeside Jr., J. B. (1925). Cretaceous and tertiary formations of the Wasatch Plateau, Utah. *Bulletin of the Geological Society of America, 36*(3), 435-454.
Sprinkel, D. A., Weiss, M. P., Fleming, R. W., & Waanders, G. L. (1999). *Redefining the Lower Cretaceous stratigraphy within the central Utah foreland basin*: Utah Geological Survey.
Swift, D. J., Hudelson, P. M., Brenner, R. L., & Thompson, P. (1987). Shelf construction in a foreland basin: storm beds, shelf sandbodies, and shelf-slope depositional sequences in the Upper Cretaceous Mesaverde Group, Book Cliffs, Utah. *Sedimentology, 34*(3), 423-457.
Sømme, T., Howell, J. A., Hampson, G. J., Storms, J. E., Steel, R., Burgess, P., & Dalrymple, R. (2008). Genesis, architecture, and numerical modeling of intra-parasequence discontinuity surfaces in wave-dominated deltaic deposits: Upper Cretaceous Sunnyside Member, Blackhawk Formation, Book Cliffs, Utah, USA (Vol. 90, pp. 421-441): SEPM (Society for Sedimentary Geology).
Thomas, R. G., Smith, D. G., Wood, J. M., Visser, J., Calverley-Range, E. A., & Koster, E. H. (1987). Inclined heterolithic stratification—terminology, description, interpretation and significance. *Sedimentary Geology, 53*(1-2), 123-179.

Vallet, J., & Skaloud, J. (2004). Development and experiences with a fully-digital handheld mapping system operated from a helicopter. *International Archives of the Photogrammetry, Remote Sensing and Spatial Information Sciences, 35*, 1-6.

Van de Graaff, F. R. (1972). Fluvial--deltaic facies of the Castlegate Sandstone (Cretaceous), east-central Utah. *Journal of Sedimentary Research, 42*(3).

Van Wagoner, J. C. (1991). Sequence stratigraphy and facies architecture of the Desert Member of the Blackhawk Formation and the Castlegate Formation in the Book Cliffs of eastern Utah and western Colorado.

Van Wagoner, J. C. (1995). Sequence Stratigraphy and Marine to Nonmarine Facies Architecture of Foreland Basin Strata, Book Cliffs, Utah, U.S.A. In J. C. V. Wagoner & G. T. Bertram (Eds.), *Sequence Stratigraphy of Foreland Basin Deposits: Outcrop and Subsurface Examples from the Cretaceous of North America*: American Association of Petroleum Geologists.

Van Wagoner, J. C., Mitchum, R., Campion, K., & Rahmanian, V. (1990). Siliciclastic sequence stratigraphy in well logs, cores, and outcrops: concepts for high-resolution correlation of time and facies.

Verwer, K., Adams, D., & Kenter, J. (2007). Digital outcrop models: technology and applications. *First Break, 25*(8), 57-63.

Verwer, K., Merino-Tome, O., Kenter, J. A., & Della Porta, G. (2009). Evolution of a high-relief carbonate platform slope using 3D digital outcrop models: Lower Jurassic Djebel Bou Dahar, High Atlas, Morocco. *Journal of Sedimentary Research, 79*(6), 416-439.

Widess, M. (1973). How thin is a thin bed? *Geophysics, 38*(6), 1176-1180.

Wilson, P., Hodgetts, D., Rarity, F., Gawthorpe, R. L., & Sharp, I. R. (2009). Structural geology and 4D evolution of a half-graben: New digital outcrop modelling techniques applied to the Nukhul half-graben, Suez rift, Egypt. *Journal of Structural Geology, 31*(3), 328-345.

Yoshida, S. (2000). Sequence and facies architecture of the upper Blackhawk formation and the lower Castlegate Sandstone (Upper Cretaceous), Book Cliffs, Utah, USA. *Sedimentary Geology, 136*(3-4), 239-276.

Young, R. G. (1955). Sedimentary facies and intertonguing in the upper Cretaceous of the Book Cliffs, Utah-Colorado (pp. 177). Boulder, Colo.

APPENDIX

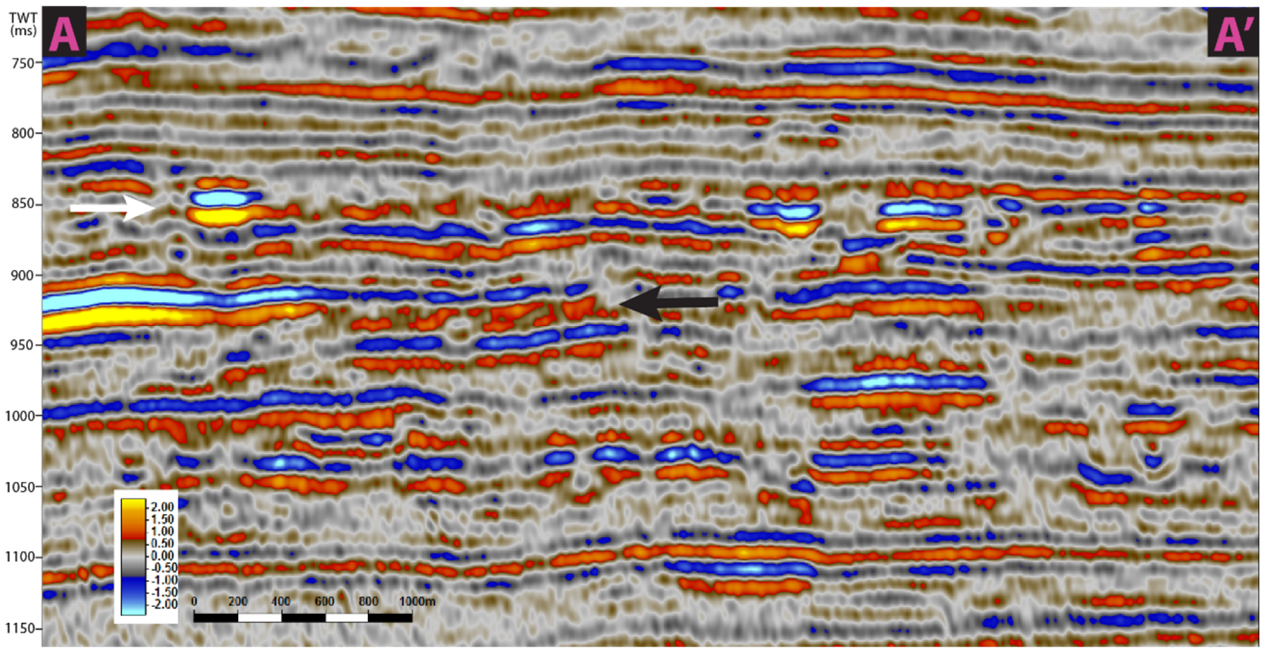

Figure A.1 2D seismic of the channel deposits in the Snadd Fm. without interpretation.

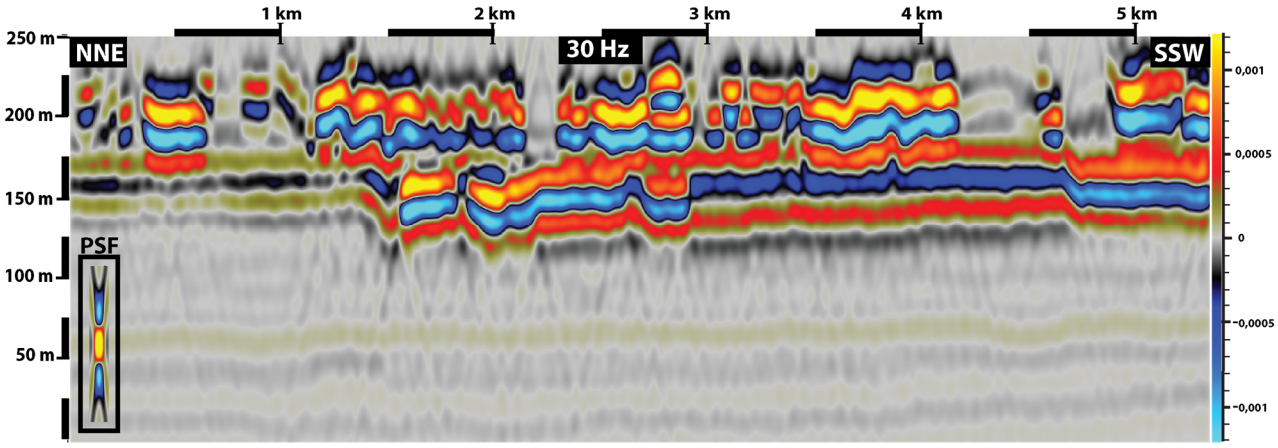

Figure A.2 Uninterpreted verison of the synthetic seimic using 30 Hz frequency.

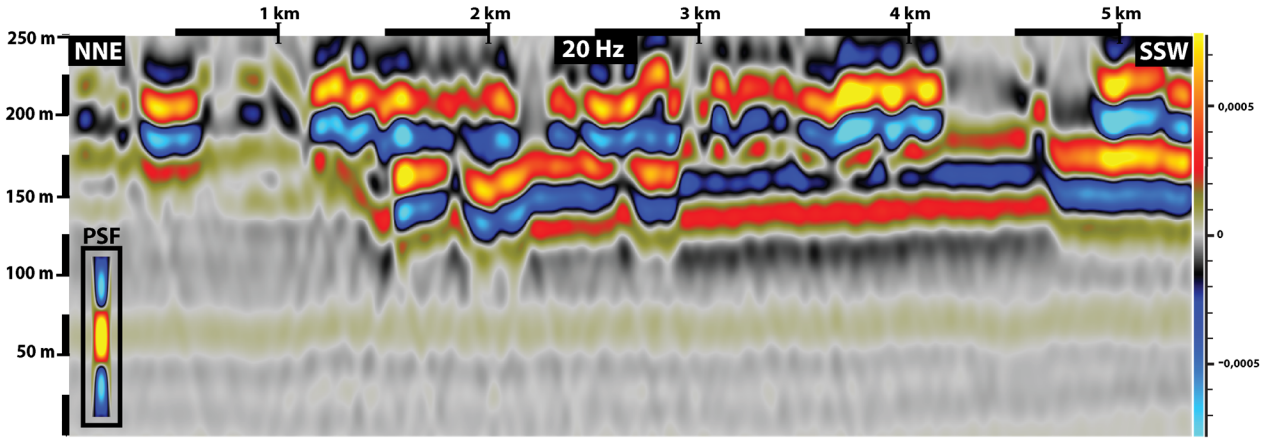

Figure A.3 Uninterpreted verison of the synthetic seimic using 20 Hz frequency.

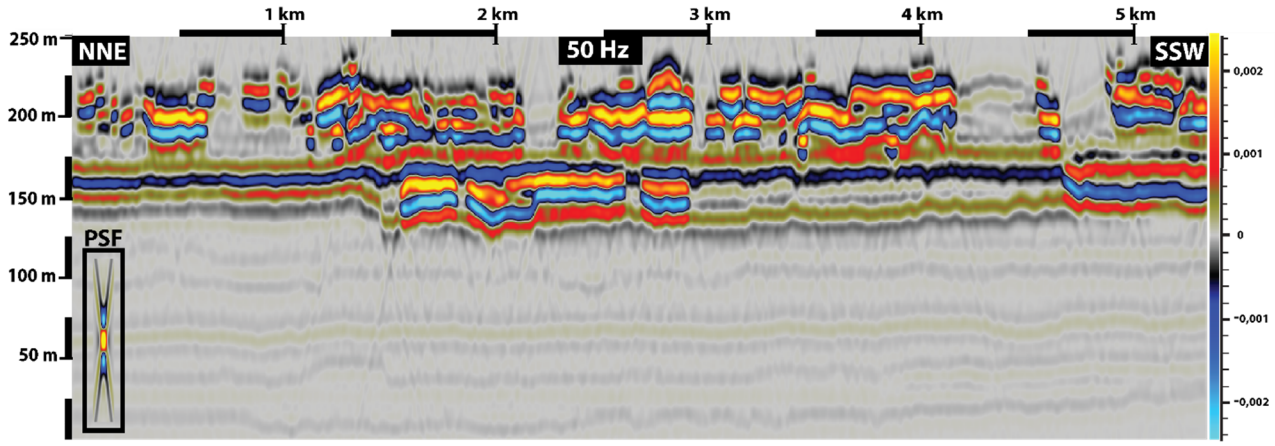

Figure A.4 Uninterpreted verison of the synthetic seimic using 50 Hz frequency.

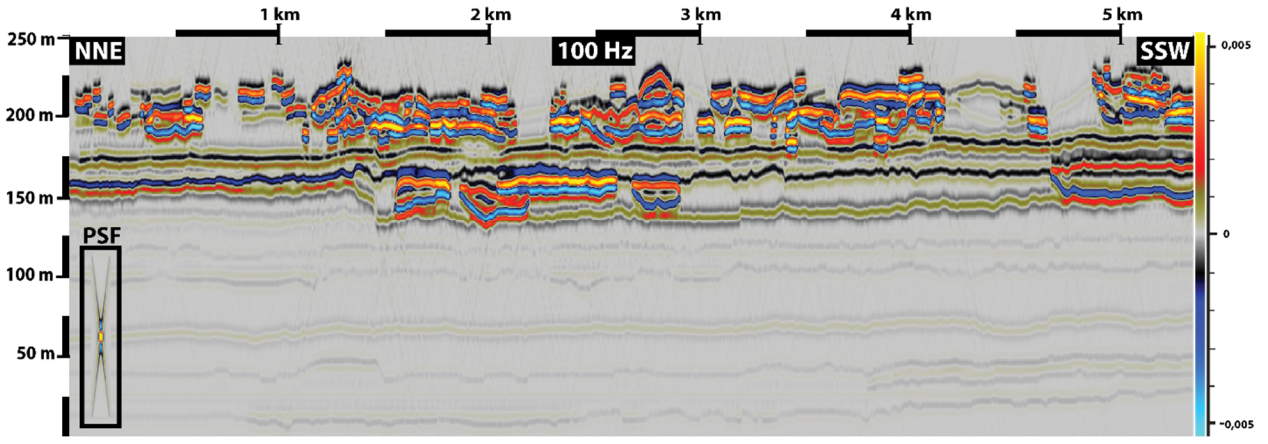

Figure A.5 Uninterpreted verison of the synthetic seimic using 100 Hz frequency.